Mobile phone imaging of fluorescence assays in scattering media

Kamal G. Shah

A dissertation

submitted in partial fulfillment of the

requirements for the degree of

Doctor of Philosophy

University of Washington

2020

Reading Committee:

Paul Yager, Chair

Barry Lutz

Xiaohu Gao

Program Authorized to Offer Degree:

Bioengineering

University of Washington

Abstract

Mobile phone imaging of fluorescence assays in scattering media

Kamal G. Shah

Chair of the Supervisory Committee:

Paul Yager

Department of Bioengineering

Recent efforts to translate diagnostic tests from laboratories to the point of care have yielded countless assays used in clinics and even the home. Point-of-care tests enable earlier diagnosis, potentially improving patient outcomes, reducing superfluous medical procedures, and lowering healthcare costs. Home assays such as lateral flow tests for pregnancy or HIV prioritize low cost and ease of use, typically by labeling antibodies with chromophores in a highly scattering porous substrate. These home assays suffer from poor sensitivities, in part due to the low contrast optics underlying the assay. In contrast, extant laboratory tests are highly sensitive molecular assays that detect fluorescence-labeled biomarkers with costly onboard electronics.

The recent proliferation of low-cost consumer electronics suggests a path toward translating the benefits of laboratory assays to the home, especially by leveraging the advanced camera hardware in modern smartphones to image fluorescence-labeled assays. However, several factors impede the naïve implementation of fluorescence assays in the porous media in which home assays are

performed, particularly light scattering and autofluorescence in porous media and the need for costly optical filters. This dissertation overcomes these challenges with multiple algorithmic, electronic, engineering, and chemistry innovations that together enable mobile phone fluorescence imaging in porous media. This work focuses particularly on sample-agnostic fluorescence imaging of both protein and nucleic acid biomarkers and is a step toward translating fluorescence assays to the home.

Table of Contents

1 Introduction **1**
1.1 Significance 1
1.2 Proposed solution 1
1.3 Specific aims 1
2 Background **4**
2.1 Context 4
2.2 The need for point-of-care diagnostics 4
2.3 Paper microfluidics enable point-of-care diagnostics 5
2.4 Detection strategies for paper microfluidics 8
2.4.1 Electrochemical methods in paper 8
2.4.2 Optical methods in paper 8
2.4.2.i Optical labels 9
2.4.2.ii Optical readers and image processing considerations 11
2.5 Assay optimization strategies to improve limit of detection 13
2.5.1 Increasing signal intensity 13
2.5.2 Reducing background intensity 14
2.6 Gaps in the literature 14
3 Develop a screening strategy to enhance the analytical performance of paper-based fluorescence assays **16**
3.1 Summary 16
3.1.1 Abstract 16
3.1.2 Contributions to the academic literature 16
3.2 Introduction 17
3.3 Methods 18
3.3.1 Survey of autofluorescence in materials commonly used in paper-based assays 18
3.3.2 Application to a quantum dot-labeled lateral flow assay 19
3.4 Results 20
3.4.1 Characterizing autofluorescence lifetimes and wavelengths 20
3.4.2 Hadamard product integral quantifies autofluorescence 23
3.4.3 Improved limit of detection of fluorescence-based lateral flow assay 25
3.5 Discussion 26
3.6 Application of the autofluorescence index to a paper-based nucleic acid amplification assay labeled with a low Stokes' shift fluorophore 29
3.6.1 Motivation 29
3.6.2 Methods 29
3.6.3 Results and discussion 30
3.7 Conclusions 31
4 Mobile phone ratiometric imaging enables highly sensitive fluorescence lateral flow immunoassays without external optical filters **32**
4.1 Summary 32
4.1.1 Abstract 32
4.1.2 Contributions to the academic literature 32
4.2 Introduction 33
4.3 Methods 34
4.3.1 Quantifying spectral sensitivities 34

4.3.2 Design of UV excitation module 34
4.3.3 Validation of ratiometric method to image quantum dots on nitrocellulose 35
4.3.4 Validation with influenza A nucleoprotein assay 36
4.4 Results 37
4.4.1 Screening LEDs and quantum dots 37
4.4.2 Validation of ratiometric method 39
4.4.3 Application of the ratiometric method to a clinically relevant bioassay 40
4.5 Discussion 42
4.6 Conclusions 45
5 Disposable platform for nucleic acid amplification based on a single USB-powered printed circuit board 46
5.1 Summary 46
5.1.1 Abstract 46
5.1.2 Academic contributions 46
5.2 Introduction 46
5.3 Methods 47
5.3.1 Design of the insulated sleeve 48
5.3.2 Design of the cartridge and electronics 49
5.3.3 Thermal validation 52
5.3.4 Nucleic acid amplification chemistry 52
5.3.5 Performing the NAAT 53
5.4 Results 54
5.4.1 Thermal validation 54
5.4.2 Applying small area heaters to lyse bacteria 55
5.4.3 Applying both small and large area heaters to a real-time, fluorescence NAAT 56
5.5 Discussion 58
5.6 Conclusions 59
6 Two-fluorophore, real-time imaging of nucleic acid amplification tests overcomes artifacts in highly scattering porous media 60
6.1 Summary 60
6.1.1 Abstract 60
6.1.2 Academic contributions 60
6.2 Introduction 60
6.3 Methods 62
6.3.1 Operating principle 62
6.3.2 Design of the mobile phone fluorescence reader 63
6.3.3 Estimating limits of detection 63
6.3.4 Characterizing evaporation artifact 65
6.3.5 Applying fluorescence reader to image a NAAT in real-time 65
6.4 Results 66
6.4.1 Hardware validation and limits of detection 66
6.4.2 Characterizing and overcoming evaporation artifact 68
6.4.3 Application to real-time NAATs 69
6.5 Discussion 71
6.6 Conclusions 72
7 Near-digital amplification in paper improves sensitivity and speed in biplexed reactions 73
7.1 Summary 73
7.1.1 Abstract 73

7.1.2 Academic contributions 73
7.2 Introduction 73
7.3 Methods 75
7.3.1 Overview of near-digital NAAT 75
7.3.2 Performing the near-digital NAAT 76
7.3.3 Optically segmenting mobile phone images 76
7.3.4 Validating near-digital NAAT 77
7.3.4.i Assess improvement of signal to noise ratios 77
7.3.4.ii Characterize impact of diffusion 77
7.3.5 Optimizing near-digital NAAT. 78
7.4 Results 79
7.4.1 Validating near-digital NAAT 79
7.4.1.i Assess improvement of signal-to-noise ratios 79
7.4.1.ii Characterize impact of diffusion 80
7.4.2 Optimizing near-digital NAAT 81
7.4.3 Demonstrating shorter time to positive with optical segmentation 82
7.5 Discussion 83
7.6 Conclusions 86
8 Conclusions 87
8.1 Overall conclusions 87
8.2 Future work 88
9 Acknowledgments 89
9.1 Aim 1 89
9.2 Aim 2 89
9.3 Aims 3 and 4 90
9.4 Aim 5 90
10 References 91
11 Appendix 99

Table of Figures

Figure 2.1: Representative commercial diagnostic tests 5

Figure 2.2: Examples of paper-based assays. 6

Figure 3.1: Luminescence characteristics of Millipore HF120 nitrocellulose. 20

Figure 3.2: Excitation-emission matrices visualize absolute fluorescence emission (unitless) in 0.5 nm increments for excitation wavelengths swept in 10 nm increments. 21

Figure 3.3: Summary of excitation-emission matrix (EEM) data processing for Millipore HF120 nitrocellulose. 22

Figure 3.4: Excitation-emission matrices of several non-nitrocellulose paper membranes commonly used in paper microfluidics 23

Figure 3.5: Imaged spots of quantum dots on dried nitrocellulose membranes (Millipore HF120, GE FF80, Millipore HF135, and GE Immunopore FP) at fixed exposure settings illustrates that fluorescence emission spectra alone cannot screen materials. 24

Figure 3.6: Assessment of an influenza A nucleoprotein (NP) assay on nitrocellulose substrates with varying levels of autofluorescence to validate effect of paper autofluorescence on assay performance. 25

Figure 3.7: Limits of detection of quantum dot-labeled influenza A nucleoprotein assay on various nitrocellulose substrates. 26

Figure 3.8: Representative photos of iSDA endpoint fluorescence. 30

Figure 4.1: Design of USB-powered UV LED module. 35

Figure 4.2: Emission spectra of ultraviolet light-emitting diodes with nominal 365 nm peak emission wavelengths**.** 37

Figure 4.3: Imaging quantum dots with varying peak emission wavelengths with mobile phones. 38

Figure 4.4: Screening quantum dots with varying peak emission wavelengths by signal-to-background ratios. 38

Figure 4.5: Gamma-corrected, normalized spectra of interest. 39

Figure 4.6: Demonstration of the ratiometric method. 40

Figure 4.7: Representative images of lateral flow strips on all devices at all tested concentrations of analyte. 41

Figure 4.8: Standard curves of recombinant influenza nucleoprotein spiked into simulated nasal matrix. 42

Figure 5.1: Summary of the multiplexed, disposable NAAT (MD NAAT) and its autonomous predecessor, the MAD NAAT**.** 48

Figure 5.2: Printed circuit board schematic shows the functional elements of the MD NAAT PCB with the electronic components used to implement them 49

Figure 5.3: Top (**a**) and bottom (**b**) views of the USB-powered printed circuit board underlying the MD NAAT 50

Figure 5.4: Diagrams of the two types of heaters on the PCB 52

Figure 5.5: Small area and large area heaters were reproducible between multiple devices and days 54

Figure 5.6: Small-area heaters lyse bacteria on chip 55

Figure 5.7: On-chip lysis and amplification with 2 assays (*ldh1* and *mecA* genes) and 3 samples in the MD NAAT 56

Figure 5.8: Photos and real-time curves of loop-mediated amplification (LAMP) performed in the MD NAAT targeting the *mecA* gene of MRSA show the platform's ability to perform LAMP (~64 °C amplification temperature) 57

Figure 6.1: Overview of the nucleic acid amplification test (NAAT) fluorescence reader 62

Figure 6.2: Design of a mobile phone fluorescence reader that images two colocalized fluorophores, such as in point-of-care NAATs, in real time 63

Figure 6.3: Principle of operation of the dual fluorophore mobile phone reader 65

Figure 6.4: Standard curves of glass fiber pads containing fluorescein or Texas Red imaged by the mobile phone fluorescence reader 67

Figure 6.5: Imaging fluorophores in high surface area, optically scattering substrates such as paper requires overcoming a light scattering artifact driven by evaporation 68

Figure 6.6: Imaging singleplexed amplification reactions in the MD NAAT in real time with the Nexus 5X phone 69

Figure 6.7: Imaging biplexed isothermal strand displacement amplification reactions performed in the MD NAAT platform with a Pixel 2 phone demonstrates the utility of the differential fluorescence imaging strategy 70

Figure 7.1: Motivation for almost-digital amplification in paper. 74

Figure 7.2: Optical segmentation improves signal-to-noise ratios of nucleic acid amplification in porous media. 79

Figure 7.3: Propagation of amplification front follows Fick's laws immediately after liftoff. 80

Figure 7.4: Optimizing assay time to result by varying the lyophilized master mix concentrations of polymerase (pol.), nicking enzyme (NE), primers, nucleotides (dNTPs), and magnesium sulfate ($MgSO_4$) relative to baseline (1×) 81

Figure 7.5: Demonstrating improved signal-to-noise ratios and time to result with near-digital NAATs 82

Figure 7.6: Gel electrophoresis of completed amplification reactions which were run in paper and centrifuged to isolate the liquid in the amplification pads corroborate real-time phone images 83

Table of Tables

Table 2.1: Representative analytical performance of optical labeling strategies 9

Table 3.1: List of porous materials evaluated 18

Table 3.2: Correlation of autofluorescence index with assay limits of detection. 25

Table 3.3: Autofluorescence index and iSDA spot intensities on several paper substrates 31

Table 4.1: Comparison of improvement in limits of detection (LOD) to literature 44

Table 5.1: Printed circuit board heater bill of materials 51

Table 7.1: Nominal block parameters in optically segmented mobile phone images 77

Table 7.2: Representative digital and point-of-care NAATs 85

Table 11.1: List of abbreviations 99

1 Introduction

"Brevity is the soul of wit."

– Polonius in William Shakespeare's *The Tragedy of Hamlet, Prince of Denmark*, Act 2, 2. *c.* 1600.

1.1 Significance

Infectious diseases contribute substantially to global mortality, comprising over 10% of deaths.[1,2] Highly sensitive diagnostic tests often require costly equipment and trained personnel, which relegate them to laboratory use. Assays are now increasingly translated beyond laboratories to point-of-care settings such as clinics and even homes to reduce barriers to clinical diagnosis and treatment. However, there remains a substantial disparity between the capabilities and sensitivities of assays intended for laboratory and point-of-care settings. For example, many laboratory assays are molecular diagnostic tests that combine sensitive optics, electronics, and advanced enzymatic assays to detect 100 molecules or fewer, whereas point-of-care assays such as lateral flow tests have million-fold worse limits of detection, albeit at a low cost per assay.[3] Factors contributing to the sensitivity gap include the challenging optics in lateral flow tests due to light scattering and low-contrast optical reporters. Improving the performance of point-of-care assays requires overcoming these optics-driven barriers to sensitive analyte detection.

1.2 Proposed solution

Assays intended for point of care settings must balance the often competing needs to minimize cost and maximize sensitivity in an easy to use format. Typical lateral flow tests are performed in highly scattering porous media, are labeled with low-contrast chromophore labels, and are read by eye or a disposable photodiode. In contrast, laboratory assays are performed in wells, labeled with high-contrast fluorophore labels, and are read by sensitive optics (including costly optical filters and photodetectors). Recently, mobile phones with highly sensitive cameras have become ubiquitous. Their cameras integrate optical filters and are increasingly optimized for low-light detection. These advances in consumer electronics suggest a path toward translating the benefits of high-contrast fluorescence labeling to point-of-care assays without requiring new detection hardware. This dissertation details the development of tools that enable imaging fluorophore-labeled assays with mobile phones, focusing especially on platform and sample-agnostic applications to detect protein and nucleic acid biomarkers.

1.3 Specific aims

This section summarizes the contributions of the dissertation to the academic literature. The first two aims focus primarily on detecting protein analytes with mobile phone fluorescence imaging. Aim 1 systematically investigates autofluorescence in porous media and describes a strategy to mitigate its effects, while Aim 2 applies these insights to describe a mobile phone-imaged fluorescence lateral flow test that does not use any external optical filters. Both aims detect influenza A nucleoproteins as a model analyte.

The last three aims describe a mobile phone-imaged, fluorescence-labeled, and real-time nucleic acid amplification platform that was validated with 2 assays for methicillin-resistant *Staphylococcus aureus*. Aim 3 describes the thermal engineering of a USB-powered platform for bacterial lysis and nucleic acid amplification. Aim 4 details a two-fluorophore mobile phone fluorescence reader for the

platform described in Aim 3, which overcomes several optical artifacts that arise when imaging in scattering media. Aim 5 explicates a strategy to improve the signal-to-noise ratio of the assay developed in Aims 3 and 4, wherein images are segmented into blocks in a format akin to digital nucleic acid amplification tests. Specific contributions to the academic literature are detailed below:

1. **Develop a screening strategy to enhance the analytical performance of paper-based fluorescence assays (Chapter 3)**
    - Systematically quantify the autofluorescence of porous media used in paper microfluidics at near-UV and visible excitation and emission wavelengths.
    - Design a mathematically robust, empirically validated strategy to screen porous media based on autofluorescence to improve assay analytical performance.
    - Improve the limits of detection of a fluorophore-labeled lateral flow assay with the screening algorithm.

2. **Mobile phone ratiometric imaging enables highly sensitive fluorescence lateral flow immunoassays without external optical filters (Chapter 4)**
    - Design a low-cost fluorescence detector that eliminates the need for optical filters *via* mobile phone ratiometric imaging of quantum dots excited by an ultraviolet light-emitting diode.
    - Implement the fluorescence detection system on multiple mobile phone models to demonstrate generalizability beyond particular camera hardware.
    - Validate the fluorescence reader by detecting a quantum dot-labeled influenza lateral flow assay with limits of detection comparable to a laboratory fluorescence instrument.
    - Improve the limits of detection of an influenza lateral flow assay imaged with the fluorescence detection system relative to conventional gold nanoparticle labeling and imaging with a scanner.

3. **Disposable platform for bacterial lysis and nucleic acid amplification based on a single USB-powered printed circuit board (Chapter 5)**
    - Develop a highly reproducible, low-cost strategy to adhere a disposable cartridge (for bacterial lysis and nucleic acid amplification) to a printed circuit board that only heats the cartridge from below.
    - Validate small area (surface-mounted resistor) and large area (serpentine wire trace) heaters for bacterial lysis and nucleic acid amplification, respectively.
    - Demonstrate utility of single USB-powered printed circuit board platform by lysing *S. aureus* and performing isothermal strand displacement amplification in porous media.

4. **Mobile phone imaging of colocalized fluorophores enables integrated, colocalized positive controls in point of care nucleic acid amplification assays (Chapter 6)**
    - Design a solid-state fluorescence reader that images two colocalized fluorophores by coupling multipass filters to a mobile phone camera and flash.
    - Develop an algorithm that enables the fluorescence reader to image, in real time, biplexed isothermal strand displacement amplification reactions performed in the paper-based platform described in Aim 3.
    - Detect colocalized, amplifying fluorescence positive controls in real time.
    - Validate algorithm and platform by detecting *S. aureus* DNA.

5. **Near-digital nucleic acid amplification in porous media improves signal-to-noise ratios and time to result (Chapter 7)**
    - Apply principles of digital nucleic acid amplification tests to design an algorithm that optically segments mobile phone images of nucleic acid amplification in porous media.
    - Demonstrate that optical segmentation improves signal-to-noise ratios and time to positive in the nucleic acid amplification platform described in Aims 3 and 4.

Subsequent chapters of this document detail each of these aims by summarizing aim-specific background information, materials and methods, results, discussion, and conclusions. The aim-specific sections are preceded by a chapter describing general background information on the need for point-of-care diagnostics, factors relevant to paper-based assays, and detection schemes used in paper diagnostics. The overall conclusions and future research directions are summarized at the end of this dissertation.

2 Background

"*ὁ βίος βραχὺς, ἡ δὲ τέχνη μακρὴ, ὁ δὲ καιρὸς ὀξὺς, ἡ δὲ πεῖρα σφαλερὴ, ἡ δὲ κρίσις χαλεπή*."

"Life is short, and art [techne] long; the crisis fleeting; experimentations perilous, and decision difficult."

– Hippocrates, *Aphorisms*. Section 1. Part 1. Original Greek from E. Littre, *Oeuvres Completes D'Hippocrate*. Translation adapted with modifications from Charles Darwin Adams, *The Genuine Works of Hippocrates*, 1868. Perseus Digital Library. http://data.perseus.org/citations/urn:cts:greekLit:tlg0627.tlg012

2.1 Context

Substantial portions of this section were published as a book chapter in Methods in Enzymology, which was written with Caitlin Anderson and Dr. Paul Yager.[4] These sections are reproduced below from: Methods in Enzymology, Volume 589. Anderson C*, Shah K*, and Yager P. Sensitive protein detection and quantification in paper-based microfluidics for the point of care, pages 383-411, Copyright 2017, with permission from Elsevier (license 4730891334391).

2.2 The need for point-of-care diagnostics

Reducing the morbidity and mortality of infectious diseases were key tenets of the Millennium Development Goals and are critical to attain their successor, the Sustainable Development Goals.[5] Global mortality from infectious diseases decreased by 19% between 2006 and 2016. Despite this decline, infectious diseases contributed to 6.3 million deaths globally in 2016, comprising 11.4% of total deaths.[1] The disease burden is borne disproportionately by low-income countries, where a majority of deaths are still caused by communicable or infectious diseases.[6] Timely diagnosis and treatment of patients who suffer from infectious disease is critical to lower this disease burden

However practical clinical diagnosis and treatment of infectious diseases is impeded by factors such as patient loss to follow-up and a dearth of appropriate diagnostic assays. Many patients are lost to follow-up due to the long turnaround time of laboratory diagnostic tests from sample acquisition to result. For example, up to 38% of tuberculosis patients in sub-Saharan Africa experience pretreatment loss to follow-up.[7] One strategy to mitigate loss to follow-up is to diagnose infectious diseases at the point of care, which requires assays that are rapid, low-cost, sensitive and specific, operable by minimally-trained end users, and suitable for point-of-care ambient environments. The World Health Organization codified these requirements as the ASSURED criteria (accurate, sensitive, specific, user-friendly, rapid and robust, equipment-free, and deliverable) for sexually-transmitted infections in 2004,[8] but few, if any extant diagnostic assays meet these needs.

Many commercial diagnostic assays with high sensitivity (such as those based on nucleic acid amplification) require trained users, complex user steps, refrigeration, and/or costly consumables, thereby limiting their use in low-resource settings. For example, two highly sensitive platforms for nucleic acid detection are the Cepheid GeneXpert (which detects as few as 10 genomic copies of pathogens such as *Chlamydia trachomatis* in 2 hours)[9,10] and the Alere *i* (results in 15 minutes[11]), which are illustrated in **Figure 2.1**. These laboratory-based tests suffer from the aforementioned limitations

* Denotes authors with equal contributions.

at considerable expense: the GeneXpert unsubsidized price is $78000 for the instrument and $72 per cartridge in constant 2013 US dollars (USD).[12] Recent efforts to improve access to sensitive diagnostic tests have focused on lowering the up-front cost of the instrument while enhancing suitability for the point of care. Such work culminated in the Cepheid GeneXpert Omni, which is a solid-state instrument with a smaller footprint and integrated batteries that costs $2700 (in 2013 USD).[1,13] However, these assays, including the GeneXpert Omni platform, still suffer from high per-test costs and require trained operators, which renders them unsuitable for the point of care.

In contrast, assays that are intended for the point of care typically combine ease of use, rapid time to result, and low cost, but at the expense of diagnostic performance (*i.e.* sensitivity, specificity, or accuracy). Many point-of-care tests are based on the lateral flow assay format, which relies on paper microfluidics to detect biomarkers for infectious diseases. Commercial lateral flow tests feature rapid sample-to-result times of <15 minutes,[14] low cost (less than $10 per test),[15] and minimal user steps; however, these tests have limits of detection above 10^8 molecules of infectious disease biomarkers.[16,17] Expounding the technical principles underlying paper microfluidics will elucidate factors that contribute to poor limits of detection and highlight strategies to improve performance, potentially improving infectious disease diagnosis at the point of care.

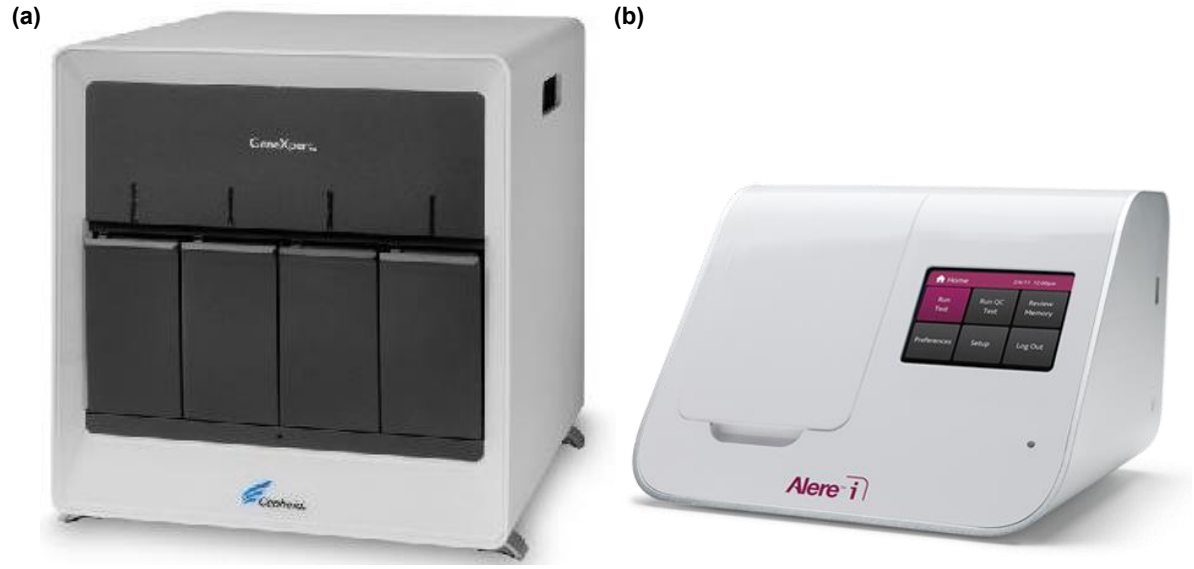

Figure 2.1: Representative commercial diagnostic tests are benchtop laboratory instruments such as the (**a**) Cepheid GeneXpert IV or the (**b**) Alere *i*, both of which are sample-to-result tests that require stable electricity, trained users, and climate-controlled environments. Images were adapted from Cepheid and Alere.

2.3 Paper microfluidics enable point-of-care diagnostics

Paper-based assays use thin sheets of porous media, such as nitrocellulose, cellulose, or glass fiber, to manipulate and process small volumes of fluids. Such assays are especially conducive to point-of-care testing of biological analytes due to their low cost, portability, and ease of use. Lateral flow assays are the simplest paper-based devices, which consist of strips of nitrocellulose that wick fluid based on capillary flow without requiring pumps or additional machinery. A sample pad is usually present at the "input" end, which is often a glass fiber pad onto which a sample is added. The sample then elutes into a conjugate pad, which is typically also a glass fiber material, in which reagents for the assay are stored in dry form and are rehydrated by application of a sample to the

sample pad (**Figure 2.2a**). A wicking or collection pad, often made of cellulose, is typically present at the end of the device opposite from the "input" end to draw fluids through the rest of the device. A typical lateral flow assay has a test line and a control line orthogonal to the flow direction, both of which are zones in which capture agents have been deposited on the membrane. Presence of the target analyte and adequate fluid delivery, along with rehydration of assay chemistry, is indicated by a change in color or luminescence of the test and control lines, respectively. Pregnancy tests, which detect human chorionic gonadotropin, are examples of lateral flow assays commonly used for protein detection at the point of care.

Despite the commercial success of the urine-based pregnancy test, many other assays require more complex manipulation of the biological sample to enable clinically relevant sensitivity in the detection of an analyte. Platforms such as the two-dimensional paper network (2DPN) format or microfluidic paper-based analytical device (μPAD) format enable the design of these more complex assays through selective or sequential delivery of reagents or fluids (**Figure 2.2b** and **Figure 2.2c**).[18–23] Typically, these devices are manufactured by cutting the paper itself via laser cutting, mechanical shearing, or slicing; depositing reagents via patterning, printing, or striping; and implementing fluidic control through valves, wax deposition, or material layering. These fluidic networks are then housed in a plastic or wax encasing to provide mechanical strength and to position components relative to one another. Such 2DPN and μPAD systems are often then coupled with lateral flow assays for quantitative readout of the analyte concentration.

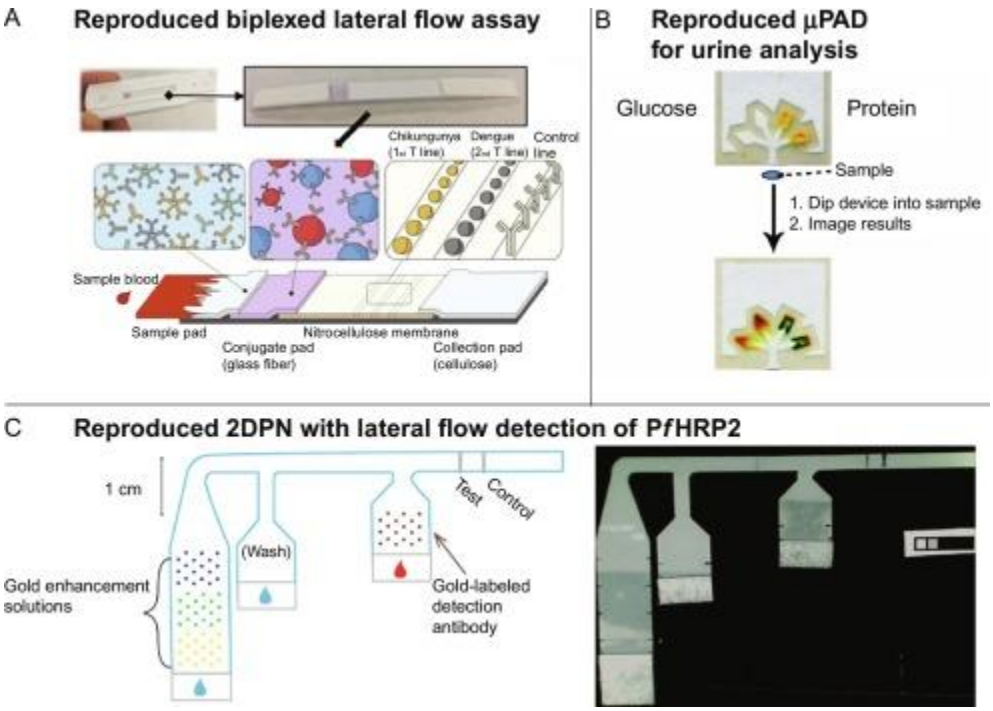

Figure 2.2: Examples of paper-based assays. (**a**) Schematic and photograph of a multiplexed lateral flow assay for differentiating febrile illnesses. (**b**) Photograph and usage of a microfluidic paper analytical device for the detection of glucose and protein in urine. (**c**) Schematics and photograph of a two-dimensional paper network coupled with lateral flow readout of P. falciparum HRP2. Images reproduced from Anderson, Shah, and Yager;[4] and are adapted from Fridley et al., Lee et al., and Martinez et al.[23–25]

Traditional lateral flow assays are initiated by the application of a sample onto the device, wherein the sample passes through a conjugate pad and rehydrates the detection complex. The complex then flows downstream and binds to the capture element deposited at the test line. This type of assay is a sandwich assay, as the typically macromolecular analyte is sandwiched between two binding elements at different epitopes. The detection element in this assay stack can be either directly or indirectly coupled to an optical label for visual readout. Adequate flow and performance of assay reagents, including the detection element and optical labelling chemistry, is confirmed by the development of signal at the control line. As the major components involved in binding of the analyte, the ligands responsible for the capture and detection binding events play a significant role in overall assay sensitivity. Successful performance of these ligands is strongly influenced by their binding thermodynamics and kinetics, including physical and chemical properties ranging from steric effects to isoelectric points.[26]

Key benefits derived from the porous nature of the membranes used in paper-based diagnostics, as compared to traditional microfluidic devices, include potentially improved analytical performance, improved ease-of-use by fewer user steps, reduced cost, and electricity-free usage. This contrasts with traditional microfluidic devices that often require several user steps, electronic pumps, and costly fabrication. Paper-based diagnostics eliminate the need for complex machinery, pumps, and other electrical equipment by manipulating fluids with capillary forces through the pores of the paper membrane.[22] The porous substrate also increases the surface area-to-volume ratio of the capture and control regions, thereby enabling more localized reagent deposition.[27] The assay's limit of detection and analytical sensitivity are thus improved by the increase in the relative concentration of the capture elements, detection ligand, and optical label. Since the surface area-to-volume ratio (typically 50–200 times greater than that of the bulk material)[28] is inversely related to the pore size of the paper substrate, assay performance may be optimized by simply tuning the physical properties of the paper substrate used.[22,27] These advantages may be realized in two-dimensional paper networks or microfluidic paper-based devices to implement controlled fluid manipulation, reagent delivery, and rinse steps to further enhance assay performance and reduce user steps.[22,29,30] Paper-based diagnostics are thus an inherently suitable format for where they are needed the most,[22,27,29–31] such as for point-of-care detection of infectious disease markers such as proteins or nucleic acids.

2.4 Detection strategies for paper microfluidics

Broadly, there are three main factors that influence the performance of paper-based assays:

- Efficiency of analyte extraction from sample and delivery to capture zone.
- Thermodynamics and kinetics with which analyte accumulates in capture zone.
- Signal-to-background ratio of labeling scheme under assay constraints, including the assay reader (if present), substrate, *et cetera*.

While the former two factors are dictated by the analyte of interest (which in turn is based on the sample type and disease/condition targeted), the last factor is typically generalizable to most paper-based assays pending steric, chemical, and electrostatic compatibility with the analyte and capturing strategy. For example, lateral flow assays labeled with optically absorbent, 30-40 nm diameter gold nanoparticles typically have limits of detection on the order of about 1-10 fmol with visual readout for a wide range of analytes spanning proteins and nucleic acids.[3,16,32,33] Improving the analytical performance of such assays requires more sensitive labeling and detection under the constraints in which an assay is performed. Common paper-based assay labeling schemes are broadly categorized as electrochemical or optical; this section considers factors relevant to each.

2.4.1 Electrochemical methods in paper

Electrochemical detection strategies correlate a molecular event with an electrical signal, often by measuring a change in charge distribution, current, impedance, or electric potential in the presence of analyte. Such assays are widely commercialized in the form of glucose meters, many of which electrochemically detect glucose in a fingerprick of blood on a disposable paper strip. Typically, these assays measure oxidation by glucose oxidase or other enzymes to enable high signal-to-noise ratio detection of approximate glucose concentrations.[34] However, electrochemical readout is not especially conducive to detecting analytes present at low levels in complex samples due in part to the poor limits of detection of extant electrochemical assays. For example, glucose is present in human blood at about 4-7 mM,[35] which corresponds to 2 nmol of glucose (about 10^{15} molecules) in a 0.5 μL fingerprick droplet. However, assays for many biological conditions require much lower limits of detection on the order of femtomoles or below (10^{9} molecules or fewer). Representative electrochemical bioassays in paper have limits of detection on the order of 1 pmol (10^{12} molecules) of analyte,[36] which is worse than that of optical detection (which have limits of detection at worst of 700 nmol (10^{11} molecules), but typically on the order of femtomoles or below) as detailed in **Table 2.1**. This thesis therefore explores implementations of optical labels to enhance point-of-care assay performance.

2.4.2 Optical methods in paper

Several optical labeling schemes are commonly used in paper microfluidics, especially in commercial assays for pregnancy or HIV. Potential optical labels may be classified broadly as color-based, chromophoric labels or as luminescent, photon-emitting labels. This section will elucidate the relative merits of potential optical labels, for which representative demonstrations in paper-based assays are documented in **Table 2.1**.

Table 2.1: Representative analytical performance of optical labeling strategies

Detection principle	Potential labels	Potential readout methods	Representative LOD	Dynamic range (log_{10})	References
Optical (absorbance)	Gold nanoparticles (AuNP), colored latex beads	Visual, scanner, smartphone, photodiode	6.9 fmol	4	[16,26]
Optical (chromogenic)	HRP-DAB; HRP-TMB	Visual, scanner, smartphone, photodiode	0.06 fmol; 8.3 fmol	1; 4	[29,37]
Fluorescence	Organic fluorophores (*e.g.*, Texas Red), quantum dots, lanthanide chelates	Visual, smartphone, photodiode	est. 0.7 fmol (10x wrt AuNP)	2	[38]
Phosphore-scence	Lanthanide chelates	Visual, smartphone, photodiode	0.35 fmol	3	[32]
Chemilumine-scence	HRP-Femtoglow	Smartphone, photodiode	0.51 fmol	2	[39]
Thermal	Gold nanoparticles	Infrared (thermal) camera	est. 0.2 fmol (32x wrt AuNP)	3.5	[40]

2.4.2.i Optical labels

2.4.2.i.a Absorbance-based labels

Chromophoric optical labels are commonly utilized in lateral flow assays. Typical chromophores include low-cost, highly stable gold nanoparticles, which selectively absorb light at particular wavelengths,[41] thereby enabling ready discernment against the uniform white background of nitrocellulose membranes typically used in lateral flow assays. As a result, most commercial assays use chromophoric labels, including those for human chorionic gonadotropin and HIV antibodies. However, these labels have the drawback of large particle size (20 nm or larger), which contributes to a potential for aggregation under extreme salt or pH concentrations and to nonspecific binding to the nitrocellulose membrane. Both of these limitations may contribute to reduced signal-to-noise ratio, lower analytical sensitivity, and poorer limits of detection.

Chromogenic optical labels were adapted to lateral flow assays to address some of the limitations of traditional chromophores. As denoted by the term, chromogenic labels operate on the principle of producing a color change to denote the presence of analyte. Such labels were adapted from histological labels, including horseradish peroxidase (HRP)-catalyzed oxidation of diaminobenzidine (DAB) or 3,3'-5,5- tetramethylbenzidine (TMB) into dark precipitates in the presence of the co-substrate hydrogen peroxide. The speed and specificity of this reaction results in a marked reduction in nonspecific signal and improved signal-to-noise ratio compared to gold-based chromophores.[29,42]

Unfortunately, the reagent concentrations must be controlled fairly precisely; hydrogen peroxide must be produced at the time of use due to its instability,[29] additional user steps or complexity are required due to the additional assay steps;[29,37] and the HRP enzyme itself is deactivated by hydrogen peroxide;[43] all of which contribute to a relative dearth of literature utilizing such optical labels. Despite these potential drawbacks, we and others have demonstrated the suitability of chromogenic labels using the HRP enzyme for either wide dynamic range or low limit of detection measurements.[29,37]

2.4.2.i.b Luminescent labels

In contrast to absorbance-based optical labels, luminescent labels have the potential to improve the analytical sensitivity of lateral flow assays without a commensurate increase in assay complexity. Potential options include fluorescent, phosphorescent, or chemiluminescent labels, all of which have been used to improve the signal-to-noise ratio because even when their signals are weak, the very low background at the wavelengths of interest enables the signal to be detected, but at the cost of requiring sensitive light detectors.[20]

Fluorescent labels include organic fluorophores such as Texas Red or fluorescein derivatives, quantum dots, and lanthanide chelates, among others. Each of these absorb photons at particular wavelengths and re-emit them at primarily longer ones as visualized by the labels' excitation and emission spectra, respectively. The difference in the excitation and emission spectral maxima is defined as the Stokes' shift, and larger Stokes' shifts are preferred due to ease of wavelength discrimination, simpler optics, and potentially improved cost and sensitivity.[44–46] Assay developers choose the wavelengths of interest of the excitation source and detectors to minimize cross-talk, typically by using lasers or light-emitting diodes as the excitation source and by using optical filters on both the excitation source and the detector. This wavelength discrimination inherently improves the analytical sensitivities and limits of detection of fluorescence-based lateral flow assays compared to their absorbance-based counterparts. However, most organic fluorophores suffer from small Stokes' shifts and tend to photobleach, while quantum dots suffer from the same size drawbacks as chromophoric nanoparticles, and europium chelates must be excited in the ultraviolet spectrum below 350 nm.[47] Moreover, many nitrocellulose membranes used in lateral flow assays are themselves fluorescent, which may also contribute to reduced signal-to-noise ratios.[48]

Phosphorescent labels may improve the signal-to-noise ratio of lateral flow assays by enabling temporal separation of the excitation and emission of luminescent labels, and also by having larger Stokes shifts than many fluorescent compounds. In this optical detection scheme, fluorophores are deliberately excited into the nonfluorescent, phosphorescent triplet state, which can increase the time constant of photon emission by as much as a dozen orders of magnitude, thereby providing a means to visualize photon-emitting labels against a dark, nonluminescent background after the excitation source is toggled off. However, this improved temporal resolution comes at the expense of reduced signal intensities as a particular phosphorescent molecule undergoes fewer cycles of photon absorption and emission than a fluorophore (due to the longer time constant). For example, a fluorophore with a 5 ns lifetime may theoretically undergo over 1 million photon absorption and emission cycles in one second (in practice, this may be only on the order of 1000 due to excitation into the forbidden triplet state), whereas a phosphor with a 1 second lifetime would undergo less than 1 photon absorption and emission cycle per second. Indeed, use of phosphors as labels in paper-based assays has been limited, in part due the need for a specialized reader, the low quantum yield of phosphors, and the only factor of 10 improvement in limits of detection compared to gold nanoparticle labeling.[32]

Chemiluminescent (and bioluminescent) optical labels are akin to their chromogenic counterparts in that a photon-emitting entity is produced by the catalytic activity of an enzyme, *e.g.* HRP,[49] luciferase,[50] or alkaline phosphatase.[51] The primary benefit of this method is that no illumination source is needed, eliminating the primary source of background noise for fluorescence and phosphorescence detection and thereby greatly enhancing the sensitivity compared to chromophoric labels. Chemiluminescence has been incorporated into highly-sensitive commercial ELISA instruments. However, the drawbacks associated with chromogenic labels using the HRP enzyme are likewise applicable to chemiluminescent labels, along with an added drawback of potentially requiring a specialized reader to image the lateral flow strips in a dark environment.[39]

2.4.2.ii Optical readers and image processing considerations

The choice of optical label guides the selection of an appropriate reader to quantify the assay output. Potential readout methods include visual discernment by human eye, imaging with a scanner, photography *via* a mobile phone or portable camera, or electronic readout with a photodiode. The choice of readout method will constrain assay reproducibility, analytical sensitivity, usability, and feasibility for point-of-care use.

For electronic readout methods, factors such as the spectral sensitivity, quantum efficiency, field of view, and dark noise of the detector will constrain an assay's limit of detection and dynamic range. While devices with broad spectral sensitivity and high quantum efficiency are advantageous, such systems may suffer from poor dark noise, thereby reducing the signal-to-background ratio relative to specialized readers. This tradeoff is an inherent limitation of photodiodes, which comprise many commercial lateral flow strip readers (such as the Qiagen ESEQuant or BD Veritor) and jack-of-all-trades CMOS and CCD detectors (which are found in modern cameras, mobile phones, and scanners). One strategy to improve assay performance is to focus on the wavelengths of interest with optical filters (since the noise is typically distributed over many wavelengths while the fluorophore emits at a more discrete wavelength) or to compensate for noise with multichannel (multicolor) imaging, which are approaches applied in Aims 2 and 4 (Chapters 4 and 6).

2.4.2.ii.a Visual readout

Visual readout by human eye is by far the simplest readout method as it may enable design of an electricity-free assay and enable point-of-care use in austere conditions. Typically, an end user will discern the presence or absence of color (for a qualitative assay) or ascertain the intensity of a color (in a semiquantitative assay) to determine the relative concentration of analyte present. An alternate approach to render paper-based assays semiquantitative is to have spots that selectively change color if the analyte concentration is above a threshold,[52] thereby enabling an end-user to count the number of colored spots to ascertain a specific range of analyte concentration.[53] However, the assay's resolution of analyte concentration is inherently quantized using this approach, and there is a potential that the results of visual readout may not be reproducible between users due to differences in eyesight. While these limitations are relatively inconsequential for qualitative assays including those commercialized for pregnancy, the limits of visual readout may render it impractical for other protein assays that need to quantify analyte concentration.

2.4.2.ii.b Image analysis for electronic readout with mobile phones

Therefore, many assay developers now use electronic readout methods that enable high resolution quantification of analyte independent of the potential bias inherent to visual readout.[22] The reader of choice during early stages of paper-based assay development tends to be a flatbed scanner connected to a computer (for chromophore-labeled assays), which enables taking images with high

spatial resolution,[54] with high bit depth, and most importantly, in a linear colorspace. Fluorophore-labeled assays in early stages of development are often imaged with fluorescence readers such as fluorescence microscopes, gel imagers, or photodiode readers. Both chromophore and fluorophore-labeled assays are amenable to mobile phone readout.[23,45,55,56] Indeed, mobile phones (especially smartphones) are highly portable and are conducive to the development of custom apps for assay quantification, which may be in line with recent US Food & Drug Administration guidelines for mobile healthcare (*e.g.* the Digital Health Innovation Action Plan).[57] Mobile phones are thus amenable to point-of-care imaging of paper-based assays as demonstrated first by the Whitesides group in 2008.[23]

However, several additional factors are relevant when considering coupling an assay to a mobile phone. Mobile phone-imaged assays must contend with the ramifications of rapid update cycles (typically annually), differences between mobile phone camera modules, the use of often eight-bit color channels in saved images, and the automatic post-processing of acquired images. The diversity of mobile phone camera hardware and software performance (and the lack of industry-wide standards) necessarily requires that developers of mobile phone-imaged assays validate assay performance with multiple mobile phone models to ensure generalizability beyond the quirks of a particular phone (which is one limitation of most extant work in mobile phone imaged assays). Aims 2 and 4 (Chapters 4 and 6) of this dissertation explore these factors in greater detail.

Quantitative analysis of a digitally imaged, paper-based assay requires assay developers to identify a region of interest corresponding to where signal develops in the presence of analyte. The developer usually quantifies the mean or representative pixel intensity of the region of interest; subtracts that of a local background region on the lateral flow strip to account for nonspecific binding; and (for fluorophore or phosphor-labeled assays) corrects for nonuniform lighting by dividing by a measure of the illuminance, often a local background region adjacent to the capture region.[16,26] This analysis is typically performed in ImageJ, Adobe Photoshop, MATLAB, or a mobile phone application, among other programs. A standard curve is then fitted to the data, where y is the normalized signal intensity and x is the analyte concentration, usually using a four-parameter (a, b, c, d) logistic curve as in **Equation 2.1**:[16]

Equation 2.1:
$$y = d + \frac{a-d}{\left(1+\frac{\log_{10}(x+2)}{c}\right)^{b}}$$

However, the results from this approach may result in unintentional bias in the results. The sRGB colorspace is the current standard for many digital displays and image file formats. Unfortunately, the sRGB colorspace is nonlinear; the gamma varies from 1 to 2.4 (based on pixel intensity) as shown in **Equation 2.2** and **Equation 2.3**, which show the transformations of linear coordinates (C_{linear}) to sRGB (C_{sRGB}) and vice versa:[58]

Equation 2.2:
$$C_{sRGB} = \begin{cases} 12.92C_{linear} & , C_{linear} \leq 0.0031308 \\ 1.055C_{linear}^{1/2.4} - 0.055 & , C_{linear} > 0.0031308 \end{cases}$$

Equation 2.3:
$$C_{linear} = \begin{cases} \frac{C_{sRGB}}{12.92} & , C_{sRGB} \leq 0.04045 \\ \left(\frac{C_{sRGB}+0.055}{1.055}\right)^{2.4} & , C_{sRGB} > 0.04045 \end{cases}$$

This nonlinearity prevents naïve quantitation with images stored in the native sRGB colorspace, including default photos taken by mobile phone cameras. This is because quantitative imaging (including analyte quantitation) requires a standard curve typically fitted with least-squares regression, which in turn often assumes normally distributed residuals. There are three main methods to address this concern: incorporate the nonlinearity of gamma in the standard curve generation process, linearize the color data, or use a file format with a constant gamma. The latter option is usually used in laboratories that have scientific imaging instruments that natively support raw (DNG) or minimally-processed (TIFF) file formats in a linear RGB, device-independent Lab, or linear sRGB colorspaces.[37,59,60] However, many mobile phone cameras do not natively support such colorspaces, but many Android devices now support exporting photos as raw DNG files and iPhones support saving uncompressed TIFF file photos (albeit in the sRGB colorspace). These factors are explicated in further detail in the mobile phone imaged assays in Aims 2 and 4 (Chapters 4 and 6) of this thesis.

2.5 Assay optimization strategies to improve limit of detection

Improving the limit of detection of a bioassay requires improving not only the optics and physics of detecting the signal of interest, but also the chemistry underlying the assay. Conceptually, this entails increasing the intensity of the signal of interest or reducing the intensity of background noise.

2.5.1 Increasing signal intensity

Conceptually, the simplest way to improve the signal-to-noise ratio is to increase the magnitude of the signal intensity, the numerator. Potential options here include increasing the multiplicity of optical labels to targets via a signal amplification scheme or using optical labels that are intrinsically brighter. While increasing the intensity of the light source (to an extent) could conceivably increase the signal intensity (*e.g.*, for fluorescence or absorbance-based measurements), the background noise may also increase commensurately (if the incident light intensity is increased beyond a critical level, perhaps due to Rayleigh or Raman scattering), which may not necessarily improve signal-to-noise ratios.

Modulating the light intensity with a greater magnitude entails both the selection of an appropriate, "bright" optical label and the selection of an appropriate wavelength at which measurements are made. For example, one novel readout method that may markedly enhance the analytical sensitivity and limit of detection of lateral flow assays is thermal readout by measuring infrared emission from binding events at roughly 10 μm wavelengths in lieu of traditional visible light measurements in the sub-micron wavelength regime, which only measure absorbance of the bulk nanoparticle rather than detection of the binding event itself. The reader may consist of commercial smartphone thermal camera dongles, which could be used to image a standard gold nanoparticle based lateral flow assay with no modifications to the bioassay itself. Proof-of-concept has been demonstrated by the Bischof group, who have demonstrated a factor of ten improvement in the limit of detection compared to visible wavelength imaging of gold nanoparticle-labeled assays.[33,40]

Many labeling approaches conjugate labels to recognition moieties at a one-to-one or lower basis, wherein a single optical label binds on average to one or more analyte molecules. One way to increase the signal intensity is to increase the number of optical labels bound to each analyte,[30,41,61] either by selecting an appropriate linker that can bind to multiple epitopes of the analyte;[26] by designing the linker so that multiple optical labels may bind to the linker;[29] or by coupling nucleic acid amplification to protein detection via immuno-polymerase chain reaction strategies,[62,63] among

other approaches. For example, the HRP-DAB system should improve the signal-to-noise ratio compared to gold nanoparticle-based labels because a single HRP ligated to an analyte could produce hundreds or thousands of colored products; the signal could be increased even further by using the streptavidin-biotin linkage system due to the four binding sites that streptavidin (and avidin) has for biotin.[29] In theory, the signal amplification strategy should increase the signal intensity by a factor up to the multiplicity of the label to analyte. In practice, however, amplification improves the analytical sensitivities and limits of detection of lateral flow assays by a factor less than the theoretical increase implied by the multiplicity, likely due to a commensurate increase in background intensity. [26,29,62]

2.5.2 Reducing background intensity

It is difficult to detect low levels of a signal of interest against high levels of a background signal. Among other factors, elevated background signal may be due to the choice of optical label or reader, to nonspecific binding of the detecting molecule or optical label, or to the intrinsic brightness of the highly scattering paper substrate. Use of optical labels that are visualized against a bright background typically leads to a reduction in an assay's analytical sensitivity, as is the case for chromophoric and chromogenic labels against the typically white nitrocellulose membrane used in lateral flow assays. Since external lighting is needed for such assays, the reflected background white signal from the membrane overwhelms the optical reader, thereby reducing the signal-to-background ratio of the assay. In contrast, a luminescent optical label imaged against a low-background (*e.g.* a low-autofluorescence material) may have an improved signal-to-background ratio, which in turn may improve the assay's analytical sensitivity and limit of detection.[44]

Reducing nonspecific binding tends to be a more delicate process that involves optimizing the assay biochemistry following insights gained in enzyme-linked immunosorbent assays (ELISA). Since the nitrocellulose membrane used in lateral flow assays adsorbs proteins well and typically has a negative surface charge similar to an ELISA plate, there is a potential for the optical label or for the intermediary linker (detecting antibody, binder, or aptamer) to bind nonspecifically to the membrane.[26] Therefore, the lateral flow membrane is often blocked with proteins such as BSA,[64,65] the isoelectric point of the intermediary linkers are optimized,[26] and vigorous wash steps with an appropriate buffer (*e.g.* phosphate-buffered saline with added surfactant and blocking protein) are included in the assay procedure.[17,42] In addition, the chemical bonds between the intermediary linker and optical label can be optimized themselves. The linker and label must be either covalently or noncovalently bound to each other, for instance via strong, noncovalent streptavidin-biotin interactions, among others.[66] Theoretically, noncovalently bound optical labels may be susceptible to dissociation in harsh conditions such as in the flow regimes present in lateral flow assays during wash or rinse steps, which may in turn reduce the signal-to-noise ratio. While a covalent bond between the linker and label is preferable due to its immutability ($k_{off} \sim 0$), noncovalent interactions are more commonly utilized since they too are conducive to modularly designed assays and interface well with commercially available reagents such as conjugated antibodies.

2.6 Gaps in the literature

There are several gaps in the literature that impede the design and translation of suitable infectious disease diagnostic tests to the point of care. Extant assays either prioritize sensitivity at the expense of instrument size and cost (*e.g.* the Gene Xpert platform and Quanterix Simoa protocols) or emphasize portability and low cost but with poor sensitivity (such as many paper-based assays including lateral flow tests). The ubiquity of mobile phones coupled with recent advances in mobile

phone camera hardware suggest that phones are uniquely suited to improve the sensitivity of current paper-based, optically labeled assays. However, previous work in coupling mobile phones to paper-based assays have not fully exhausted the capabilities of mobile phone cameras to image fluorescence in clinically relevant bioassays. This dissertation addresses these gaps by exploiting the built-in optical filters in mobile phone cameras to enhance the analytical performance and expand the capabilities of mobile phone-imaged fluorescence assays. The aims which comprise this thesis:

- Enumerate the wavelengths and lifetimes of paper autofluorescence to enable rational screening of the porous media on which assays are performed (*i.e.* improve assay performance by reducing background intensity contributed by substrate autofluorescence).
- Ratiometrically image a fluorophore with a mobile phone without any external optical filters while simultaneously improving the limits of detection of a clinically relevant immunoassay (*i.e.* improve limits of detection by increasing signal intensities while simultaneously reducing background intensity without substantially increasing cost).
- Heat a disposable cartridge for bacterial lysis and nucleic acid amplification from below with a single disposable, USB-powered printed circuit board heater while enabling real-time imaging with a mobile phone.
- Image two fluorophores simultaneously with a mobile phone to implement colocalized positive controls in a fluorescence-labeled, isothermally amplified assay for nucleic acids (*i.e.* improve nucleic acid assay time to result while reducing false negatives).
- Translate some of the benefits of digital nucleic acid amplification tests to assays performed in paper by optically segmenting real-time mobile phone images into blocks that improve signal-to-noise ratios.

3 Develop a screening strategy to enhance the analytical performance of paper-based fluorescence assays

"*Fiat lux*."

"Let there be light."
– Genesis 1:3 and the motto of the University of Washington ("*Lux sit*").

3.1 Summary

3.1.1 Abstract

Porous media made of nitrocellulose and glass fiber are common "paper" substrates for lateral flow assays, microfluidic paper analytical devices, and other point-of-care diagnostic assays. Such assays commonly use optical labels such as gold nanoparticles, latex beads, or fluorescent nanoparticles to visualize the presence of analytes. Fluorescent labels are commonly used in bioassays to enhance sensitivity, but autoluminescence of the paper substrate worsens signal-to-noise ratios of fluorescence-based assays. To date, there exists no systematic investigation of autoluminescence wavelengths or lifetimes of porous membranes used in lateral flow assays. In response, we quantified the autoluminescence of commonly used porous materials across the visible spectrum *via* excitation-emission spectroscopy and time-resolved fluorescence spectroscopy, and demonstrate that autoluminescence is solely due to autofluorescence with lifetimes of about 5 ns in the visible spectrum. Counterintuitively, we found that spectroscopy alone does not provide sufficient information to select candidate paper substrates for fluorophore-labeled assays. Therefore, we developed a simple quantitative framework to select a low-fluorescence substrate that minimizes both the overlap of paper and fluorophore emission spectra and the fluorescence intensity on an imaging system of interest (such as a gel imager). Use of this framework was shown to lower the limit of detection of an influenza A nucleoprotein immunoassay by over 50%. The tools developed in this section enable screening appropriate, low-fluorescence porous substrates to enhance the sensitivity of membrane-based fluorescence assays.

3.1.2 Contributions to the academic literature

Parts of this aim contributed to the academic literature as a conference poster and journal article:

- Shah K, Kauffman P, and Yager P. Fluorescence improves the sensitivity of paper microfluidics: 1) Account for paper autofluorescence and 2) Image with a mobile phone. Gordon Research Seminar, Poster, 2017. Tuscany, Italy.
- Shah K, Kauffman P, and Yager P. Fluorescence improves the sensitivity of paper microfluidics: 1) Account for paper autofluorescence and 2) Image with a mobile phone. Gordon Research Conference, Poster, 2017. Tuscany, Italy.

3.2 Introduction

Many lab-on-a-chip systems intended for point-of-care diagnostics are comprised of one or more porous media fabricated from nitrocellulose, glass fiber, and cellulose. Such devices use one or more of these "paper" substrates for their low cost, reproducibility, suitability for low sample or buffer volumes, and compatibility with biological samples, among other potential benefits.[21,42,67] For example, commercial point-of-care tests for pregnancy or for HIV antibodies consist of lateral flow assays that use a porous nitrocellulose membrane to support capture molecules. These assays typically employ optically-absorbing labels such as gold nanoparticles to visualize the presence of an analyte,[17] but these absorbance-based labels suffer from poor analytical performance due to the low signal-to-background ratio associated with measuring a signal against the bright, highly scattering background of the substrate. To address this limitation, luminescent detection labels (fluorophores or phosphors) have been used to enhance limits of detection and analytical sensitivities. Several assays developed recently have demonstrated the effectiveness of these luminescent detection labels to enhance the analytical performance of paper-based assays compared to chromophore labels. Indeed, assays utilizing fluorophore or phosphor labels show a factor of ten or greater limit of detection improvement compared to traditional chromophores such as gold nanoparticles.[4,32,44,45,56] Such improvements are orders of magnitude worse than the several orders of magnitude improvement in sensitivity observed in microscopy of transparent samples upon switching to fluorescent labels. Autoluminescence of paper substrates is the main cause of this performance discrepancy as noted by Hollas and Kopf.[68,69] Efforts to mitigate paper autoluminescence have included developing low-fluorescence alternative substrates, labeling with upconverting phosphors in lieu of fluorophores, utilizing brighter labeling schemes, and using time-gated imaging, but these approaches are costly and require complex instrumentation.[70,71]

To our knowledge, most commercial porous membranes made of glass fiber, cellulose, nitrocellulose, and polyvinylidene difluoride (PVDF) emit significant fluorescence in the blue, yellow, and green regions of the visible spectrum, thereby worsening the analytical performance of paper-based luminescence assays. Beyond such assays, the autofluorescence of nitrocellulose in particular has broader implications for reducing the sensitivity of western blots and protein visualization on nitrocellulose slides.[69] Although the autofluorescence of these commercial porous media is widely acknowledged, there have been no studies that definitively quantify the autofluorescence spectra or lifetime(s) of common paper substrates. This gap in the literature has hindered the development of highly sensitive fluorophore-labeled assays because assay developers have been unable to select an optimal low-fluorescence paper substrate.

Recent work from the Klapperich group has shown the importance of paper substrate selection in biological assays as certain materials will hinder the performance of nucleic acid amplification-based assay biochemistries.[72] Similarly, Lee et al. have shown that membrane selection strongly impacts lateral flow assay performance due to differences in flow speed between membranes.[73] Our group has had similar experiences. In this paper, we extend the idea that materials selection strongly impacts assay performance by systematically characterizing paper autofluorescence and assessing its impact on fluorescence-based assay performance. We applied excitation-emission fluorescence spectroscopy to characterize the fluorescence spectra of materials across all combinations of excitation and emission wavelengths in the visible spectrum; the data are visualized as excitation-emission matrices (EEMs), which follows the work of McKnight, Coble, and others in the environmental testing literature.[74–76] Beyond simple materials characterization, we demonstrate the usefulness of EEMs when selecting an appropriate low autofluorescence substrate during assay

development: We propose use of an "autofluorescence index" as a simple metric to rank papers and validate this with a quantum dot-labeled lateral flow assay for the quantitative detection of influenza A nucleoprotein previously developed in our lab. It is the aim of this specific aim to provide assay developers with a simple, quantitative framework to screen substrate materials to enhance sensitivity, potentially reducing time-consuming assay optimization.

3.3 Methods

3.3.1 Survey of autofluorescence in materials commonly used in paper-based assays

Twelve materials that are commonly utilized in paper-based diagnostic assays were identified from the literature and from those known to have minimal autoluminescence, as shown in **Table 3.1**. Samples of each material were cut to approximately 35 by 14 mm rectangles and placed diagonally in polymethacrylate fluorimeter cuvettes (Sigma-Aldrich C0793, lot 3110). Four milliliters of water were added to each cuvette, which was placed in a fluorimeter (Perkin-Elmer LS-50B) rotated fifteen degrees counterclockwise to minimize direct specular reflection of excitation light into the detector from the surface of the porous materials. Spectra were converted to comma-separated values with Spekwin32 version 1.72.2.

Table 3.1: List of porous materials evaluated

Nitrocellulose	Glass fiber, cellulose, and other	
GE FF80	Ahlstrom 8950	GE Whatman 1
GE Immunopore FP	Ahlstrom 8964	Millipore C083
Millipore HF120	GE Fusion 5	Pierce PVDF
Millipore HF135	GE Standard 17	Sterlitech PES

Excitation-emission matrices (EEMs) were acquired for each material and for Raman-scattering (pure water) and fluorescence (ThermoFisher Qdot 605-streptavidin conjugate diluted to 50 nM, lot 1801968) controls; emission was swept at 400 nm/min from 300 to 650 nm in 0.5 nm increments with a 2.5 nm emission monochromator slit width, and excitation was characterized from 300 to 650 nm in 10 nm increments with a 2.5 nm excitation monochromator slit width. An EEM was also obtained in phosphorescence mode (1 ms delay) for Millipore HF120 nitrocellulose. The EEMs were processed to remove first order and second order Rayleigh scattering with a custom MATLAB script available in the files supplementing this document. Briefly, any emission within 25 nm of the excitation wavelength was masked for removal; the filtered data was reconstructed by local linear interpolation along the emission axis (y-axis) for each excitation wavelength (x-axis). In addition, the EEMs were corrected for the sensitivity of the detector for each emission wavelength and for variations in brightness of the Xe excitation source.

Fluorescence lifetimes of Millipore HF120 and GE Standard 17 were measured with transient absorption and photoluminescence spectroscopy (Ultrafast Systems). Briefly, the excitation source was a Coherent Libra amplified Ti-Sapphire laser (50 fs pulses of 800 nm light at 1 kHz) that underwent optical parametric amplification and bandpass filtering to 365 nm. Samples were mounted in an epifluorescence configuration in a cuvette with Millipore water to minimize excitation artifacts, and fluorescence emission photons were measured with a streak camera to elucidate the temporal fluorescence kinetics (0.18 to 200 ns) throughout the visible spectrum (400 to 650 nm). Data were processed with a custom MATLAB script to window data into rolling 10 nm moving

sums to generate decay curves, perform numerical integration with the trapezoidal rule, and fit single-exponential decay curves to compute 1/e (36.8%) fluorescence decay times.

The autofluorescence of each paper was also measured in transmission mode at 300 nm excitation with a gel imager (Bio-Rad Gel Doc EZ Imager with UV tray, 12-bit monochromatic charge-coupled device) set to 0.75 second exposure. Photos were analyzed with ImageJ, and the average and standard deviation of pixel intensity was quantified for each paper. The autofluorescence of each paper was ranked by developing the "autofluorescence index," a quantitative measure that accounts both for spectral emission variations and for the imaging optics used in an assay (see below). Two microliter spots of Qdot 605-streptavidin were pipetted onto dried nitrocellulose membranes and were imaged with a 2.5 second exposure on the gel imager.

3.3.2 Application to a quantum dot-labeled lateral flow assay

The impact of paper substrate autofluorescence on assay analytical performance was assessed by performing an influenza A nucleoprotein lateral flow assay on the five hydrophilic membranes with protein-binding capacity: GE FF80, GE Immunopore FP, GE Fusion 5, Millipore HF120, and Millipore HF135. Lateral flow strips were manufactured in-house *per* the following procedure. Each membrane was cut to a sheet approximately 3.8 cm by 20 cm, and lateral flow cards were assembled by overlapping 1.3 cm of each membrane with the exposed adhesive of 2 mil-thick, 5 cm by 20 cm, adhesive-backed Mylar (Fralock). Millipore C083 cellulose was used as a wicking pad by cutting cellulose cards to 5 cm by 20 cm and then placing on the cards top of the adhesive so that about 1.3 cm of the cellulose cards overlapped with the protein-binding membrane. Anti-influenza A nucleoprotein monoclonal antibodies were striped in the capture region (Hytest InA108, lot 14/04-IN5-A108, 5.8 mg/mL) and anti-mouse IgG was striped in the control region between the capture region and the wicking pad (Jackson ImmunoResearch AffiniPure Goat Anti-Mouse IgG, lot 125769, 1 mg/mL) at 0.35 μL/s and 35 mm/s (Biodot Biojet HR Solenoid Dispenser). Striped cards were stored at 37 °C for 2 hours, cut to 3 mm-wide strips, and stored at 25% relative humidity at 21 °C overnight.

Lateral flow strips were run by sequentially dipping the cut lateral flow strips into six wells of a 96-well plate until the fluid was drawn from each well (3-10 minutes per well, total ~35 minutes). The solutions consisted of: 1) 20 μL of recombinant influenza A nucleoprotein with histidine tag (Brisbane/10/2007 (H3N2), Influenza Reagent Resource, Influenza Division, WHO Collaborating Center for Surveillance, Epidemiology and Control of Influenza, Centers for Disease Control and Prevention, Atlanta, GA, USA, lot 59245888) diluted into lateral flow assay running buffer (10 mM phosphate-buffered saline, 1% w/v bovine serum albumin (Sigma Aldrich A3294, lot SLBR0419V), and 0.05% v/v Tween-20 (Sigma-Aldrich P7949, lot SLBK8628V)) with 5% Triton X-100; 2) 15 μL of lateral flow assay running buffer; 3) 10 μL of detecting antibody (HyTest 3IN5B InA245, lot 15/11-IN5B-A245) at 1.7 mg/mL; 4) 15 μL of lateral flow assay running buffer; 5) 10 μL of streptavidinylated quantum dots (ThermoFisher Qdot 605 Streptavidin Conjugate, lot 1801968) diluted into lateral flow assay running buffer with 5% Triton X-100; and 6) 40 μL of the lateral flow assay running buffer with 5% Triton X-100. The lateral flow strips were dried at room temperature for two hours and photographed in transmission mode with the gel imager as before at a 0.75 second exposure and 300 nm excitation. A custom MATLAB script was used to identify and

quantify the average and standard deviation of the signal intensity of the capture region of each strip. A previously-developed script then fitted a four-parameter logistic curve to the signal intensities for each sample, quantify limits of detection with 95% confidence intervals, and calculate t-statistics comparing the limits of detection for assays run on each substrate for type I (α) and type II (β) error rates set to 1%.[16] Correlation between the limits of detection and substrate autofluorescence was assessed with the right-tailed Spearman rank correlation coefficient.

3.4 Results

3.4.1 Characterizing autofluorescence lifetimes and wavelengths

Autoluminescence of a representative porous substrate, Millipore HF120 nitrocellulose, was characterized by time-resolved fluorescence spectroscopy and excitation-emission spectroscopy. **Figure 3.1a** visualizes fluorescence lifetime kinetics of wet nitrocellulose centered at 605 nm, which was observed to undergo single-exponential fluorescence decay with a dominant lifetime of about 4 ns. Similarly, short lifetimes of 2-5 ns were observed throughout the visible spectrum; wet nitrocellulose consistently had a shorter lifetime than dry nitrocellulose (**Figure 3.1b**). No long-lifetime phosphorescence emission was seen as visualized in the excitation-emission matrix in **Figure 3.1c**, which was confirmed by excitation-emission spectroscopy with a 1 ms delay on a conventional commercial luminescence spectrometer. Autofluorescence lifetimes in glass fiber membranes was similar to that in nitrocellulose; the lifetime in GE Standard 17 was 3-7 ns in the visible spectrum for both wet and dry membranes.

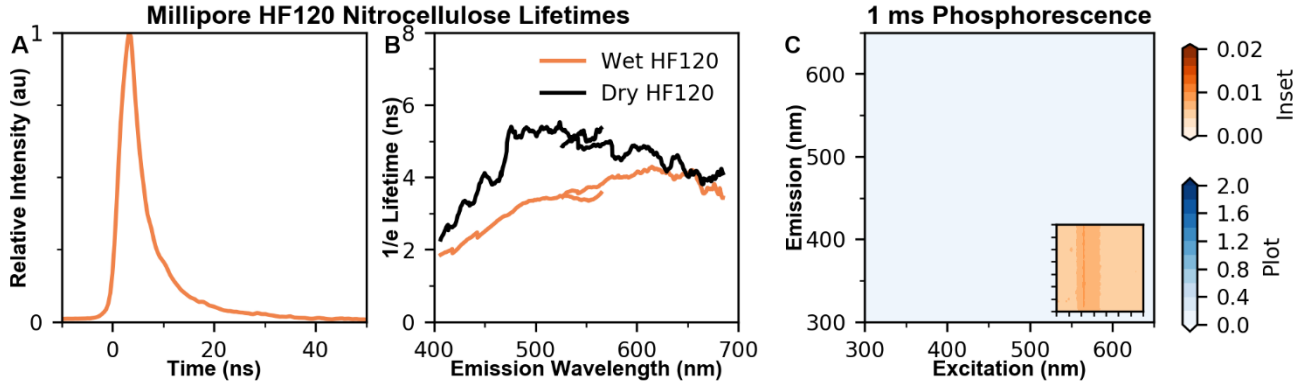

Figure 3.1: Luminescence characteristics of Millipore HF120 nitrocellulose. (**a**) Time-resolved luminescence spectrum of wet HF120 between 595 and 615 nm when excited by a 50 fs, 365 nm pulse. (**b**) Fluorescence lifetimes as a function of wavelength with 10 nm window (for 365 nm excitation). (**c**, inset) Excitation-emission spectrum confirms the lack of strong long-lifetime phosphorescence.

Figure 3.2 shows fluorescence EEMs for several other nitrocellulose membranes commonly used in paper-based assays or for protein visualization. EEMs visualize autofluorescence at all combinations of excitation (horizontal axis) and emission (vertical axis) wavelengths; traditional excitation and emission spectra correspond to horizontal and vertical cross-sections of each EEM, respectively.

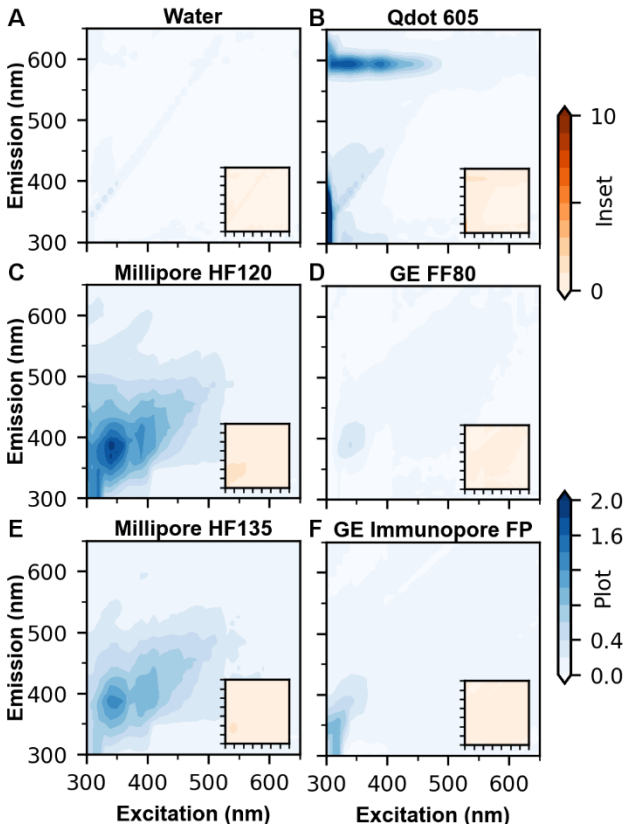

Figure 3.2: Excitation-emission matrices visualize absolute fluorescence emission (unitless) in 0.5 nm increments for excitation wavelengths swept in 10 nm increments. The spectra shown in each subpanel are of: (**a**) Water, a Raman scattering control; (**b**) Qdot-605, a fluorescence control; (**c**) Millipore HF120 nitrocellulose; (**d**) GE FF80 nitrocellulose; (**e**) Millipore HF135 nitrocellulose; and (**f**) GE Immunopore FP nitrocellulose. Insets show fluorescence spectra between 300 and 650 nm with a larger z-axis dynamic range. Details of data processing, including Rayleigh scattering suppression, are in the accompanying text.

First and second-order Rayleigh/Mie scattering artifacts were observed as diagonal striations of high signal intensity at integer multiples of the excitation wavelength, which were removed as shown in **Figure 3.3**. Raman scattering was not directly observed in the fluorescence EEMs for any material (Raman intensities weaken with increasing excitation wavelength, are offset from the excitation by a constant wavenumber, and the angle of Raman lines on an EEM graph is steeper than Rayleigh/Mie scattering artifacts). No Raman scattering was also observed for the cellulose, glass fiber, and alternate materials evaluated (**Figure 3.4**).

All twelve paper materials emitted autofluorescence across all emission wavelengths, especially below 500 nm. Many materials were observed to have windows of low autofluorescence, especially for emission wavelengths between 550 nm and 650 nm. The autofluorescence of all tested porous membranes was observed to occur as a single, distinct peak typical of fluorophores such as quantum dots (**Figure 3.2**, **Figure 3.4**).

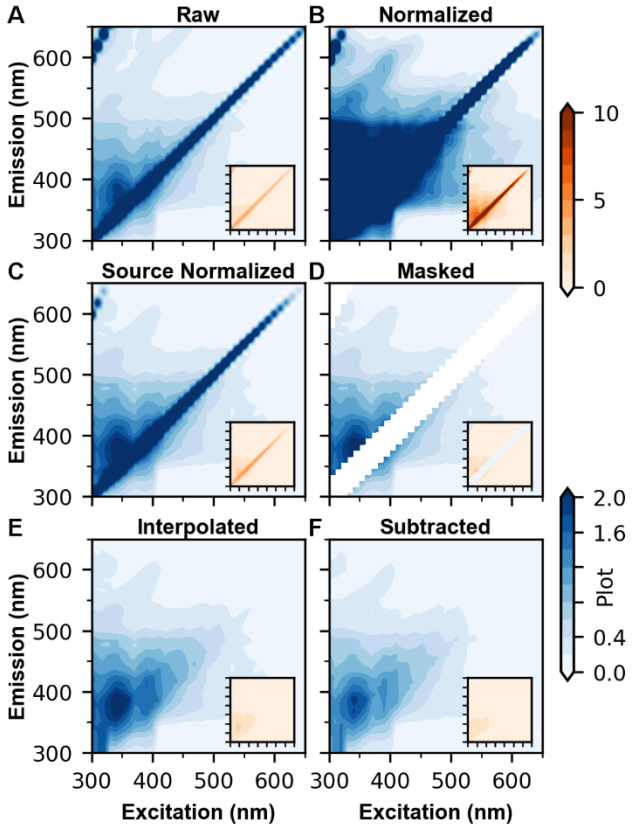

Figure 3.3: Summary of excitation-emission matrix (EEM) data processing for Millipore HF120 nitrocellulose. Z-axis shows fluorescence intensity at each excitation and emission wavelength pair. Insets show z-axis across a wider dynamic range. (**a**) Raw EEM as acquired by fluorimeter; (**b**) EEM normalized to photomultiplier tube spectral sensitivity; (**c**) EEM normalized by excitation source sensitivity; (**d**) EEM with first- and second-order Rayleigh scattering masked; (**e**) EEM with masked values linearly interpolated; and (**f**) EEM after subtracting that of a blank cuvette.

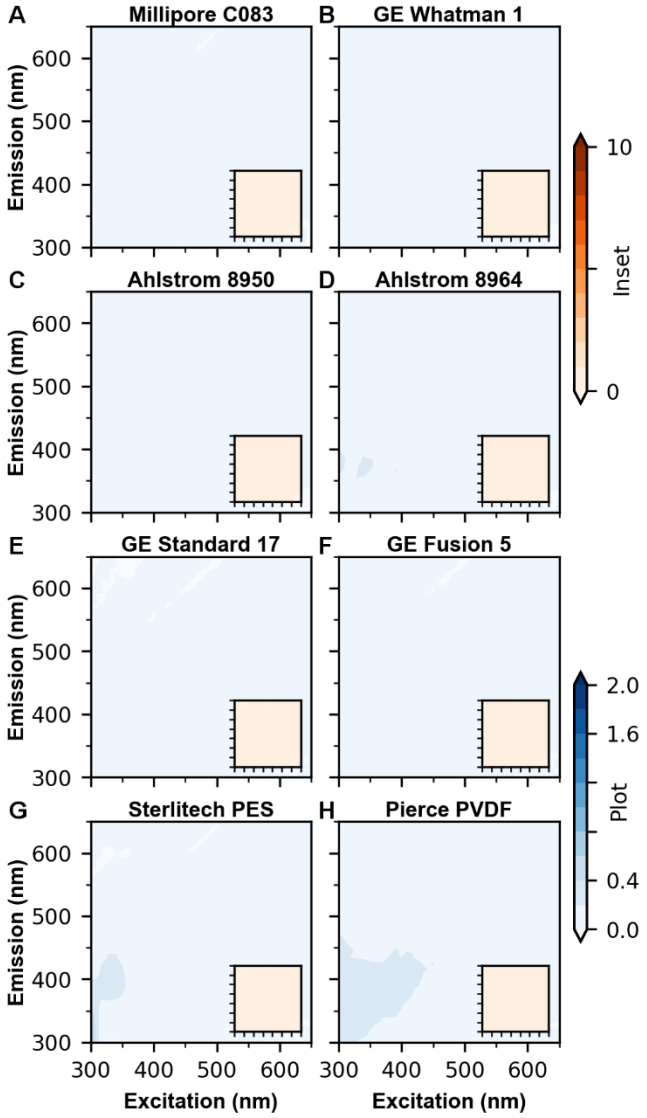

Figure 3.4: Excitation-emission matrices of several non-nitrocellulose paper membranes commonly used in paper microfluidics: (**a**) Millipore C083; (**b**) GE Whatman 1; (**c**) Ahlstrom 8950; (**d**) Ahlstrom 8964; (**e**) GE Standard 17; (**f**) GE Fusion 5; (**g**) Sterlitech Polyethersulfone; and (**h**) Pierce Polyvinylidene Difluoride. Z-axis shows fluorescence intensity at each excitation and emission wavelength pair. Insets show z-axis across a wider dynamic range.

3.4.2 Hadamard product integral quantifies autofluorescence

Typically, fluorescence assay developers use the emission spectra of porous substrates and of fluorophore(s) of interest to identify a substrate and fluorophore pair with minimal overlap of emission spectra; if multiple substrates appeared suitable, then the material with the lowest fluorescence intensity (peak or area-under-the-curve) would be selected for a given assay. However, such an approach does not always work in practice because the optical characteristics of the fluorescence reader used in the final assay must also be considered: these factors include the optical path, optical filters, spectral emission distribution of the excitation source, and spectral sensitivity of the detector, among others. Similarly, imaging a substrate of interest to quantify its autofluorescence is not sufficient on its own as spectral characteristics of the fluorophore and paper are not accounted for. Indeed, a cursory glance at the EEMs in **Figure 3.2** suggest that GE FF80 should be

used in lieu of Millipore HF120 nitrocellulose when visualizing Qdot-605 because GE FF80 appears to emit less autofluorescence than Millipore HF120 and other nitrocellulose membranes. However, in practice, the opposite phenomenon is observed as shown in **Figure 3.5**. An aliquot of Qdot 605-streptavidin is not visible on GE FF80 due to its autofluorescence, but the quantum dots are visible on three other nitrocellulose membranes when imaged with a gel imager under UV excitation.

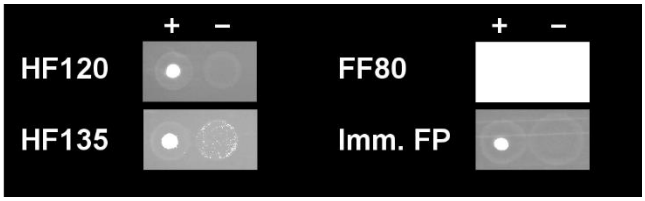

Figure 3.5: Imaged spots of quantum dots on dried nitrocellulose membranes (Millipore HF120, GE FF80, Millipore HF135, and GE Immunopore FP) at fixed exposure settings illustrates that fluorescence emission spectra alone cannot screen materials. A 10 fmol spot of Qdot-605 (+) or negative control (-) is visible on all nitrocellulose membranes except GE FF80, even though GE FF80 appears to emit the least autofluorescence based on emission spectra alone.

Therefore, we developed a quantitative framework to enable assay developers to identify which paper(s) may be suitable for use with a particular fluorophore label. An autofluorescence index was developed to quantify the fluorescence intensity of each paper based on its spectral distribution and luminescence on an imaging system of choice. Definition of the autofluorescence index was guided by the principle of parsimony and *a priori* design criteria that stipulated that the autofluorescence index should be greater for papers with emission spectra that overlap more with a fluorophore's emission and that the autofluorescence index should be greater for papers that appear brighter on a given imaging system. The spectral component of the autofluorescence index was quantified with the Hadamard product (for details on the Hadamard product, refer to Horn[77]), which is simply the pointwise product of the emission spectra of the specific porous material and the fluorophore in question (**Equation 3.1**).

Equation 3.1: $$\boldsymbol{Hadamard\ Product}\ (\lambda_i) = \boldsymbol{Paper}_{em\ curve}(\lambda_i) \circ \boldsymbol{Fluorophore}_{em\ curve}\ (\lambda_i)$$

Equivalently, we could apply the convolution theorem and convolve the paper emission spectra with the fluorophore emission spectrum in Fourier space (**Equation 3.2**):

Equation 3.2: $$\boldsymbol{Hadamard\ Product}\ (\lambda_i) = \mathcal{F}^{-1}\left(\mathcal{F}\left(\boldsymbol{Paper}_{em\ curve}(\lambda_i)\right) * \mathcal{F}\left(\boldsymbol{Paper}_{em\ curve}(\lambda_i)\right)\right)$$

As shown in **Equation 3.3**, the Hadamard product was then integrated across the near-ultraviolet and visible spectrum and normalized by the integrals of the paper and fluorophore emission curves to eliminate instrument artifacts and run-to-run variation. The bounds were set at 400 and 650 nm because our imaging system (a gel imager) had a detector sensitive to wavelengths greater than ~400 nm and our fluorimeter was sensitive in the visible range up to 650 nm.

Equation 3.3: $$\boldsymbol{Norm.Hadamard\ Product} = \frac{\int_{400\ nm}^{650\ nm} \boldsymbol{Hadamard\ Product}\ (\lambda_i)\ d\lambda}{\int_{400\ nm}^{650\ nm} \boldsymbol{Paper}_{em\ curve}(\lambda_i)\ d\lambda \int_{400\ nm}^{650\ nm} \boldsymbol{Fluorophore}_{em\ curve}(\lambda_i)\ d\lambda}$$

The autofluorescence index was then defined as the product of the normalized Hadamard product with the average luminescence intensity of each paper, as measured on an optical setup (*e.g.* scanner, mobile phone, camera, or gel imager) used to read assays, which was a gel imager in this case (**Equation 3.4**).

Equation 3.4: $$\textit{Auto-fluorescence index} = \textit{Average luminescence} \cdot \textit{Norm. Hadamard product}$$

We quantified the autofluorescence index of the membranes used to run the lateral flow assay for excitation at 300 nm and visualizing Qdot 605-streptavidin (**Table 3.2**).

Table 3.2: Correlation of autofluorescence index with assay limits of detection.

		Assay limit of detection†	
	Autofluorescence index† (au)	**Signal domain (au)**	**Concentration domain (fmol)**
Millipore HF120	7.63-8.55	0.61–0.65	59–105
GE Immunopore FP	12.75-14.26	2.12-2.20	Undefined
Millipore HF135	9.75-11.80	0.67–0.79	135–232
GE FF80	17.49-19.97	0.79–0.92	87–306
Spearman's rho		0.78 (p=0.001)	

†Values indicated are 95% confidence intervals; the dynamic range of the assay in the signal domain is from 0–1 units

3.4.3 Improved limit of detection of fluorescence-based lateral flow assay

A quantum-dot-labeled lateral flow immunoassay for influenza A nucleoprotein was performed to validate the application of membrane autofluorescence concepts developed in this specific aim (**Figure 3.6a**). Representative photos of the lateral flow assay on Millipore HF120, Millipore HF135, GE FF80, and GE Immunopore FP nitrocellulose are shown in **Figure 3.6b**. An exposure time of 0.75 seconds was used as longer exposure times resulted in a saturated image (as in **Figure 3.5**). The streptavidin-labeled quantum dots did not flow in GE Fusion 5, which prevented obtaining a standard curve of the assay on this membrane. The intensity of the capture line was quantified at a range of input nucleoprotein concentrations on the other four membranes, and four-parameter logistic fits were fitted to generate standard curves of quantified signal intensity against concentration. A representative standard curve on Millipore HF120 is shown in **Figure 3.6c**.

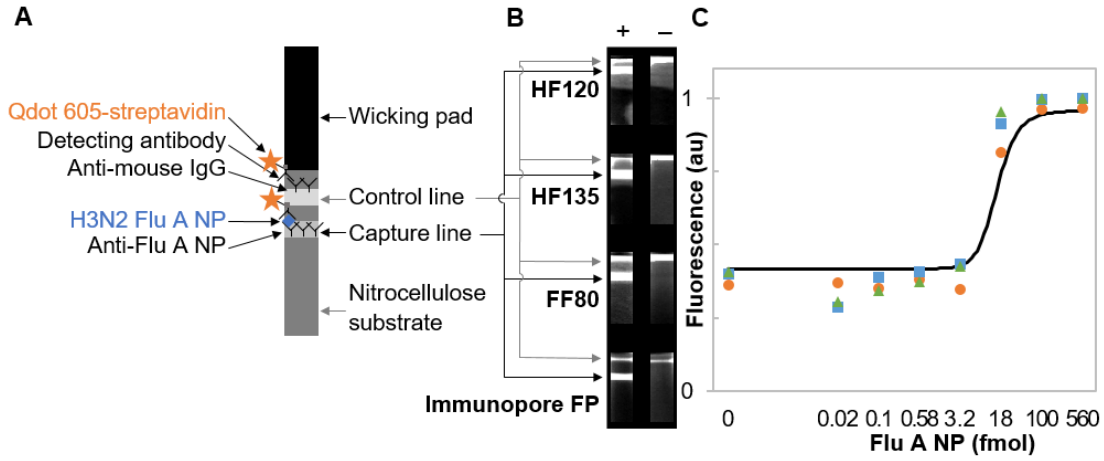

Figure 3.6: Assessment of an influenza A nucleoprotein (NP) assay on nitrocellulose substrates with varying levels of autofluorescence to validate effect of paper autofluorescence on assay performance. (**a**) Cartoon of the assay stack, (**b**) photos of representative positive (left) and negative (right) lateral flow strips on each nitrocellulose substrate, (**c**) representative standard curve on Millipore HF120.

The limits of detection of the standard curves for each membrane are shown in **Figure 3.7a** along the standard curve vertical axis and in **Figure 3.7b** along the standard curve horizontal axis. The assay was observed to have the lowest limit of detection on HF120 (along both axes). Materials with lower autofluorescence tended to have lower (better) limits of detection in the signal domain (vertical axis of standard curve) (Spearman's rho=0.78, p=0.001).

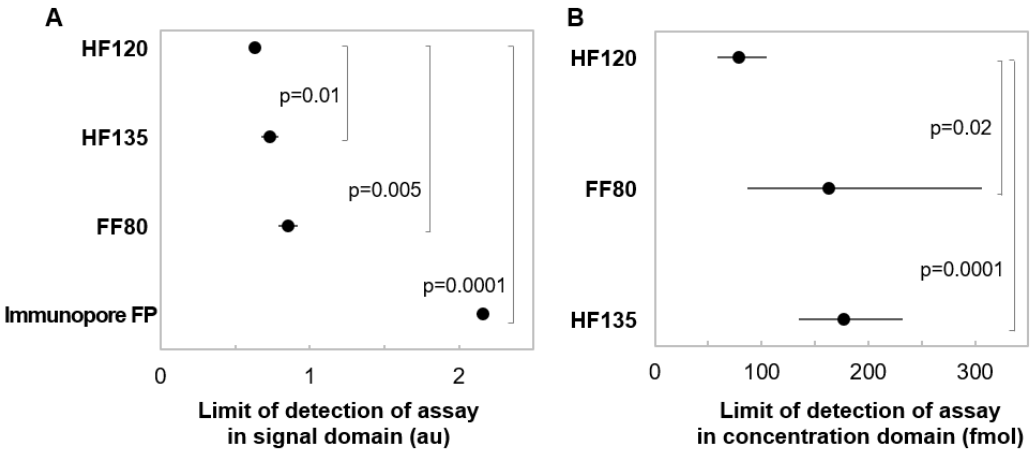

Figure 3.7: Limits of detection of quantum dot-labeled influenza A nucleoprotein assay on various nitrocellulose substrates. (**a**) Limit of detection in the signal domain (vertical axis of standard curve) and (**b**) concentration domain (horizontal axis of standard curve). Average limit of detection and 95% confidence intervals are plotted and p-values from Welch's t-test are indicated for pairwise comparisons of the limit of detection on each paper to HF120. The limit of detection on Immunopore FP was beyond the assay's dynamic range (0 to 1 in signal domain).

3.5 Discussion

Fluorescence-labeled assays performed in paper microfluidic devices suffer from poor limits of detection due to the intrinsic autoluminescence of paper. While the paper microfluidics literature widely acknowledges the scope of this problem, prior attempts to address this limitation have often resorted to time-resolved spectroscopy (using fluorescence decay curves as in **Figure 3.1a** to distinguish a particular fluorescent label) or changing the assay detection chemistry (with custom phosphorescent detection labels to bypass autofluorescence).[32,71] To our knowledge, there exist no strategies to mitigate paper autoluminescence while maintaining extant assay detection chemistries. Here, we present a simple framework to reduce the impact of autoluminescence on extant fluorescence assays without changing the detection chemistry; provide the first systematic, quantitative investigation of paper autoluminescence; and demonstrate that the autoluminescence of porous media is due mainly to autofluorescence.

Common contributors to luminescence include fluorescence, phosphorescence, and Raman scattering (Tyndall and Brillouin scattering are often too weak to measure, and Rayleigh scattering is often eliminated via optical filtering). The absence of diagonal steaks in the excitation-emission matrices in **Figure 3.2** excludes Raman scattering as a strong contributor of paper autoluminescence. Similarly, long-lifetime phosphorescence is excluded by the lack of measured photons beyond 50 ns in the fluorescence lifetime curve in **Figure 3.1a** and the absence of signal in **Figure 3.1c**. Therefore, we attribute autoluminescence of porous media mainly to autofluorescence at the wavelengths indicated in **Figure 3.2** and lifetimes indicated in **Figure 3.1**. While the autofluorescence wavelengths are similar to those reported previously in the literature, the lifetimes

obtained herein are orders of magnitude below the 20-40 μs previously documented.[71] We attribute this discrepancy to improved time-gating in this work as enabled by a pulsed femtosecond laser excitation source and precision high-speed optics.

We developed the autofluorescence index with two key properties in mind: calculation ought to be sufficiently simple to enable screening papers for a fluorescence-labeled assay while simultaneously having a mathematically robust foundation. **Equations 3.1-3.4** efficiently embody these properties by reducing the autofluorescence index calculation to four simple steps: take the pointwise product of emission spectra, approximate the area under the curve, normalize for the fluorimeter, and normalize for the imaging setup. Conceptually, the autofluorescence index is comprised of two components, which are 1) the spectral overlap between a paper's emission spectrum with that of a fluorophore of interest and 2) the luminescence observed on an imaging system of interest (which encompasses characteristics such as the excitation source, optical filters, detector sensitivity, light path, *etc.*). In effect, the autofluorescence index serves a nondimensional number that predicts the ease of observing a fluorophore on a paper.

Intuitively, the autofluorescence index ought to be lower for materials with fluorescence emission that minimally overlaps with the emission of a fluorophore of interest, and should also be lower for materials that appear dimmer in a particular imaging system. Moreover, materials with lower autofluorescence indices would be expected to have better analytical performance in an assay, which is validated in **Table 3.2**—the autofluorescence index is shown to quantitatively correlate with assay limits of detection despite the complexities inherent to a biochemical assay. This correlation holds true in the signal domain (y-axis of the standard curve in **Figure 3.6c**), whereby papers with lower autofluorescence indices have improved limits of detection ($p=0.001$). While no similarly broad statement may be made about the correlation of autofluorescence index with the limits of detection in the concentration domain (x-axis of the standard curve), the paper with the lowest autofluorescence index, Millipore HF120, also had the lowest limit of detection in the concentration domain compared to each of the other nitrocellulose substrates ($p<0.05$). One potential variable that could have confounded the observed trend between autofluorescence index and assay limits of detection is differences in flow rate between membranes. However, while the flow rate of each membrane varied from 80 s/4 cm (GE FF80) to 170 s/4 cm (GE Immunopore FP), there was no statistically-significant correlation between membrane flow rate and assay limits of detection ($p>0.05$, Spearman's rank correlation). While it is conceivable that differences in membrane surface chemistry could have confounded the observed trends, it is more likely that the observed trends in limits of detection are attributable to paper autofluorescence. Indeed, limits of detection were higher in Millipore HF135 than in Millipore HF120 even though the flow rate of the former is slower than in the latter (and both are manufactured similarly).

The results reported here extend prior work by the Klapperich group and others highlighting the role of materials selection on assay performance and complements work quantifying plastic autofluorescence for use in microfluidic devices.[72,73,78] We believe the autofluorescence index is useful, especially considering the counterintuitive image shown in **Figure 3.5**, in which a paper (GE FF80) with an apparently lower autofluorescence as measured by spectroscopy had higher autofluorescence upon imaging with a gel imager. Therefore, we propose that developers of new assays first use the autofluorescence index to screen candidate paper substrates and identify low autofluorescence candidates at specific combinations of excitation and emission wavelengths. In contrast, developers with extant assays may use the excitation-emission matrices in **Figure 3.2** and **Figure 3.4** to identify excitation and emission wavelength combinations that minimize paper

autofluorescence, thereby potentially enhancing assay performance for a given paper and fluorophore pair while minimizing the need for assay re-engineering. The time-resolved spectra may be used by assay developers who use long-lifetime phosphorescent labels to improve assay sensitivity even further. For example, assay developers could label an assay with long-lifetime fluorophores or phosphors, and use time-gating to improve analytical performance by introducing a delay greater than 5 ns.

Sections 3.4.2 and **3.6** of this specific aim provide details on how the proposed autofluorescence screening process may be implemented. One example is the identification of a suitable paper substrate in which to perform isothermal strand displacement amplification for the point-of-care, whereby we sought to extend our recently demonstrated sample-to-result nucleic acid amplification platform to include sensitive fluorescence detection using conventional low Stokes' shift fluorophores.[79] For this application, we required a relatively thick paper substrate that had a high volumetric fluid capacity, so we narrowed our consideration to the six materials listed in **Table 3.1** that met this criterion (Ahlstrom 8950, Ahlstrom 8964, GE Standard 17, GE Fusion 5, GE Whatman 1, and Millipore C083). Details of the screening process are found in section 3.6. Briefly: we identified AquaPhluor-593 (a Texas Red analog) as a suitable fluorophore because its peak excitation and emission wavelengths (593 and 615 nm, respectively) are in the window of low autofluorescence for these papers based on the EEMs in **Figure 3.4**, its fluorescence emission is relatively uniform across a range of pH and temperatures, and it is amenable to point-of-care detection with a mobile phone. As a first step to select substrates based on autofluorescence, we performed isothermal nucleic acid amplification in-tube (six total reactions were seeded with either 0 or 10^4 copies of methicillin resistant *S. aureus* genomic DNA, labeled with AquaPhluor-593 Pleiades probes, and incubated at 49 °C for an hour) and pipetted 10 μL of each reaction onto each of the six papers (n=3). These pads were imaged with a mobile phone and the gamma-corrected intensities of each spot were quantified for the red color channel. Only 1/3 of the spots with 10^4 input copies on Millipore C083 was truly positive, while 3/3 spots with such input copies were positive on all other papers. Moreover, Millipore C083 had both the highest autofluorescence index and highest background signal (as indicated by the highest intensity of the negative spots ($p<0.01$, Welch's *t*-test)). Therefore, we eliminated Millipore C083 from consideration for further testing for this assay.

Overall, this experimental procedure took less than 2 hours, which compares favorably to the several weeks it would have taken to perform and optimize the nucleic acid amplification procedure in each paper separately (since the relative concentration of all reagents would need to be optimized independently in each material, each marginal candidate substrate requires several such 2-hour experiments to determine suitability). We strongly believe that the proposed paper substrate screening process may similarly benefit other bioassay developers and rationally identify low-autofluorescence candidate materials. To facilitate such use of the insights gleaned from this specific aim, we have made all time-resolved fluorescence spectroscopy and excitation-emission spectroscopy data freely available in the figshare data repository. We hope that access to these data will enable developers of luminescence-labeled assays to select appropriate porous substrates quantitatively and rationally, thereby enabling development of more sensitive assays.

3.6 Application of the autofluorescence index to a paper-based nucleic acid amplification assay labeled with a low Stokes' shift fluorophore

This section describes how the screening strategy based on the autofluorescence index was applied to screen membranes on which nucleic acid amplification was performed.

3.6.1 Motivation

Many diagnostic assays rely on detecting pathogenic nucleic acids, including those for HIV and methicillin-resistant *Staphylococcus aureus* (MRSA).[3,79] Isothermal nucleic acid amplification methods are a suitable alternative to polymerase chain reaction for the point of care due to their less stringent thermal and engineering constraints. Implementing such assays on paper substrates provides additional advantages by minimizing the thermal mass of the system. Several such sample-to-result assays intended for the point of care have been demonstrated recently in the literature.[79,80] The assay development process for point-of-care systems typically consists of selecting a suitable nucleic acid amplification biochemistry (*e.g.* loop-mediated amplification or strand-displacement amplification), identifying a suitable paper substrate (based on compatibility with the assay biochemistry and detection scheme),[4,72] developing the necessary support hardware (including heaters, valves, and sample preparation), and optimizing the assay biochemistry to maximize performance; these steps typically last several months or years.

One critical component of assay development and optimization is choosing the paper substrate used to support a particular assay. Beyond compatibility with the nucleic acid amplification scheme, the substrate should also enable visualization of the assay output, typically with the use of an optical label. Specific aims 3-5 (chapters 5-7) explores my work toward converting our lab's extant sample-to-result nucleic acid detection platform from colorimetric readout[79] to fluorescence readout, which ought to substantially lower the time to result. This section discusses how the autofluorescence index was applied to screen paper membranes.

3.6.2 Methods

Six membranes that have favorable fluidic (large volumetric capacity) and/or chemical compatibility with isothermal strand displacement amplification (iSDA) were identified (Ahlstrom 8950, Ahlstrom 8964, GE Standard 17, GE Fusion 5, GE Whatman 1, and Millipore C083). Nitrocellulose membranes were not considered as they were determined previously to be poor substrates for iSDA.[81] Membranes were cut to 2 cm diameter circles using a mechanical punch and placed in individual wells of a 12-well plate. Rather than optimize the nucleic acid amplification assay biochemistry on each membrane (which could take several weeks per membrane due to the need to titrate each reagent), we first used the autofluorescence index to rapidly screen membranes based on the ability to visualize the fluorescence output of a successful iSDA run.

AquaPhluor-593 (a Texas Red analog) was used as part of a Pleiades probe (with a minor groove binder) to label the output of iSDA. Its peak excitation (593 nm) and emission (615 nm) wavelengths correspond to a window of low autofluorescence for the identified papers based on **Figure 3.7**. Moreover, AquaPhluor-593 (AP-593) has a relatively constant fluorescence emission across a wide range of pH and temperatures (unlike Texas Red or AlexaFluor 594) and is suitable for detection with a point-of-care instrument such as a mobile phone (as are Texas Red and AlexaFluor 594). Reaction mixes were prepared by mixing K_iPO_4 (500 mM, 60 μL), $MgSO_4$ (100 mM, 22.5 μL),

dNTPs (10 mM, 12 µL), trehalose (37%, 1M, 162 µL), 500 kD dextran (72 µL), *ldh1* primers (500 nM forward, 250 nM reverse, 50 nM each bumper, 30 µL, ELITechGroup; sequences previously reported),[79] *ldh1* fluorescent probe (4 µM, 30 µL; 5'–AP-593–CTA ATT CAT CAA CAA TGC–minor groove binder nonfluorescent quencher–3', ELITechGroup), nuclease-free water (127.2 µL), WarmStart Bst polymerase (8000 U/µL, 15 µL, New England Biolabs), and Nt.BbvC1 nicking enzyme (0.2 U/µL, 9.6 µL, mutant strain, New England Biolabs). Reaction tubes were prepared by adding either MRSA genomic DNA (10^4 copies/µL, 6 µL, ATCC) or nuclease-free water (6 µL) and 54 µL of reaction mix. Three positive and three negative reaction tubes were prepared. iSDA was performed by incubating each tube at 49 °C for 60 minutes. The output of each reaction tube (10 µL) was pipetted onto each membrane and imaged while each membrane was still wet. The detector used was a mobile phone (LG Nexus 5X) with a Texas red excitation and emission filter (Semrock) on the cell phone flash and camera, respectively. Images were acquired at ¼ second exposure and ISO 6400; spot intensities were quantified in ImageJ. Gamma-corrected mean spot intensities of the red channel were compared between membranes; for each membrane type, spots were considered positive if they were greater than the mean plus 2.92 times the standard deviation of the negative control spots (threshold based on *t*-statistics for α=5% and 2 degrees of freedom).

3.6.3 Results and discussion

Figure 3.8 below shows representative photos of iSDA endpoint fluorescence on paper. On each membrane, three (of three) distinct spots are visually observable for those corresponding to MRSA gDNA-positive reaction tubes, whereas zero spots (of three) are visually observable for those corresponding to MRSA-negative tubes. Images were acquired at the highest exposure and sensitivity (¼ second and ISO 6400, respectively) possible for the Nexus 5X to maximize photon capture.

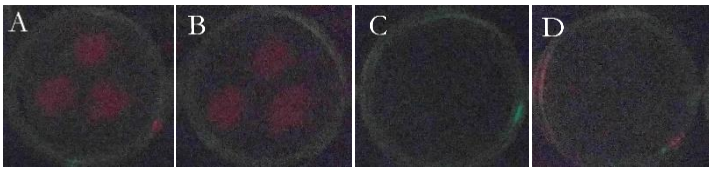

Figure 3.8: Representative photos of iSDA endpoint fluorescence. iSDA was performed in-tube and the output was spotted onto porous membranes: (**a**) Ahlstrom 8950 (MRSA gDNA-positive); (**b**) Ahlstrom 8964 (MRSA gDNA-positive); (**c**) Ahlstrom 8950 (MRSA gDNA-negative); and (**d**) Ahlstrom 8964 (MRSA gDNA-negative). Three spots are visible on each membrane corresponding to tubes that were MRSA gDNA-positive (a and b), whereas no spots are visible for spots corresponding to tubes that were MRSA gDNA-negative (c and d).

Table 3.3 indicates the mean and standard deviation of spots corresponding to MRSA gDNA-positive and MRSA gDNA-negative tubes, along with the statistical thresholds for a positive result and fraction of spots greater than this criterion. All spots corresponding to MRSA gDNA-positive tubes were above the threshold for positive spots except on Millipore C083, the membrane with the highest autofluorescence index, for which only one of three spots was above the threshold. Indeed, Millipore C083 had the greatest autofluorescence index, spot intensities, and threshold for positive of all materials evaluated.

Table 3.3: Autofluorescence index and iSDA spot intensities on several paper substrates

	Autofluorescence index	Negative spot intensity†	Positive spot intensity†	Threshold for positive†	Fraction above threshold
Ahlstrom 8950	1500	5.5 ± 0.69	21 ± 2.9	8	3/3
Ahlstrom 8964	1720	7.7 ± 0.19	39 ± 1.3	8	3/3
GE Standard 17	1090	11 ± 2	20 ± 2.3	16	3/3
GE Fusion 5	924	9 ± 0.88	18 ± 1	12	3/3
GE Whatman 1	1610	12 ± 1.6	19 ± 1.8	16	3/3
Millipore C083	2850	47 ± 9	74 ± 5.6	73	1/3

†: Mean and standard deviation of the gamma-corrected red color channel intensities are tabulated.

The threshold for positive was much greater on Millipore C083 than on the other membranes because of the greater intensity of the negative spot and slightly greater coefficient of variation. Indeed, the negative spot intensity was greater on Millipore C083 than on each of the other materials ($p<0.01$, Welch's *t*-test). Based on these data, we eliminated Millipore C083 from consideration as a substrate to support iSDA in paper. Rather, we have been exploring GE Fusion 5, GE Standard 17, and Ahlstrom 8950 due to their low autofluorescence (as indicated by both low negative spot intensities and low autofluorescence indices) and favorable fluidic and chemical compatibility with iSDA.

Use of the autofluorescence index in substrate screening is advantageous because it enables rationally (rather than arbitrarily) identifying potential paper membranes. The autofluorescence index reduces the need to optimize an assay on several potential paper substrates, which is time-consuming and costly (requiring weeks or months of experiments in our experience as all 12 assay reagents must be titrated independently). This is because the autofluorescence index provides a metric that corresponds to the expected signal observed in an assay based on the spectral overlap between a fluorophore's spectral emission and that of paper autofluorescence, while also accounting for the detector's spectral sensitivity. In our case, use of the autofluorescence index to screen membranes eliminated Millipore C083 from consideration (thereby eliminating the need to validate iSDA on Millipore C083).

3.7 Conclusions

This aim details a systematic investigation of autofluorescence in porous media and a rational screening strategy to overcome it. It is the first systematic characterization of autofluorescence in different types of porous media commonly used in paper microfluidics, including nitrocellulose, cellulose, glass fiber, and other membranes. The details on autofluorescence lifetimes and wavelengths are invaluable to the development of any luminescence-based assay performed in porous media. Second, the screening strategy described in this aim is the first quantitative framework that enables assay developers to rationally identify substrates for fluorescence assays. The screening strategy enables developers to screen materials based on easily measurable autofluorescence properties that correlate with assay performance; its application toward both a lateral flow immunoassay and a nucleic acid test demonstrate its potential utility to reduce the time needed to develop assays, such as the assays described in the following chapters of this work.

4 Mobile phone ratiometric imaging enables highly sensitive fluorescence lateral flow immunoassays without external optical filters

"Every experience of beauty points to infinity."

– Han Urs von Balthasar, as recorded by Noel O'Donaghue reflecting on the philosophy of Plato, from *The Analogy of Beauty*, p. 7, edited by John Riches, 1986.

4.1 Summary

4.1.1 Abstract

Paper-based diagnostic tests based on the lateral flow immunoassay concept promise low-cost, point-of-care detection of infectious diseases, but such assays suffer from poor limits of detection. One factor that contributes to poor analytical performance is a reliance on low contrast chromophoric optical labels such as gold nanoparticles. Previous attempts to improve the sensitivity of paper-based diagnostics include replacing chromophoric labels with enzymes, fluorophores, or phosphors at the expense of increased fluidic complexity or the need for device readers with costly optoelectronics. Several groups, including our own, have proposed mobile phones as suitable point-of-care readers due to their low cost, ease of use, and ubiquity. However, extant mobile phone fluorescence readers require costly optical filters and were typically validated with only one camera sensor module, which is inappropriate for potential point-of-care use. In response, we propose to couple low-cost ultraviolet light-emitting diodes with long Stokes-shift quantum dots to enable ratiometric mobile phone fluorescence measurements without optical filters. Ratiometric imaging with unmodified smartphone cameras improves the contrast and attenuates the impact of excitation intensity variability by 15x. Practical application was shown with a lateral flow immunoassay for influenza A with nucleoproteins spiked into simulated nasal matrix. Limits of detection of 1.5 and 2.6 fmol were attained on two mobile phones, which are comparable to a gel imager (1.9 fmol), 10x better than imaging gold nanoparticles on a scanner (18 fmol), and >2 orders of magnitude better than gold nanoparticle-labeled assays imaged with mobile phones. Use of the proposed filter-free mobile phone imaging scheme is a first step toward enabling a new generation of highly sensitive, point-of-care fluorescence assays.

4.1.2 Contributions to the academic literature

Parts of this aim contributed to the academic literature as part of conference posters, a US patent application, and a journal article (from which substantial portions of this chapter are reproduced):

- Shah K, Abe K, Kauffman P, and Yager P. Filter-free fluorescence measurements at the point of care: A simple device to improve the limit of detection of lateral flow assays. MicroTAS Conference, Poster, 2016. Dublin, Ireland.
- Shah K, Kauffman P, and Yager P. Fluorescence improves the sensitivity of paper microfluidics: 1) Account for paper autofluorescence and 2) Image with a mobile phone. Gordon Research Conference, Poster, 2017. Tuscany, Italy.

- Shah K, Kauffman P, and Yager P. Fluorescence improves the sensitivity of paper microfluidics: 1) Account for paper autofluorescence and 2) Image with a mobile phone. Gordon Research Seminar Poster, 2017. Tuscany, Italy.
- Shah K, Abe K, and Kauffman P. Filter-free devices and systems for measuring fluorescence of a microfluidic assay and associated methods of use. US Patent Application. US20170323441A1. Assigned to University of Washington.

4.2 Introduction

Paper-based assays are suitable for the point-of-care detection of infectious disease due to their low cost, ease of use, and suitability for multiplexing. Many paper-based assays use gold nanoparticle labels to indicate the presence of analyte, but these tests suffer from poor limits of detection due to the low signal-to-noise ratios inherent to labeling with one absorbance-based optical label per analyte molecule. Chromogenic enzymatic labels or fluorescent labels have been proposed to enhance signal-to-noise ratios, but at the expense of increased device complexity.[29,82] Fluorescent labeling is especially promising due to its potential to enable single-molecule detection when lab-based microfluidic assays are imaged with standard cameras.[83]

Several recent studies have shown that camera-based sensors and mobile phones sensitively read the output of assays intended for the point of care. The Whitesides group demonstrated that low-cost mobile phones are suitable for chromophoric, paper-based assays in low resource settings.[23] Several other groups have shown that mobile phones (including smartphones) may image chromophore and fluorophore-labeled (including paper-based) assays.[29,83,84] Such smartphone-imaged assays have even been integrated into fully automated diagnostics platforms, such as those developed by our lab for the sample-to-result detection of methicillin-resistant *Staphylococcus aureus* nucleic acids or influenza A/B nucleoproteins at the point of care.[42,79] However, one drawback of extant mobile phone-based imaging systems is that assays were typically validated with just one mobile phone camera sensor, even for studies involving multiple mobile phone models.[83] Given the fragmentation of the commercial mobile phone market, there is a need to develop device-independent imaging methods that are compatible with a wide range of camera sensors.

Such device-independent imaging capabilities are especially relevant to fluorophore-labeled assays. Typically, fluorescence measurements enhance the sensitivity of bioassays by enabling wavelength-based discrimination of a signal of interest generated by a fluorescent labeling molecule against noise spread over a wide spectral range. Wavelength discrimination is accomplished by using one or more optical filters on the excitation source and photodetector. However, wavelength-selective optical filters are costly, subject to photodegradation, and (in the case of interference filters) vary in wavelength discrimination based on the angle of incident photons. An additional drawback of camera-mounted external attachments is the need to optimize such attachments for specific mobile phone models, which limits their generalizability beyond the particular mobile phones for which such attachments were engineered. Moreover, the spectral sensitivity of detectors varies between both camera sensor modules and mobile phone device models.[85] In addition, the fluorescence intensity measured by a detector is dependent not only on the concentration of fluorescent labels,

but also on the excitation light intensity (which often requires the addition of a fluorescence intensity standard). These limitations typically impose tight constraints on fluorescence measurements by requiring specific excitation sources, optical filters, and detectors with narrow spectral tolerances and controlled positioning of optical components, all of which increase the cost and complexity of fluorescent detection.

In response, we developed a ratiometric imaging approach that is suitable for fluorophore-labeled, mobile phone-imaged assays without requiring external optical filters or any attachment onto the mobile phone camera. The system excites large Stokes shift quantum dots with low-cost, USB (universal serial bus)-powered ultraviolet (UV) light-emitting diodes (LED) and images with unmodified mobile phone cameras. The versatility of this approach was validated with two mobile phone cameras with significantly different spectral sensitivities and was demonstrated with a clinically relevant influenza A nucleoprotein assay developed previously in our lab.

4.3 Methods

4.3.1 Quantifying spectral sensitivities

A pulsed Hg-Xe arc lamp was used to generate broad-spectrum light between 300 and 800 nm and a monochromator was swept in 10 nm increments (Perkin-Elmer LS-50B). The arc lamp was imaged with a LG Nexus 5X and Apple iPhone SE at fixed exposure settings (0.25 second exposure, ISO 400 using the Camera FV-5 or ProCamera apps). The intensity of the arc lamp was quantified using ImageJ for the red, green, and blue color channels of minimally compressed images outputted by each smartphone and corrected for the arc lamp emission spectrum. The spectral emission of six commercial UV LEDs with nominal 365 nm emission peaks was measured (Ocean Optics USB4000 spectrometer) when powered by a 200 mA current source. The fluorescence excitation (605 nm emission wavelength, 2.5 nm slits) and emission spectra (365 nm excitation wavelength, 2.5 nm slits) of streptavidin-labeled quantum dots (ThermoFisher Qdot 605-streptavidin) were measured on a fluorimeter (Perkin-Elmer LS-50b). The quantum dot conjugates are ~15-20 nm in diameter and consist of CdSe-ZnS core-shell quantum dots with a polymer coating. The manufacturer-reported quantum yield for the particular lot is 83% when excited at 300 nm; the expected quantum yield is less than 40% at the 365 nm excitation wavelength used herein.

4.3.2 Design of UV excitation module

A low-cost USB-powered UV LED excitation module was constructed with a laser-cut, minimally-fluorescent device housing made of layered polymethylmethacrylate. A custom constant-current LED driver was designed to output constant current despite fluctuations in input voltage based on steady-state circuit simulations using SPICE (input voltage between 4.5 and 5.5 volts, which can be provided by a mobile phone or standard USB connection). The module (**Figure 4.1a**) consists of a double pole, single throw button that powers the UV LED and activates the cell phone camera shutter (**Figure 4.1b**), which was inspired by the design of selfie sticks. The UV LED can be positioned anywhere along the back of the smartphone using double-sided tape, such as near the built-in camera flash. (**Figure 4.1c**).

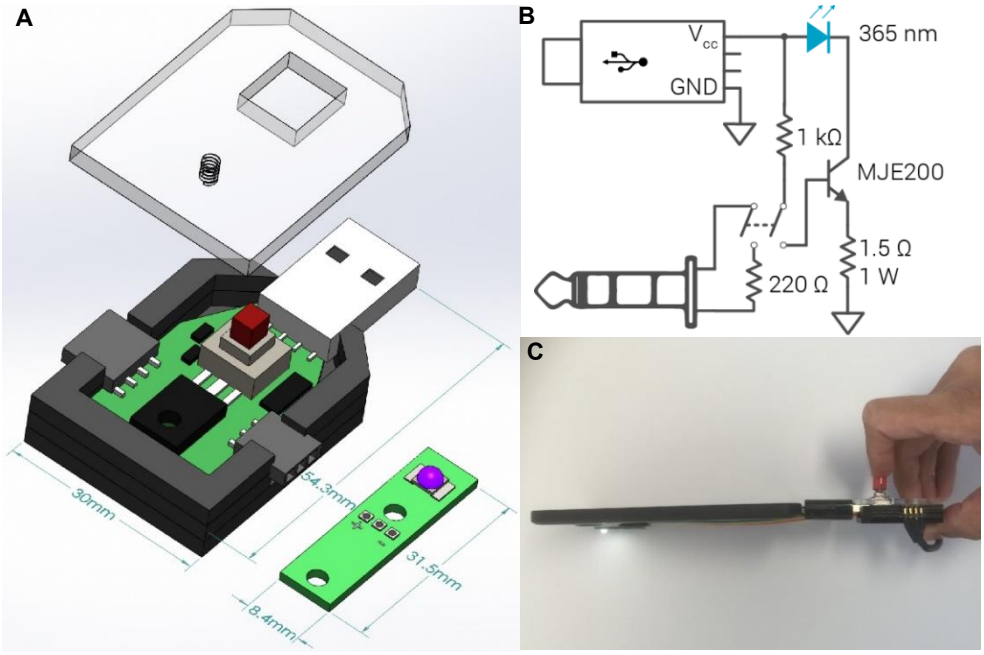

Figure 4.1: Design of USB-powered UV LED module. (**a**) Exploded view shows the USB type A LED driver and repositionable UV LED board (wires hidden for clarity). (**b**) Schematic and circuit diagram of the LED driver. (**c**) Photo of the LED module being powered by a Nexus 5X with a USB type A to type C adapter. Pressing the button activates both the UV LED and triggers the Android camera shutter via the 3.5 mm headphone connector. The printed circuit board was laid out by Peter Kauffman.

4.3.3 Validation of ratiometric method to image quantum dots on nitrocellulose

A 10-fold serial dilution of the streptavidinylated quantum dots was prepared (10 nM to 10 pM and 0 M) in 10 mM, pH 7.4 phosphate-buffered saline. The quantum dots were pipetted (2 µL) onto a sheet of Millipore HF120 nitrocellulose (spots were 0.5 cm from each other) and imaged when dry (n=6, alternate rows were reversed to reduce confounding lighting biases). The quantum dots were excited with the UV LED module, which was placed 14 cm above the nitrocellulose. Exposure-corrected photos were taken with the Nexus 5X and iPhone SE at ISO-400; the phones were placed 11 cm above the nitrocellulose. The excitation intensity was varied by placing a UV-visible neutral density filter (OD 0.3, 1.3, 2.5, and 3.0 (Edmund Optics)) in front of the UV LED module (the current was kept constant to minimize variation in the LED spectrum). Actual excitation intensities near the test line were measured with a UV-sensitive photodiode (Thorlabs FGAP71) connected to a picoammeter (Keithley 414A); radiant flux estimates were made by dividing the measured current with the definite integral of the convolved spectra of the photodiode and UV LED. The red, green, and blue color channel intensities of each spot were quantified in ImageJ. These intensities were gamma-corrected from the 8-bit sRGB colorspace to normalized linear RGB coordinates from 0 to 1. A ratiometric quantity was developed based on the linear RGB coordinates as shown in **Equation 4.1** (the denominator adds unity to prevent division by zero):

Equation 4.1:

$$\boldsymbol{Ratio = \frac{Linear\ red\ channel}{Linear\ blue\ channel + 1}}$$

Statistical analysis was performed with parametric methods to compare whether the fluorescence emission increased linearly with excitation intensity (*F*-test) and whether there was a difference in slopes between the ratiometric method and considering the red channel only (Welch's *t*-test).

4.3.4 Validation with influenza A nucleoprotein assay

We validated our fluorescence imaging system with an influenza A nucleoprotein lateral flow assay previously developed in our lab (assay stack visualized in **Figure 3.6**).[42,86] Briefly, the assay consists of Millipore HF120 4 mil-thick (0.1 mm) Mylar-backed nitrocellulose striped (Biodot Biojet HR Solenoid Dispenser) with anti-influenza A monoclonal antibodies (Hytest InA108, 1 mg/mL) in the capture region and anti-mouse IgG in the control region (Jackson ImmunoResearch Affinipure Goat Anti-Mouse IgG, 1 mg/mL). The cellulose wicking pad (Millipore C083) overlapped the nitrocellulose over 1 cm and was held in place with adhesive-backed Mylar (Fralock). Striped cards were dried at 37 °C for two hours, cut to 5-mm strips, and stored with desiccant in airtight, lightproof bags.

Usage of the lateral flow strips consisted of sequentially placing the strips into four wells of a 96-well plate until the fluid was drawn (about 3-10 minutes per well, total time less than 30 minutes). The first well contained 20 μL of recombinant influenza nucleoprotein with histidine tag (Brisbane/10/2007 (H3N2), International Reagent Resource, Influenza Division, WHO Collaborating Center for Surveillance, Epidemiology and Control of Influenza, Centers for Disease Control and Prevention, Atlanta, GA, USA, lot 59245888) diluted in simulated nasal matrix (specified below), which was pre-mixed with 20 μL of biotinylated detecting antibody (HyTest 3IN5 InA245) at 0.01 mg/mL diluted in assay running buffer (specified below) with 5% Triton X-100. The simulated nasal matrix followed the recipe described in Panpradist et al., which consisted of 1 part nasal matrix: 110 mM NaCl, 1% w/v mucin from porcine stomach type III (Sigma-Aldrich M1778), and 10 μg/mL human genomic DNA (Promega G041) diluted in 9 parts assay running buffer with 5% Triton X-100).[87] The assay running buffer consisted of 10 mM phosphate-buffered saline (pH=7.4), 1% (w/v) bovine serum albumin, and 0.05% Tween-20. The second well contained 20 μL of assay running buffer. The third well had 20 μL of optical label diluted in assay running buffer with 5% Triton X-100 (50 nM streptavidin-labeled quantum dots or OD0.3 streptavidin-40 nm diameter gold conjugates (Innova Biosciences)). The fourth well contained 40 μL of assay running buffer with 5% Triton X-100 as a final wash step. The lateral flow strips were dried at room temperature (about 20 minutes) to minimize the effect of variations in refractive index due to differences in wetness. The strips were imaged with the mobile phones and a laboratory instrument (gel imager (Bio- Rad Gel Doc EZ Imager with UV tray) for Qdot-605 or scanner (Epson Perfection V700) for gold nanoparticles). The mean intensity in all color channels was quantified in ImageJ for each capture region. Four-parameter logistic curves were fitted to the data in MATLAB following the method outlined by Holstein et al.[16,86] Statistical analysis was performed using parametric techniques (2-sample *t*-tests with equal variance) to determine whether Qdot-605 labeling improved limits of detection compared to gold nanoparticles (95% confidence intervals reported when calculable). Figures were prepared in MATLAB 2017b or Python *via* the Anaconda distribution (Spyder 3.2).

4.4 Results

4.4.1 Screening LEDs and quantum dots

The actual peak emission wavelengths of six ultraviolet LEDs were 7-11 nm greater than the 365 nm nominal rated peak emission. A substantial portion of the emission of all LEDs was at ultraviolet wavelengths as quantified by the area under the emission curve ratio (AUCR) below 400 nm to the area above 400 nm (**Figure 4.2**). The LED with the greatest AUCR per unit price (Everlight EAUVA35352BC6) was used as the excitation source for the USB-powered LED module.

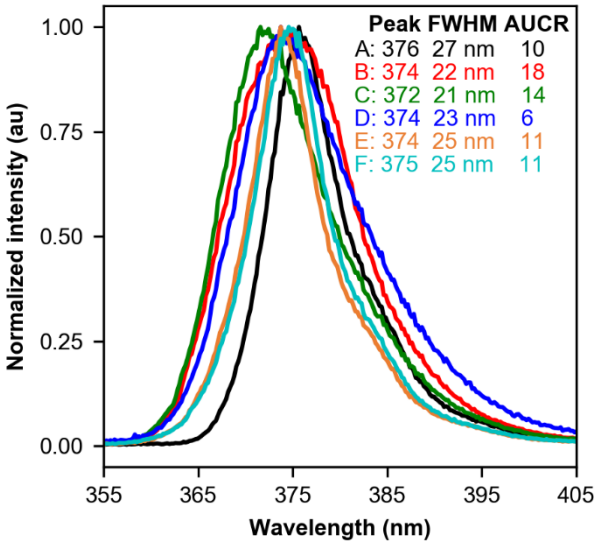

Figure 4.2: Emission spectra of ultraviolet light-emitting diodes with nominal 365 nm peak emission wavelengths. Actual peak emission wavelengths, full width at half-maximum (FWHM), and areas-under-the-curve ratio (AUCR) at ultraviolet (<400 nm) to visible wavelengths (400-700 nm) are indicated in the upper-right for each diode: (**a**) Lite-On LTPL-C034UVH365; (**b**) Luminus Devices SST-10-UV-A130-E365-00; (**c**) LED Engin LZ1-10UV-00-0000; (**d**) LED Engin LZ1-30UV00-0000; (**e**) Vishay VLMU3510-365-130; (**f**) Everlight EAUVA35352BC6. Diode F was selected based on maximizing AUCR per unit price. Details of acquisition (by Vidhi Singh) are found in the methods section.

Seven quantum dots with peak emissions between 525 nm and 705 nm were screened for visualization by the Nexus 5X and iPhone SE. Both phones resolved 20 fmol spots of quantum dots with peak emission between 565 and 655 nm (inclusive) when excited with the USB-powered LED module. As expected, quantum dots with peak emissions at lower wavelengths were mainly detected in the blue channel of smartphone photos, and those with peak emissions at 585 nm and greater were primarily detected in the red color channel as shown in **Figure 4.3**.

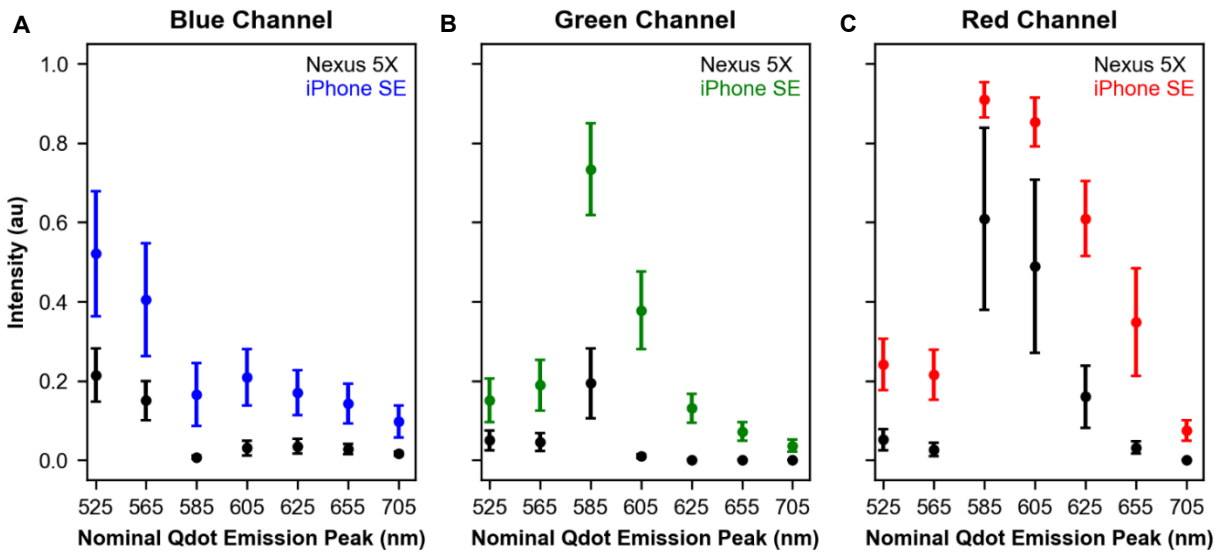

Figure 4.3: Imaging quantum dots with varying peak emission wavelengths with mobile phones. Quantum dots with visible and near-infrared peak emission wavelengths were pipetted (20 fmol) onto HF120 nitrocellulose and imaged with two mobile phones and excited with an ultraviolet light-emitting diode (n=3). Panels show the gamma-corrected intensities of the (**a**) blue channel, (**b**) green channel, and (**c**) red channel. Values indicated are averages and standard errors and are not compensated for local background intensities or excitation levels.

Quantum dots with peak emissions of 585 and 605 nm were observed to have the highest signal intensities, which occurred in the red channel. These large signals also corresponded to high signal-to-background ratios for these two quantum dots (**Figure 4.4**). Quantum dots with peak emissions of 605 nm (Qdot-605) had the largest signal-to-background ratio on both phones and were selected for further evaluation.

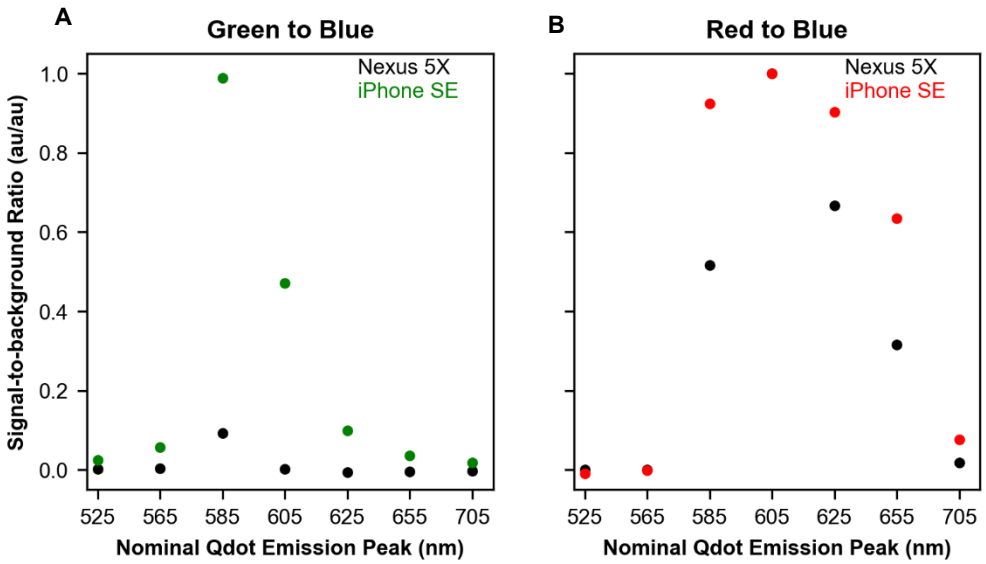

Figure 4.4: Screening quantum dots with varying peak emission wavelengths by signal-to-background ratios. The average of the normalized green-to-blue (**a**) and red-to-blue (**b**) ratios for the data in **Figure 4.3** are plotted for two mobile phones. Qdot-605 was selected as it has the largest signal-to-background ratio on both phones.

Figure 4.5a shows the emission spectrum of the Everlight UV LED overlaid with the fluorescence excitation and emission spectra of Qdot-605. The UV LED emission spectrum overlaps substantially with the excitation spectrum of the quantum dots. **Figure 4.5b** and **Figure 4.5c** show the spectral sensitivity of the rear cameras of two midrange mobile phones, the iPhone SE and the Nexus 5X. The red channels of both phones are much less photosensitive than the blue or green channels. The red channels of both phone cameras detect light with wavelengths near 400 nm in addition to light around 600 nm. Neither phone detects an appreciable level of near-ultraviolet or near-infrared light. The red channels of both phones overlap almost perfectly with the emission of Qdot-605. The red and blue channels of both phones overlap slightly with the right tail of the UV LED's spectral emission.

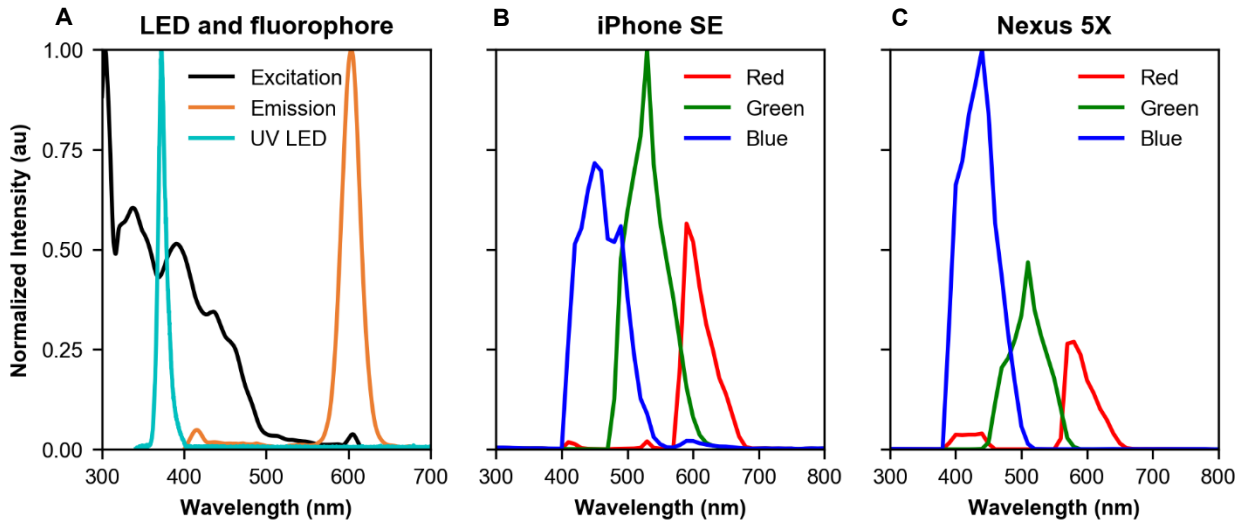

Figure 4.5: Gamma-corrected, normalized spectra of interest. (**a**) Fluorescence excitation and emission spectra of Qdot-605 and the spectrum of the ultraviolet LED. (**b**) Spectral sensitivity of the iPhone SE rear camera color channels across near-ultraviolet through near-infrared wavelengths. (**c**) Spectral sensitivity of the Nexus 5X rear camera. The red channel of both camera sensors detects blue light in addition to red. The camera spectra were quantified by imaging an arc lamp swept in 10 nm increments across near-ultraviolet to near-infrared wavelengths as detailed in the text.

4.4.2 Validation of ratiometric method

The ratiometric method was evaluated by imaging a series of quantum dots on nitrocellulose at five excitation intensities and at five Qdot-605 concentrations with both mobile phones. The radiant flux (a measure of excitation intensity) measured by a UV-sensitive photodiode was 9.9 μW, 21 μW, 300 μW, 2.7 mW, and 5.0 mW. **Figure 4.6a** and **Figure 4.6b** show how the observed fluorescence varied with excitation intensity for the Nexus 5X and iPhone SE, respectively. The average and standard error of the red channel gamma-corrected, exposure-compensated intensities varied from 0.23±0.018 arbitrary units (au) (at 20 fmol Qdot-605, 0.2% excitation intensity) to 450±26 au (at 20 fmol Qdot-605, 100% excitation intensity) on the iPhone SE. At these excitation levels, the ratiometric method intensities on the iPhone SE spanned from 0.22±0.017 au to 26±0.90 au.

In other words, as the excitation intensity increased by 2.7 orders of magnitude, the measured fluorescence by the iPhone SE red channel increased by 3.3 orders of magnitude, whereas the fluorescence intensity of the ratiometric method increased by only 2.1 orders of magnitude (similar trends were observed at all Qdot-605 concentrations tested). On the Nexus 5X, the red channel fluorescence intensity increased by 3.8 orders of magnitude across these excitation intensities,

whereas the fluorescence intensity of the ratiometric method increased by only 2.6 orders of magnitude. The increase in fluorescence intensity was significantly lower for the ratiometric method than for the red channel alone ($p<0.001$, Welch's *t*-test). The slopes of the trend lines in **Figure 4.6a** and **Figure 4.6b** quantify the extent to which measured fluorescence varies with excitation intensity. These slopes are plotted in **Figure 4.6c** and **Figure 4.6d** for both phones. The slope was significantly greater when considering the red channel only than with the ratiometric method for all amounts of Qdot-605 ($p<0.001$, Welch's *t*-test).

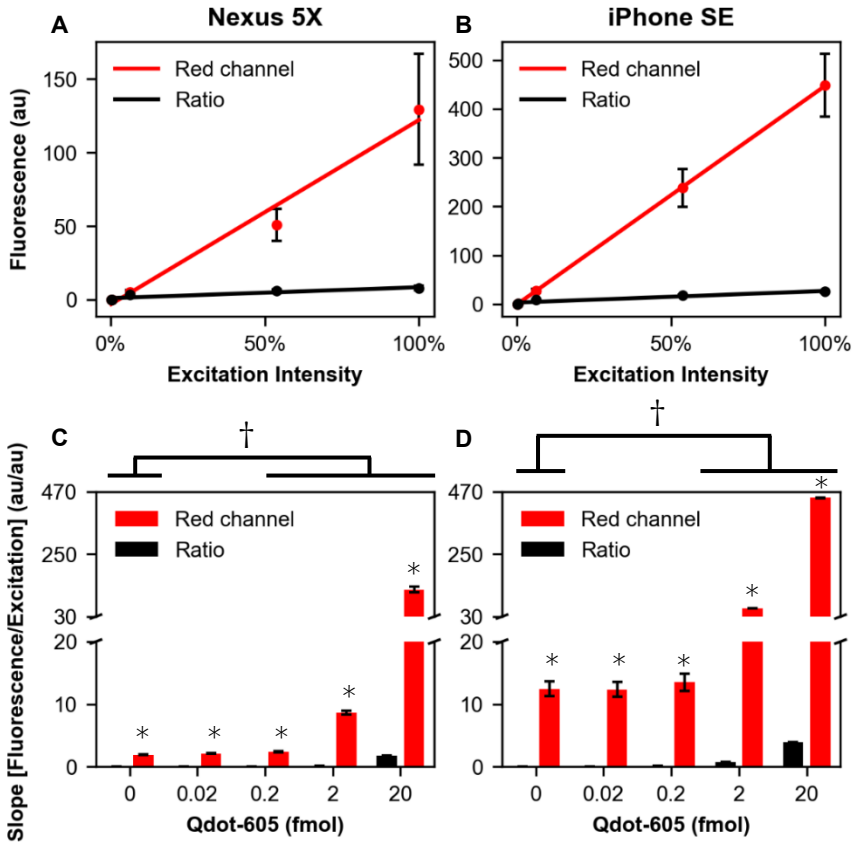

Figure 4.6: Demonstration of the ratiometric method. Validation of the hypothesis that fluorescence measured via the ratiometric method is less dependent on the excitation intensity than when considering just one color channel (*lower* slopes indicate better performance). The measured fluorescence emission of 20 fmol of Qdot-605 in the red channel increases linearly ($p<0.0001$, *F*-test) with the excitation intensity for both the (**a**) Nexus 5X and (**b**) iPhone SE (points indicate average and standard error). However, the slope of increase is significantly lower for the ratiometric method than in the red channel for both the (**c**) Nexus 5X and (**d**) iPhone SE across all fluorophore amounts ($^{*}p<0.001$, Welch's *t*-test). Error bars show the standard error of the slope estimate. The ratiometric method does not appreciably worsen limits of detection as evidenced by the differing slopes between the 0 fmol and the 2 fmol or 20 fmol conditions ($^{\dagger}p<0.05$, Welch's *t*-test).

4.4.3 Application of the ratiometric method to a clinically relevant bioassay

Practical application of the ratiometric method was realized by evaluating the ability of two mobile phones and lab instruments to image lateral flow strips to detect recombinant influenza A nucleoprotein spiked into simulated nasal matrix (this relatively complex sample was used because complex biological samples exhibit autofluorescence[88,89] and typically exacerbate quantum dot nonspecific binding[90,91]). The assay was run at optimized conditions with Qdot-605 or gold nanoparticle labels and imaged with the Nexus 5X or iPhone SE (illumination with the UV LED for

Qdot-605 and ambient light for gold nanoparticles) or laboratory instrument controls (gel imager for Qdot-605 and scanner for gold nanoparticles). Representative images of the lateral flow strips are shown in **Figure 4.7**. The Qdot-605 labeled strips had low background intensities when imaged on the gel imager but appeared distinctly blue when imaged with mobile phones; the gold-labeled strips had clearly distinguishable capture and control lines when imaged on a laboratory scanner but had faint lines when imaged with mobile phones. The Nexus 5X and iPhone SE successfully resolved as few as 1.6 fmol of analytes with Qdot-605 labels based on visual readout, whereas 8-40 fmol were needed for gold nanoparticle labels. The laboratory controls both required at least 1.6 fmol of analyte for visualization.

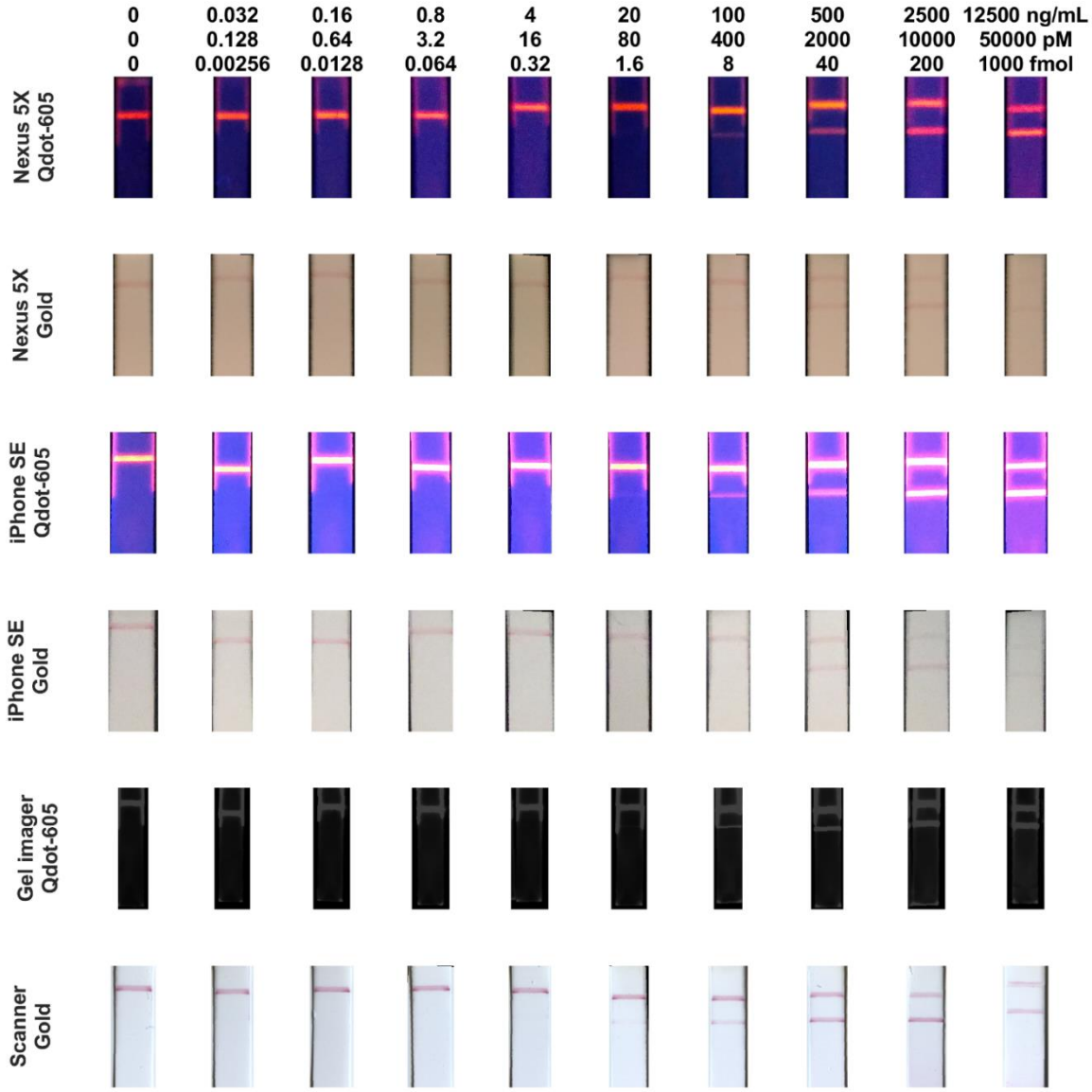

Figure 4.7: Representative images of lateral flow strips on all devices at all tested concentrations of analyte. The lower line in each lateral flow strip is the capture region (test line) indicating the presence or absence of influenza A nucleoprotein. The upper line is a flow control that indicates delivery of detection antibody and optical label to the capture region. While the quantum dot-labeled lateral flow strips had a very low background on the gel imager due to optical filtering, the lateral flow strips had a strong blue background when imaged by mobile phones, but the perceived color differed between the two mobile phone models.

Quantitative analysis of the lateral flow strip images suggests that limits of detection (as established by thresholding via *t*-statistics following Holstein et al.)[16] were 1.50 fmol on the Nexus 5X and 2.61 fmol (95% confidence interval: 2.38 to 2.85 fmol) on the iPhone SE with Qdot-605 labeling, but that the gold nanoparticle-labeled strips were not quantitative with mobile phone imaging at the analyte levels tested (**Figure 4.8**). Limits of detection on the laboratory instruments were 1.92 fmol (1.80 to 2.06 fmol) on the gel imager for Qdot-605 and 17.8 fmol on a scanner for gold nanoparticles. Limits of detection were significantly lower with the ratiometric method on the Nexus 5X ($p<0.001$, 1-sample *t*-test) or iPhone SE ($p<0.00001$, 1-sample *t*-test) with Qdot-605 labeling than with a scanner using gold nanoparticle labels. No significant difference was observed between the gel imager and the ratiometric method on either mobile phone ($p>0.01$, 2-sample *t*-test with equal variance).

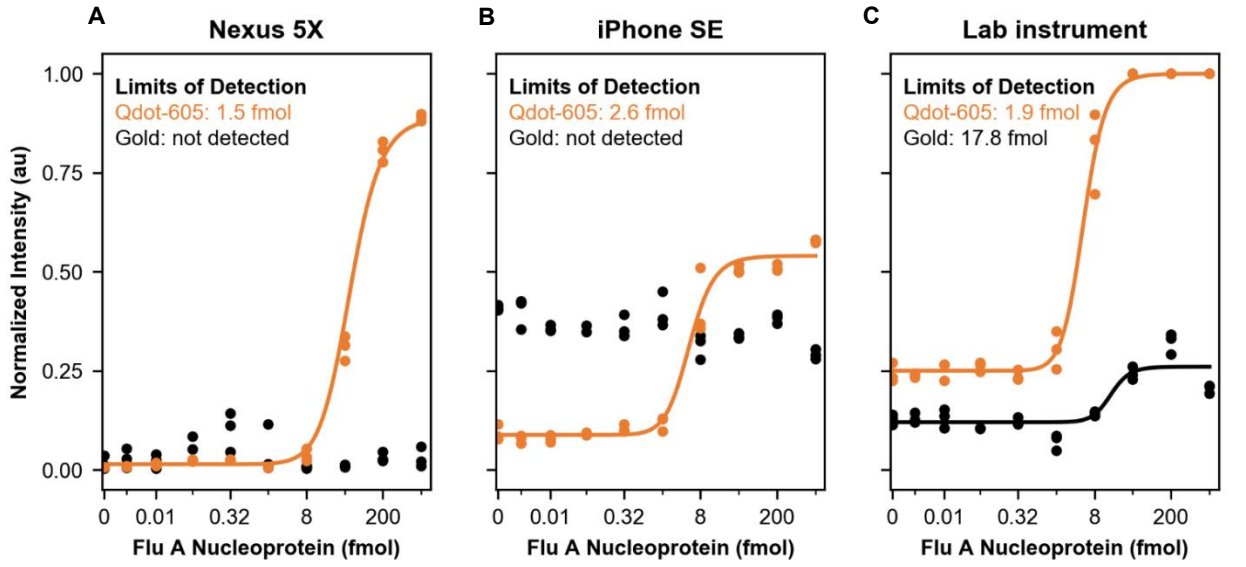

Figure 4.8: Standard curves of recombinant influenza nucleoprotein spiked into simulated nasal matrix (n=3) as imaged by the (**a**) Nexus 5X, (**b**) iPhone SE, or (**c**) laboratory controls. The mobile phones quantitatively measured influenza nucleoprotein when labeled with Qdot-605 and imaged via the ratiometric method, but not with gold nanoparticles (normalized green channel intensity is plotted). Ratiometric mobile phone fluorescence imaging without optical filters was comparable to a laboratory fluorescence reader and improved limits of detection by 10x compared to gold nanoparticle-labeled strips imaged on a laboratory scanner. Each point indicates the mean intensity of a particular lateral flow strip's capture region, and curves indicate 4-parameter logistic regressions.

4.5 Discussion

Paper-based diagnostic tests such as lateral flow assays provide a simple, low-cost platform to detect analytes such as infectious disease biomarkers, but these assays suffer from poor sensitivity due to the use of absorbance-based optical labels. The use of fluorescent labeling has been shown to improve these assays,[4,44,56,92] but translation to the point of care is impeded by the considerable expense of specialized fluorescence readers, which often use custom excitation sources, optical filters, and detectors. Mobile phones are especially suited to replace dedicated fluorescence readers due to their ubiquity, ease of use, and integrated optics and communications hardware.[4]

However, several factors currently hinder the practical realization of point-of-care mobile phone imaging of fluorescence assays in paper: 1) the paper substrate (*e.g.* nitrocellulose) on which the assay is performed emits autofluorescence and is highly scattering, which reduces signal-to-

background ratios;[86] 2) on-camera image preprocessing impedes quantitative measurements; 3) spectral sensitivities of mobile phone camera color channels (*i.e.* red, green and blue pixel sensitivities) differ significantly between models;[85] 4) measured fluorescence intensity correlates not just with the number of fluorophores present but also the excitation intensity;[4] and 5) external optical filters are still needed to distinguish fluorescence emission from excitation light. We propose to address these limitations with ratiometric mobile phone imaging of long Stokes shift quantum dots to improve sensitivity while significantly reducing the cost of fluorescence measurements. Since images acquired with mobile phones do not have a one-to-one correlation between standardization of outputted images into the highly nonlinear sRGB colorspace, we follow the standard approach to linearize image intensities by correcting for the gamma and converting to linear RGB coordinates. Ratiometric analysis of the linear RGB coordinates reduces the impact of the five limitations previously expounded.

Ratiometric analysis requires identifying two color channels such that one color channel primarily contains the signal of interest and the second primarily contains the background noise. In our case, the signal of interest (Qdot-605 fluorescence emission) is primarily detected in the red color channel (along with some paper autofluorescence). However, fluorescence intensity (*e.g.* in the red channel) is also proportional to the excitation intensity as illustrated by **Figure 4.6a** and **Figure 4.6b**. The blue color channel primarily detects the background noise: 1) the UV LED emission; 2) paper autofluorescence; and 3) some of the quantum dot signal in the case of phones such as the Nexus 5X that follow the CIE 1931 color space. All three of these signals detected in the blue color channel are proportional to the excitation intensity. Therefore, the ratio of the linearized red and blue color channels ought to reduce the effect of variations of excitation intensity on the measured fluorescence signal, which concords with the observed 15× reduction (1.2 orders of magnitude).

While many mobile phones are unable to natively visualize ultraviolet light (including the two phones in **Figure 4.5**), the emission of LEDs undergoes a slight bathochromic shift toward longer wavelengths as the LEDs heat up during use (shown in **Figure 4.2**), which increases the overlap of UV LED emission spectra with the blue channel of mobile phone cameras. In previous work, we showed that nitrocellulose primarily emits autofluorescence at blue and green wavelengths below about 550 nm, which would also be detected by the mobile phone camera blue and green color channels.[86] Therefore, one would expect that quantum dots that emit primarily at longer wavelengths and are detectable by the camera's red color channel would have higher signal-to-background ratios than those that emit at shorter wavelengths. **Figure 4.4** affirms this *a priori* hypothesis, which shows that quantum dots with a peak 605 nm emission have higher signal-to-background ratios than those with other peak emission wavelengths (quantum dots with greater peak emission wavelengths overlap less with the peak spectral sensitivity of the mobile phone cameras' red channel).

This aim describes a significant step toward more sensitive immunoassays at the point of care without a significant increase in device complexity or cost. Almost all previous attempts to improve point-of-care assay performance by 10x have come at a significant increase in device complexity[29,42] or cost[32,38,56,92–94] as shown in **Table 4.1**. For example, previous attempts to image UV-excited quantum dots with smartphones relied on optical filters and/or FRET to enhance performance.[56,95] While ratiometric imaging was applied previously to fluorescence, FRET-based lateral flow assays by the Krull group,[56] and is a useful approach in fluorescence microscopy (*e.g.* for measuring intracellular calcium concentration), we are unaware of such an approach being used to completely eliminate the need for external optical filters for single-fluorophore labeling while simultaneously improving bioassay limits of detections.

Table 4.1: Comparison of improvement in limits of detection (LOD) to literature

Reporter	Instrument cost	Point of care?	Detection scheme	Limit of detection†	Source
Quantum dots (lateral flow assay)	~$10+ mobile device	Yes	Quantum dot labels excited with UV LEDs and ratiometrically detected with mobile phone without any optical filters	7-12x improvement compared to chromophoric gold labels on scanner; LOD ~2 fmol	This work
Quantum dots (lateral flow assay)	>$100+ mobile device	Somewhat	Quantum dot labels excited with UV LEDs and detected with portable CMOS sensor with optical filters	No quantitative data for negative control shown; 2 ng/mL sample distinguishable from 1 ng/mL sample (no sample volumes given)	[92]
Traditional fluorophore (lateral flow assay)	~$1000 + mobile device	Yes	Fluorescein or $Ru(bpy)_3$ fluorophores excited with blue LEDs and detected with mobile phone with a standard fluorescence filter cube and lens	10x improvement relative to chromophoric gold labels; LOD ~10^5 cfu/mL of *E. coli* and salmonella	[38]
FRET with quantum dot donors and Cy3 acceptors	~$10+ mobile device	Yes	Excited with UV LEDs and detected with iPad mini (no optical filters, but Stokes shift enhanced with FRET)	450 fmol LOD	[56]
Enzyme-catalyzed fluorogenic production of quantum dots	>>$1000	No	Spectrometer (290 nm arc lamp excitation)	6.5x improvement in limits of detection compared to chromogenic enzymatic labeling	[93]
Upconverting phosphor (lateral flow assay)	~$1000	Yes	Excitation in near-infrared and detection at 540 nm with a benchtop strip reader	116 ng/mL (1.16 ng or est. 140 fmol); comparable to lab-based test	[94]
Phosphor (lateral flow assay)	~$1000	Yes	Excitation with 370 nm UV lamp (or with UV LEDs) and imaged with a gel imager with 8-minute exposure	10x improvement in LOD compared to gold nanoparticle labels	[32]

†Improvement relative to gold nanoparticles (when possible) is shown to facilitate comparison as authors use differing definitions of limits of detection (*e.g.* 2 or 3 standard deviations above mean negative control intensity)

Indeed, we observed limits of detection with unmodified mobile phone cameras that are 7-12-fold better than lab-based, gold nanoparticle-labeled immunoassays imaged with scanners, which are comparable to limits of detection obtained with laboratory fluorescence readers such as a gel imager at a much lower cost (the smartphone module costs less than $10 in parts, compared to standard optical filters (*e.g.* interference filters) that cost hundreds of dollars). This compares favorably with previous fluorescence lateral flow assays imaged with mobile phones, which improved limits of detection by 10 to 40-fold relative to gold nanoparticle labels, but at the considerable expense of $100 to $1000 of additional optical components such as lenses and filters.[38,45] The improved performance at lower cost is despite our use of analytes diluted in more realistic and challenging (higher autofluorescence) simulated clinical samples rather than in pure buffer. The technical principle that underpins this innovation is that the Bayer filters that distinguish red, green, and blue

light on mobile phone cameras discriminate between the fluorescence emission of large Stokes shift quantum dots in the red channel and the excitation photons from low-cost, high-power ultraviolet LEDs in the blue channel. The mobile phone ratiometric imaging approach described in this section is a first step toward enabling low-cost, fluorescence lateral flow immunoassays at the point of care by eliminating the need for costly external optical filters.

4.6 Conclusions

This specific aim describes a mobile phone-imaged fluorescence assay that does not require any external optical filters. The key insight motivating this innovation is that smartphone cameras' onboard Bayer filter discriminates between ultraviolet excitation light and fluorescence emission (in the visible spectrum) of long Stokes shift fluorophores. The particular combination of phone or USB-powered ultraviolet light-emitting diodes, high Stokes shift quantum dots, ratiometric algorithmic analysis, and detection with unmodified camera phones was the first demonstration of improved limits of detection without a substantial increase in imaging hardware cost. Another key advance pioneered in this section is validation with multiple mobile phone models, including those with different camera sensors and spectral sensitivities. Together, these two innovations may enable translating fluorophore-labeled lateral flow tests to the point of care.

5 Disposable platform for nucleic acid amplification based on a single USB-powered printed circuit board

"A man who dares to waste one hour of time has not discovered the value of life."
– Charles Darwin in a letter to his sister, Susan, in 1836, from *The Life and letters of Charles Darwin, including an autobiographical chapter* by Frank Darwin, 1887.

5.1 Summary

5.1.1 Abstract

Recent advances in electronics and microfluidics have led several research groups to develop fully integrated, sample-to-result isothermal nucleic acid amplification test (NAAT) platforms for the point of care. However, translating these platforms beyond the clinic to low-resource settings including homes has been limited by high component counts and cost. Many NAATs include complex, multi-component heater electronics based on flex circuits, Peltier elements, multiple printed circuit boards (PCBs), or costly sensors to support lysis, sample deactivation, and nucleic acid amplification. In contrast, current commercial assays for home use, such as those for pregnancy or ovulation, that include electronics typically have just one onboard PCB. In this aim, we describe a generalizable strategy to integrate all heaters and the electronics needed to control them onto a single low-cost, USB-powered PCB. We built a multiplexable disposable NAAT ("MD NAAT") platform that applies these principles, integrating small-area heaters that heat small regions to near-boiling (for pathogen lysis and sample deactivation) and large-area heaters (for amplification) on the same PCB. We show that both classes of heaters have high intra-board and inter-device reproducibility despite only heating a NAAT cartridge from below. We validated the small area heaters by lysing *Staphylococcus aureus* cells and the large area heaters by performing 2 isothermal NAATs (isothermal strand displacement amplification (iSDA) and loop-mediated isothermal amplification (LAMP)). These results demonstrate the merit of integrating NAAT heaters and control electronics onto a single printed circuit board and are a step toward translating NAATs to the home.

5.1.2 Academic contributions

Parts of this aim will be submitted to a peer-reviewed journal in collaboration with Mike Purfield, Joshua Buser, Sujatha Kumar, Katriel Looney, Erin Heiniger, Joshua Bishop, and Paul Yager.

5.2 Introduction

Over eleven percent of total deaths are caused by infectious diseases, causing 6.3 million deaths globally in 2016.[1] Highly sensitive and specific diagnostic tests are needed to facilitate early diagnosis and treatment, especially at the point of care. Paper-based assays such as lateral flow tests are suitable for the point of care due to their low cost, rapid time-to-result, and minimal user steps, but they suffer from poor sensitivity.[4,21,42] In contrast, many nucleic acid amplification tests (NAATs) are highly sensitive and specific but require complex user or manufacturing steps and/or costly instruments,[96] thereby relegating them to laboratory use. One strategy to combine the merits of both assay formats is to isothermally amplify nucleic acids in a paper-and-plastic point-of-care device and

to image with a mobile phone, as our lab first demonstrated in 2016 with the "MAD NAAT" platform (multiplexed autonomous disposable NAAT).[79]

Several recent publications describe microfluidic NAAT platforms.[79,80,97–99] Several steps in the NAAT workflow require heating, such as sample deactivation and nucleic acid amplification. Many NAAT platforms therefore include on-board chemical[100–103] or electrical[79,80,97] heaters. However, most of these platforms (especially devices integrating sample lysis) have large component counts and require complex assembly steps. For example, our lab's own MAD NAAT platform required 57 discrete components that were precisely aligned and soldered.[79] Other NAATs in the literature similarly rely on external heaters,[98] flexible circuits,[97] costly temperature sensors,[97] Peltier elements,[99] or multiple printed circuit boards[79] to precisely attain or maintain NAAT-relevant temperatures. In contrast, current commercial point-of-care tests intended for home use (*e.g.* disposable automatic digital pregnancy or ovulation tests such as the Clearblue™ digital) integrate all electronics onto a single rigid printed circuit board with surface mounted components.

In this aim, we describe a strategy to substantially improve point-of-care NAAT platform manufacturability by integrating all power distribution, heater, communication, and control electronics onto a single, 2-layer rigid printed circuit board (PCB), which we call the "MD NAAT" (multiplexable disposable NAAT[†]). The PCB includes both surface-mounted resistors for localized heating (*e.g.* for lysis heating or valve actuation) and controlled-resistance wire traces for heating large areas uniformly (*e.g.* for amplification) in microfluidic cartridges. We describe a reproducible strategy to provide good thermal contact between the heater and other disposable elements while minimizing undesired heating of other device components. Finally, we show the platform's utility to lyse bacteria and amplify nucleic acids in paper despite only heating a cartridge from below. The integrated heaters in the MD NAAT are a substantial step toward translating NAATs from laboratories to the home.

5.3 Methods

The device consists of a rigid printed circuit board, disposable paper and plastic cartridge with amplification reagents, and an outer sleeve to insulate the assay (**Figure 5.1**). The printed circuit board contains regions with localized resistor-based heaters and a large area with a resistive wire trace heater. Thermally conductive tape (3M 8815) adheres the printed circuit board heaters to the disposable cartridge. Note that in the development phase of this device, we have reused the PCBs, but replaced all fluidic components after each use to prevent contamination of samples from one test to the next. It is possible for a commercial implementation to continue this practice, with the PCB as part of a permanent instrument and the fluidic components as the disposable. However, we consider that the PCB could be so inexpensive at production scale that it could be permanently affixed to the fluidic components and be disposed of as a single unit after a single use as with commercial pregnancy or ovulation tests.

---

† Note that the loss of the "A" from our published MAD NAAT device is because the device is no longer autonomous after replacing onboard batteries with USB power.

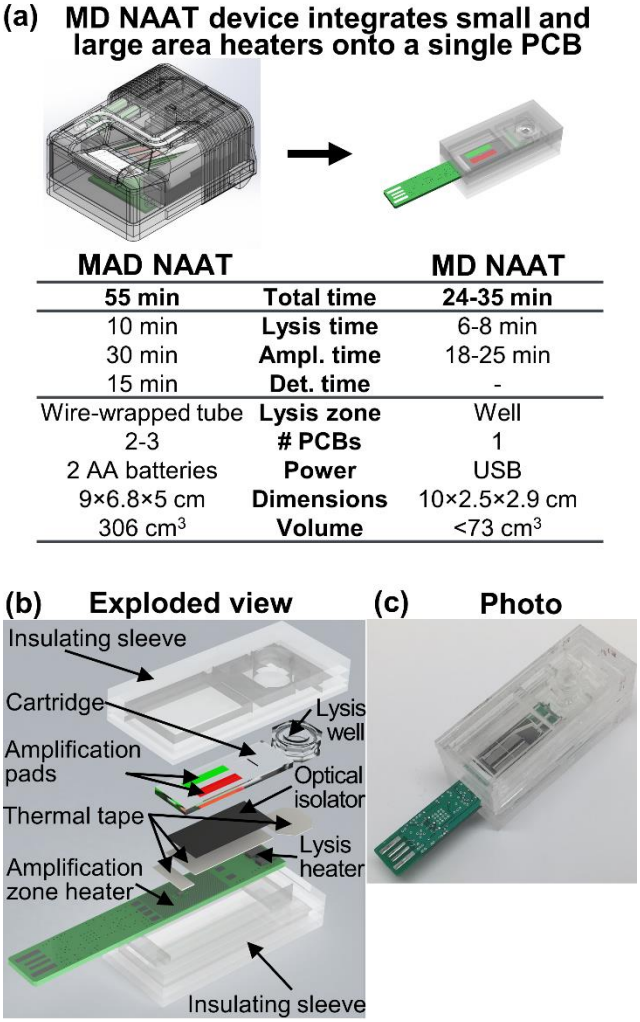

Figure 5.1: Summary of the multiplexed, disposable NAAT (MD NAAT) and its autonomous predecessor, the MAD NAAT**.** (**a**) The new MD NAAT platform reduces device complexity and size (by integrating all electronics on one PCB) while also lowering time to result. (**b**) The new MD NAAT device implements large-area (*e.g.* amplification zone) and small area (*e.g.* lysis) heaters, along with their control electronics, on a single 2-layer USB-powered PCB. (**c**) A photo of the MD NAAT device shows that the amplification pads are visible through the plastic insulation (*i.e.* compatible with real-time or in situ optical detection) because the PCB heats the cartridge to lysis and amplification-relevant temperatures from below.

5.3.1 Design of the insulated sleeve

For fluorescence assays, an optically clear, nonfluorescent insulated sleeve was designed by layering laser-cut, chemically welded 1/16" and 1/8" PMMA sheets. Air voids were located above and below the temperature-regulated zone in which nucleic acid amplification occurred to minimize conductive losses through the PMMA. A mobile phone (Nexus 5X) fluorescence reader (with filters for fluorescein and Texas Red) was fixed 15 cm above the insulated sleeve to balance the competing needs of maximizing the field of view while ensuring a sufficient numerical aperture to resolve fluorophores at amplification-relevant concentrations (details of the phone reader and image processing are detailed in Aims 4 and 5 (Chapters 6 and 7).

5.3.2 Design of the cartridge and electronics

The disposable cartridge consisted of a PMMA base and glass fiber membranes in which nucleic acid amplification occurred (**Figure 5.1b**). The 1.59 mm-thick base layer of the PMMA cartridge contained two 0.45 mm deep laser-etched regions into which 3×15 mm glass fiber membranes (GE Standard 17) were placed (about 20 µL capacity). The cartridge also contained an upstream lysis well (about 300 µL volume), which had two additional laser-cut PMMA layers bonded with dichloromethane (~3.6 mm thick total). The cartridge top was sealed with clear adhesive tape (Bio-Rad MSB1001), while the bottom of the amplification zone was optically isolated from the printed circuit board with a 0.1 mm-thick sheet of black low-density polyethylene (LDPE, McMaster-Carr). Thermally conductive tape (3M 8810) adhered the LDPE to the printed circuit board (PCB). An exploded view and photo of the cartridge are shown in **Figure 5.1**.

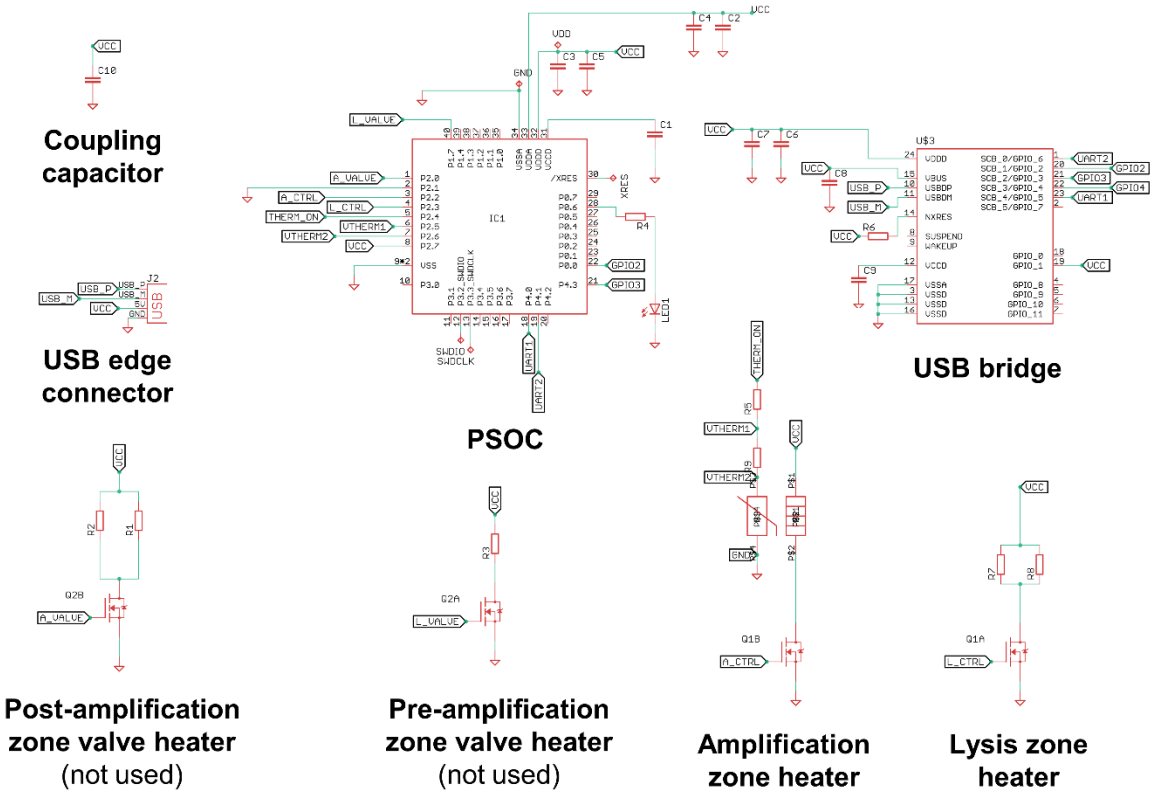

Figure 5.2: Printed circuit board schematic shows the functional elements of the MD NAAT PCB with the electronic components used to implement them. The PCB schematic was designed by Mike Purfield and Joshua Bishop.

The PCB was a standard 2-layer board made of FR-4 (150 °C glass transition temperature); was powered by universal serial bus (USB, 5V at up to 500 mA); and contained a microcontroller and USB interface bridge (Cypress Semiconductor CY8C4245LQI-483 and CY7C65211-24LTXI). **Figure 5.2** above shows a schematic of the PCB; layers are detailed in **Figure 5.3** and **Table 5.1.**

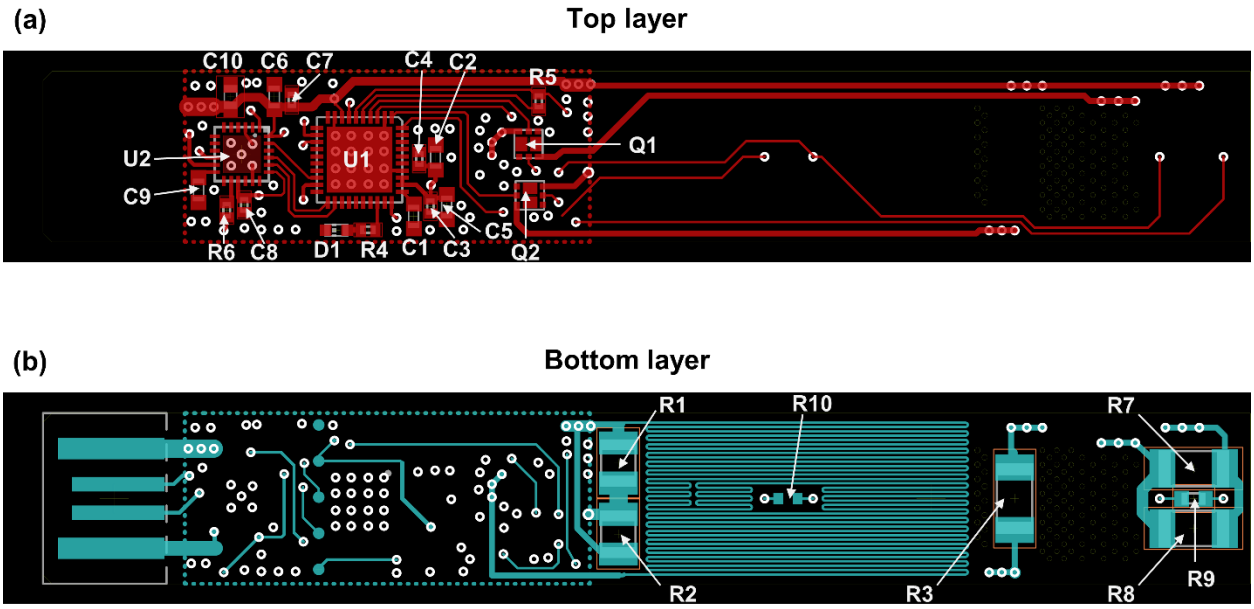

Figure 5.3: Top (**a**) and bottom (**b**) views of the USB-powered printed circuit board underlying the MD NAAT. The board implemented all heaters on the bottom layer. The board includes heating zones for: lysis (far right), pre-amplification valves (not used), nucleic acid amplification (center), and post-amplification valves (not used). The initial design and layout of the PCB was done by Mike Purfield and Joshua Bishop.

Table 5.1: Printed circuit board heater bill of materials

	Component (value, package*)	Manufacturer**	Part number	Quantity	Unit price†	Reference
1	MOSFET (6-VDFN)	Vishay	FDMA1024NZ	2	$0.5733	Q1, Q2
2‡	PSOC (32 KB flash 4 KB SRAM, 40-QFN)	Cypress	CY8C4245LQI-483	1	$2.9835	U1
3‡	USB bridge (24-QFN)	Cypress	CY7C65211-24LTXI	1	$2.262	U2
4	White LED (0603)	Osram	LW Q38E-Q1OO-3K6L-1	1	$0.204	D1
5	Resistor (360 Ω, 0402)	Panasonic	ERJ-2RKF3600X	1	$0.0183	R4
6	Capacitor (100 nF, 0402)	Murata	GRM155R71C104KA88D	4	$0.0152	C3, C4, C7, C8
7	Capacitor (1000 nF, 0603)	Murata	GRM188R61A105KA61D	6	$0.039	C1, C2, C5, C6, C9
8	Capacitor (4700 nF, 0603)	Kemet	C0603C475K9PACTU	1	$0.0565	C10
9	Resistor (4700 Ω, 0402)	Panasonic	ERJ-2RKF4701X	1	$0.0225	R6
10	Resistor (10 Ω, 1210)	Panasonic	ERJ-14YJ100U	2	$0.0551	R1, R2
11	Resistor (10 Ω, 2010)	Panasonic	CRCW201010R0FKEF	1	$0.0993	R3
12	Resistor (20 Ω, 2010)	Panasonic	CRCW201020R0FKEF	2	$0.0993	R7, R8
13	NTC thermistor (10 kΩ, 0402)	Panasonic	ERT-J0EG103FA	2	$0.0839	R9, R10
14	PCB	Sunstone			$3.51	
	Total				**$11.07†**	

*Package sizes are in imperial package sizes
†Prices are at laboratory scale (100 units)
‡Components that only needed for laboratory development
** All components except the printed circuit board were purchased from Digikey

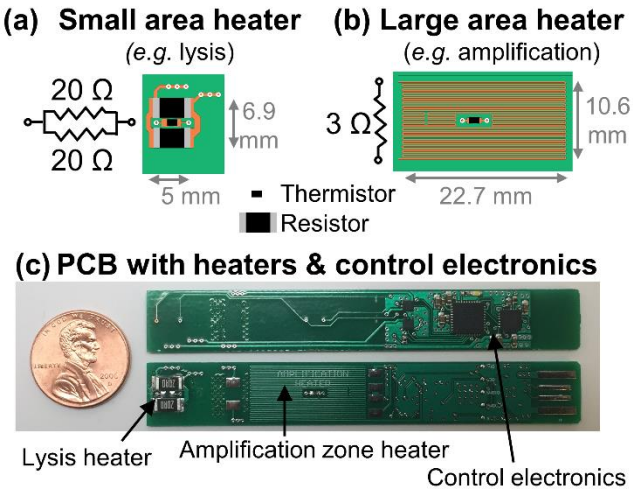

Figure 5.4: Diagrams of the two types of heaters on the PCB. (**a**) The small-area heaters consisted of surface-mounted resistors in parallel (the heater can be made smaller by using a smaller resistor package). (**b**) The large area heater consisted of a serpentine copper trace in the PCB itself. The temperatures of both types of heaters can be actively regulated with a thermistor *via* proportional-integral control. (**c**) A photo of the top and bottom of the MD NAAT PCB which implements both heater types (bottom layer) and control electronics (top layer) on just one PCB, with a US penny for scale. The MD NAAT PCB includes areas for optional post-lysis or post-amplification valves, but these are not used here. The PCB was initially designed and laid out by Mike Purfield and Joshua Bishop, but was modified by this author.

Amplification zone temperatures were actively regulated to 55.3 °C with proportional-integral control (K_p=65535, K_i=10) by passing current through a serpentine trace (nominal 3 Ω resistance) and monitoring a NTC thermistor (Panasonic ERT-J0EG103FA) in the middle of the amplification zone at 5 Hz. The lysis zone was heated by passing current through two resistors (20 Ω, ¾ W each) in parallel; an optional NTC thermistor could be used to actively regulate the temperature with PID control if necessary (**Figure 5.4**). The PCB was fabricated by Sunstone Circuits (Mulino, OR) using default manufacturing parameters (2-layer board, 1 oz. copper).

5.3.3 Thermal validation

Thermal performance of the small-area heaters was evaluated by assessing the heaters' ability to heat water to near-boiling temperatures from below. Four sets of insulating sleeves and printed circuit boards were fabricated and evaluated on two separate days with three cartridges (*i.e.* replicates) on each day. The PMMA cartridges were adhered to PCBs with thermal tape, lysis wells were filled with 200 µL of water (>18.0 MΩ•cm), the heaters were powered for 8.5 minutes in open loop configuration, and liquid temperatures were monitored with T-type thermocouples for ten minutes at 1 Hz.

Given the lower thermal mass and target temperatures of the amplification zone compared to the lysis zone, we monitored the temperature of the thermistor (at 5 Hz) during NAAT runs on two sets of insulating sleeves and PCBs and nine cartridges (*i.e.* replicates) over two days. Statistical analysis consisted of performing two-way ANOVAs on the ramp-up time to threshold temperatures. All data analysis was performed in Microsoft Excel 365 and MATLAB R2019a.

5.3.4 Nucleic acid amplification chemistry

Nucleic acid amplification was performed in glass fiber membranes *via* isothermal strand displacement amplification (iSDA); details of materials and procedures are in Lafleur et al.[79] The

membranes were typically laser cut, blocked in 1% bovine serum albumin + 0.1% Tween-20 for 1 hour, and dried at 45 °C in an incubator at least overnight before use. Each pad contained 18 μL of iSDA master mix as described previously; briefly, the chemistry consisted of: inorganic potassium phosphate buffer (pH 7.6, 50 mM), magnesium sulfate (5.63 mM), an equimolar mix of deoxynucleotides [dATP, dCTP, dGTP, dTTP] (0.4 mM), trehalose (0.27 M), 500 kD dextran (4.8% (w/v)), DNA primers (500 nM forward, 250 nM reverse, 50 mM of each bumper primers), target-specific fluorescent probes (minor groove binders) labeled with a Texas Red analog (AquaPhluor-593, 200 nM), internal amplification control-specific probes labeled with 6-FAM (200 nM), Bst 2.0 Warmstart DNA polymerase (New England BioLabs, 300 U/μL), Nt.BbvC1 nicking enzyme (New England BioLabs, 2.4% (v/v)), and nuclease-free water. The trehalose and dextran aided enzyme preservation and controlled rehydration.[79] Nucleic acid sequences of primers, probes, and DNA templates are published in Lafleur *et al.*[79] Typically, the master mix was pipetted onto blocked pads, flash-frozen with liquid nitrogen, lyophilized for at least 2 hours, and stored in heat sealed, aluminized Mylar pouches at room temperature with desiccant until use.

5.3.5 Performing the NAAT

NAAT runs on the MD NAAT device consisted of placing the PCB and cartridge assembly in the insulated PMMA sleeve, powering *via* USB, and performing sample lysis and/or nucleic acid amplification. Sample lysis methods followed Heiniger *et al.* and Buser *et al.*;[101,104] briefly, methicillin-resistant *Staphylococcus aureus* (strain FPR3757, ATCC BAA-1556) was grown to mid-log phase and suspended in 10 mM Tris buffer (pH 8.0). Ten thousand MRSA cells (100 μL) were added to the lysis well of a cartridge along with 100 μL of achromopeptidase (ACP) enzymes (Sigma A3547, 3.0 U/μL in 10 mM Tris), and the mixture was incubated for two minutes. The lysate was thermally deactivated in the MD NAAT by heating for 4 minutes with a small area heater unless otherwise indicated.

For amplification reactions, two glass fiber pads containing lyophilized iSDA reagents were placed in the cartridge and were rehydrated with 20 μL of MRSA lysate (for MRSA-positive samples), 10^5 copies of single-stranded IAC DNA (for positive controls), or 10 mM Tris buffer (for true negatives). The cartridges were then sealed, and the PCB was powered by USB and heated the amplification zone for 45 minutes. A mobile phone fluorescence reader (detailed in the following aim in Chapter 6) imaged the amplification zone in time-lapse mode using the Android Camera FV-5 application (0.25 second exposure, ISO 3200, incandescent white balance, about 30 seconds between frames, flash on). The mobile phone reader was equipped with multipass fluorescence excitation (over the flash) and emission (on the camera) filters for fluorescein and Texas Red (Semrock Brightline dual-band bandpass filter). Amplification reactions were also performed in a plate reader (Molecular Device SpectraMax iD3) by mounting glass fiber pads containing lyophilized iSDA reagents onto a clear PMMA plate which was laser cut to the size of a 384-well plate. The glass fiber pads were positioned so that they corresponded to 4 wells of a 384-well plate. The plate reader heated the trays to 50.5 °C and imaged the pads in fluorescence kinetic mode (593 nm excitation, 650 nm emission, 1 s exposure).

5.4 Results

5.4.1 Thermal validation

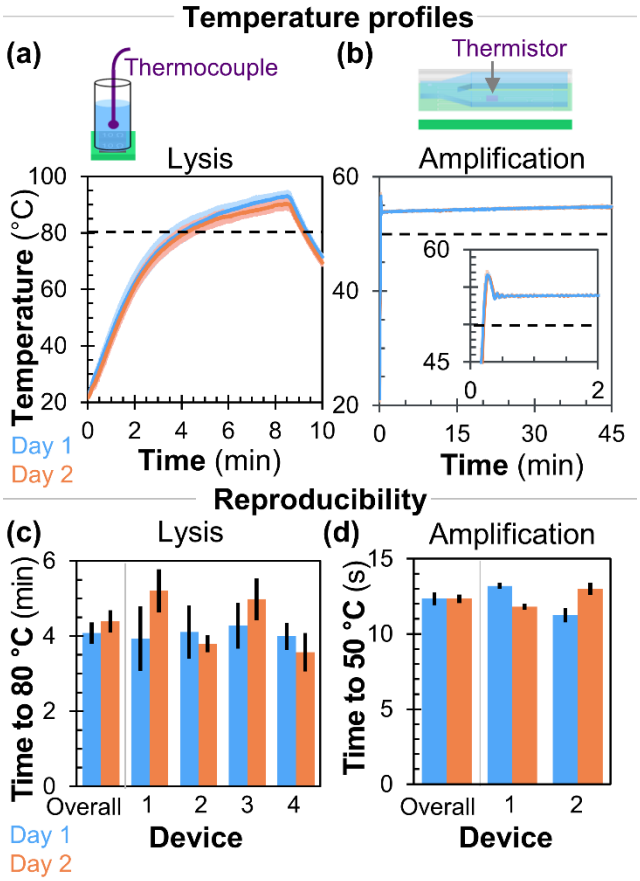

Figure 5.5: Small area and large area heaters were reproducible between multiple devices and days. (**a**) Temperature profiles of a thermocouple in a liquid-filled well above a small area heater that was powered for 8.5 minutes were reproducible between days (curves show average and 95% confidence intervals of data from four devices with three replicates each). (**b**) Temperature profiles of a thermistor in the large area heater during nucleic acid amplification runs also showed substantial reproducibility (curves showed average and 95% confidence intervals from nine runs on two devices). Panels c and d show ramp-up times (time to 50 °C (**c**) and 80 °C (**d**)) for the profiles in panels a and b; bars indicate mean and standard error of the mean. There was no significant difference in ramp-up time between days or groups for both types of heaters ($p>0.05$, two-way ANOVA).

We initially validated the thermal performance of the localized and large-area heaters on the printed circuit board. In both experiments, laser cut PMMA cartridges with flat bottomed surfaces were adhered to the PCB with thermally conductive tape. First, we assessed whether surface-mounted resistors could heat a liquid-filled well to near-boiling temperatures reproducibly from below, which is a common operation in NAATs to lyse pathogens or deactivate enzymes. Two 20 Ω resistors (¾ W) in parallel were powered with about 500 mA total in open-loop configuration for 8.5 minutes. **Figure 5.5a** shows temperature-time profiles of thermocouples in wells filled with 200 µL of water. The liquid temperature reached 80 °C in about 4 minutes on four devices (n=3) on two days (**Figure 5.5c**). The temperature continued to increase to about 90 °C while the resistors were powered (*i.e.* until 8.5 minutes). The liquid was above 80 °C for about 5 minutes on average. **Figure**

5.5c shows that there was no significant difference in the ramp-up time to 80 °C between devices or days at the 5% significance level (respectively: p=0.37 and p=0.46, two-way ANOVA).

Second, we assessed the ability of the large-area wire trace heaters to attain NAAT-relevant temperatures on two devices on two days. The wire traces were supplied with 5V under proportional-integral control (set point 55.3 °C). We actively monitored the temperature of the NTC thermistor protruding from the middle of the amplification zone at 5 Hz. **Figure 5.5b** shows that the amplification zone reached NAAT-relevant temperatures with a slight 1.4 °C overshoot at 20 seconds relative to the set point of 55.3 °C on day 1 (n=9); similar results were observed on day 2. All devices reached 50 °C within 13 seconds. The temperature of the amplification zone was 53.97±0.26 °C (mean ± 95% confidence interval) at 30 seconds and rose slightly to 54.77±0.30 °C at 45 minutes. As before, there was no significant difference in the ramp-up time to 50 °C between devices or days at the 5% significant level (**Figure 5.5d**, p=0.57 and p=0.82, two-way ANOVA). Thermocouple measurements of liquid-filled cartridge temperatures suggest a ramp-up time to iSDA temperatures (>48.5 °C) of about 3 minutes (n=4, data not shown).

5.4.2 Applying small area heaters to lyse bacteria

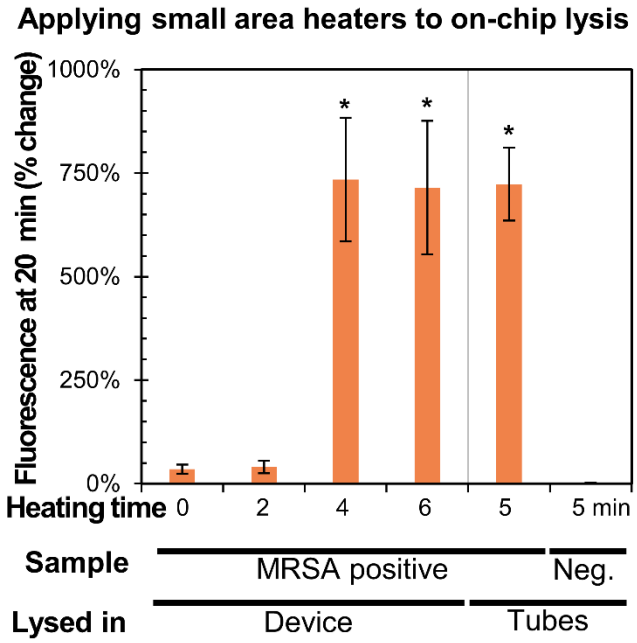

Figure 5.6: Small-area heaters lyse bacteria on chip. MRSA cells were lysed with achromopeptidase enzymes and thermally deactivated in tube controls (n=3 tubes) in a heat block or with the small area heaters in the MD NAAT (n=3 devices). Twenty μL of each lysate then rehydrated 3 lyophilized pads containing reagents for isothermal strand displacement amplification (iSDA), placed in a PMMA tray, heated to 50.5 °C, and imaged in a plate reader in fluorescence mode in real time. Samples heated in the lysis chamber for at least 4 minutes showed significantly higher MRSA-specific fluorescence than negative controls after 20 minutes of amplification (* p<0.00001, one-way ANOVA). Bars show mean and error bars show standard error of the mean.

On-chip cell lysis is a challenging step in point-of-care NAATs. In the implementation demonstrated here, this is in part due to the need to heat a specific area to near-boiling temperatures while ensuring that nearby amplification reagents (especially heat-sensitive enzymes) remain near room temperature. One strategy to lyse Gram-positive bacteria that we have shown with great success[79,101,104,105] is to use an enzyme mixture such as achromopeptidase (ACP) followed by thermal

deactivation by heating to near-boiling temperatures. We applied the localized resistive heaters to lyse methicillin-resistant *Staphylococcus aureus* (MRSA) grown to mid-log phase. About 90,000 MRSA cells were added to the flat-bottomed PMMA cartridges in 3 devices, co-incubated with ACP for 2 minutes, and thermally deactivated at a range of heating times. We assessed lysis effectiveness by using the lysate to rehydrate glass fiber pads containing lyophilized nucleic acid amplification reagents, which were then incubated in a plate reader at 50.5 °C and imaged in fluorescence mode. Real-time amplification curves show that MRSA lysate heated with the small-area heaters for 4 or 6 minutes in the MD NAAT amplify similarly to samples from tube positive controls (**Figure 5.6**). Negative controls did not amplify. The average fluorescence at 20 minutes was significantly greater than that of a MRSA-negative control ($p<0.0001$, one-way ANOVA).

5.4.3 Applying both small and large area heaters to a real-time, fluorescence NAAT

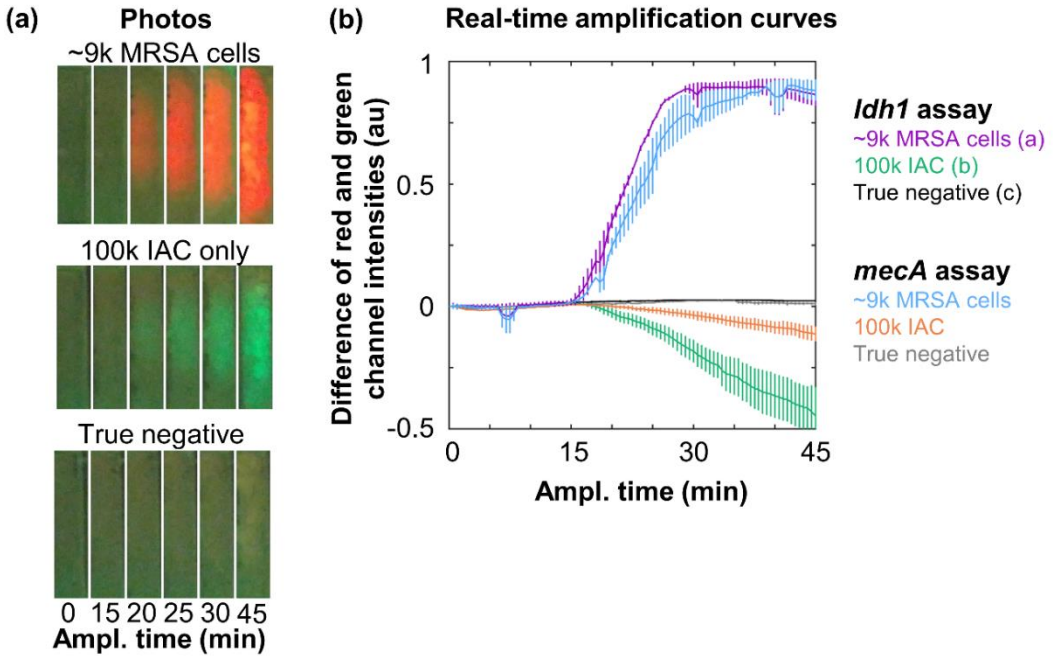

Figure 5.7: On-chip lysis and amplification with 2 assays (*ldh1* and *mecA* genes) and 3 samples in the MD NAAT. MRSA cells were grown to mid-log phase, incubated with achromopeptidase enzymes for 2 minutes, and thermally deactivated for 4 minutes by heating to ~95 °C. The lysate then rehydrated amplification (ampl.) pads containing lyophilized reagents iSDA reagents, and the pads were heated by the MD NAAT (the x-axes indicate when the amplification heaters were powered on). (**a**) Mobile phone images of pads show no amplification in the true negatives, substantial green fluorescence in pads containing only internal amplification control (IAC) DNA, and substantial red fluorescence in pads containing MRSA cells for the *ldh1* assay. Similar results were observed for the *mecA* assay. (**b**) Real-time curves show high signal-to-noise ratios and rapid amplification. MRSA-positive samples amplified in 18 minutes on average ($p<0.001$ for *ldh1* and $p<0.01$ for *mecA* relative to respective true negative controls, one-way ANOVA). Curves show mean and standard error of the mean for n=3 pads (IAC only and true negatives) or n=2 (MRSA-positive samples); positive signals (*i.e.* redder images) indicate target-specific amplification, while negative signals (*i.e.* greener images) indicate IAC-specific amplification (see Aim 4 (Chapter 6) for additional details).

Finally, we tested the small-area heaters for lysis in conjunction with the large-area wire trace heaters for amplification. We validated the heaters with 2 fluorescence assays for MRSA using a NAAT that contained fluorescent probes for MRSA (red-emitting fluorophore) or a synthetic internal amplification control (*e.g.* as a positive control, labeled with a green-emitting fluorophore).[79,106] We lysed MRSA cells in the device by incubating them in the device as before and heated the lysate for 4

minutes to thermally deactivate enzymes. The deactivated lysate then rehydrated downstream glass fiber pads containing lyophilized NAAT reagents. The NAAT reactions were heated by the large area wire trace heaters and imaged in real time with a two-fluorophore mobile phone reader for fluorescein and Texas Red. **Figure 5.7** shows images and real-time amplification curves for pads specific to the *ldh1* or *mecA* genes (which are both present in MRSA). Samples containing MRSA (about 9000 copies per pad) showed substantial red fluorescence within 20 minutes for the *ldh1* (**Figure 5.7a**) and *mecA* genes when imaged with a Nexus 5X phone. Pads containing 100k copies of internal amplification control DNA had strong green fluorescence in about 25 minutes for both assays (**Figure 5.7a**). Truly negative samples (lacking MRSA and IAC) showed neither red nor green fluorescence during the entire 45 minutes of amplification time (**Figure 5.7a**). The real-time curves in **Figure 5.7b** showed similar liftoff times for both assays: the fluorescence at 18 minutes was significantly higher in MRSA-positive samples than in the negative controls for both the *ldh1* ($p<0.0001$, one-way ANOVA) and *mecA* ($p<0.01$, one-way ANOVA) assays. Similar amplification times (~20 minutes to liftoff) were observed in loop-mediated isothermal amplification (LAMP) performed with genomic DNA in buffer (**Figure 5.8**).

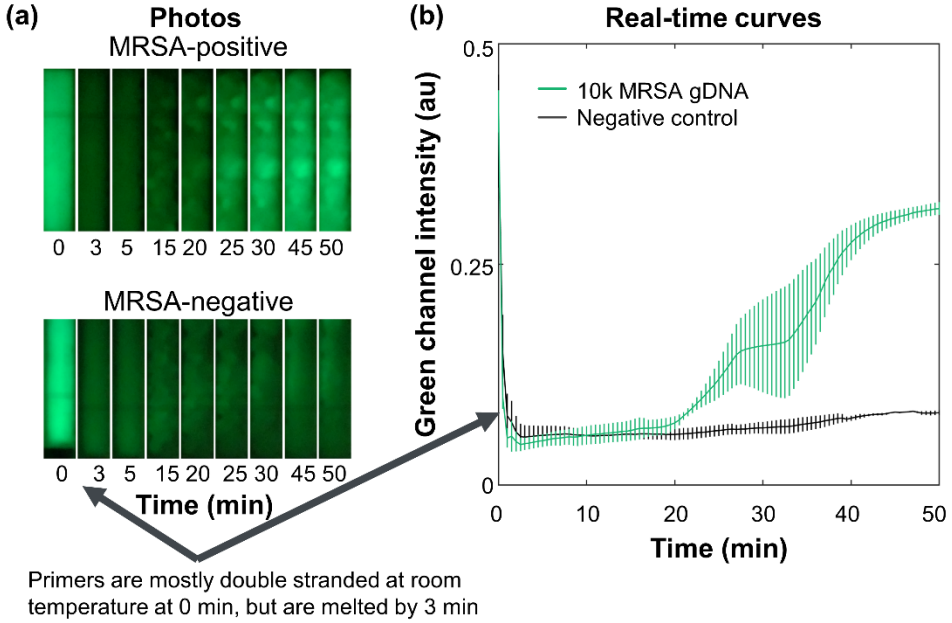

(c) Primer sequences

LAMP primer	Primer sequence	Final concentration (μM)
F3	GTACAGATCCTTTCAATCTATAGCG CATTAG	0.2
FIP	CGACTTGTTGCATACCATCAGTTAATAGATTG GGCAATATTAACGCACCTCACTTATTAAAAGACACG	1.6
FL	TTCTTTGGAAATAATATTTTTCTTCCAAACTTT	0.4
BL	GGTACTGCAGAACTC AAAATGAAAC AAGG AGA	0.4
BIP	AAAGGAAGATATTTATAGATCTTATGCAAACTTAATTGG C GATATAAACCACCCAATTTGTCTGCCAG	1.6
B3	CATTAATAGCCATCATCATGTTTGGATTATCA	0.2

Figure 5.8: Photos and real-time curves of loop-mediated amplification (LAMP) performed in the MD NAAT targeting the *mecA* gene of MRSA show the platform's ability to perform LAMP (~64 °C amplification temperature). (**a**) Photos of glass fiber pads during amplification show detectable amplification by about 25 minutes. The pads appeared fluorescent at time zero due to the use of an intercalating dye which labels all double stranded DNA (*i.e.* the primers and

templates present before the pads reach LAMP-relevant temperatures). (**b**) Real-time amplification curves in the green color channel show substantial amplification of MRSA-positive samples beyond 21 minutes ($p<0.05$ at 21 minutes and $p<0.001$ beyond 40 minutes relative to negative control, *t*-test, n=3). Bars show mean and error bars show standard error of the mean. (**c**) Sequences and concentrations of primers used in LAMP reactions. The LAMP experiment was performed by Katriel Looney.

5.5 Discussion

NAATs intended for the point of care must integrate several steps that require heating small regions to high temperatures (*e.g.* to lyse samples or actuate valves[79,107]) or large areas to specific temperatures with tight tolerances (*e.g.* for amplification). This aim describes a strategy to implement both types of heaters on a single, 2-layer rigid printed circuit board; thermal validation of the heaters; and application to sample lysis and amplification on the MD NAAT platform.

Many NAATs intended for the point of care are based on paper microfluidics, but these NAATs must overcome paper's high surface-area-to-volume ratio and low thermal mass, which substantially complicate uniform heating. Approaches to uniformly heating include incorporating materials with a high thermal conductivity,[98] high thermal mass,[79,108] or phase change at the target temperature (often coupled to exothermic chemical reactions).[79,109] However, these strategies often suffer from high component counts and are not amenable to integration onto a single rigid printed circuit board.[79,80] In contrast, the large area heater described in this work requires just 1 extra component (<$0.15 thermistor) coupled to a serpentine wire trace in the PCB. This compares favorably with recent work that used costly infrared temperature sensors (>$40) to monitor the temperature of an area heated by a serpentine trace in a flexible circuit.[97]

However, serpentine traces are not suitable for heating small areas due to PCB trace's low electrical resistivity, which cannot dissipate sufficient heat at particular location. Heating small areas rapidly with discrete, surface-mounted resistors addresses this limitation, and provides the added benefit of precisely defining the heater area with deliberate resistor package selection. One drawback of integrating small area and large area heaters onto one PCB is potentially worse thermal contact because the upper surfaces of the two classes of heaters are not coplanar (*i.e.* the resistors nominally protrude 0.6 mm and the thermistor 0.5 mm relative to the wire traces in the PCB itself).

Therefore, we explored strategies to planarize the PCB surface relative to the bottom of the NAAT cartridge. We evaluated whether strategies addressed the competing needs of rapid/uniform heating, low board-to-board variability, PCB reuse during development, and ease of manufacturing at both laboratory and larger volumes. We found that thermally conductive double-sided adhesive met these needs while ensuring consistent thermal performance between boards and days (**Figure 5.5**), which was not true for other adhesives such as CNC-machined planar thermal epoxy (which introduces irregularities from degassing, is labor-intensive, and is poorly reproducible) or polydimethylsiloxane (PDMS) tape (data not shown). Thermally conductive double-sided tape is especially useful in this application because it is available at specific thicknesses (near the nominal resistor thicknesses) and conforms to surface deformities, which ensures that the tape accommodates manufacturing defects, thermistors, or other components protruding from the PCB surface. Adhering the bottom of the cartridge to just one PCB with thermally conductive tape enabled us to perform common NAAT operations such as lysis in wells and amplification in paper (**Figure 5.7** and **Figure 5.8**). We minimized undesired heating of the amplification zone during the lysis heating step by using separate pieces of thermally conductive tape in each zone and placing an array of holes in the PCB between the two zones.

The MD NAAT, which contains a printed circuit board with integrated small and large area heaters, improves upon other heater designs in the NAAT literature. Many recent NAATs are heated by laminates such as wire traces in flex circuits or positive temperature coefficient (PTC) resistive heaters,[80,97,110] but these suffer from high component counts, costly sensors, and limited ability to scale the area heated. To our knowledge, almost all NAATs that lyse samples and amplify nucleic acids on chip require separate (or external) heaters for the two NAAT steps (or costly components). In contrast, the heaters described in this paper are integrated onto a single PCB and only heat the NAAT cartridge from below, which substantially improves manufacturability and enables real-time fluorescence detection on the MD NAAT.

To summarize, this aim describes an evolution of the MAD NAAT device that incorporates the first integrated PCB that: 1) heats both small and large areas for NAATs; 2) heats to a precise temperature reproducibly between devices; 3) is easily powered by consumer-grade electronics (USB 2.0 at 5V with maximum 500 mA current draw); 4) can be manufactured at default PCB fabrication conditions; and 5) implements standard NAAT operations such as lysis and amplification on just one printed circuit board.

5.6 Conclusions

We have demonstrated a generalizable approach to integrate large area and small area heaters onto a single, USB-powered rigid printed circuit board using default PCB manufacturer fabrication parameters. The heaters enable on-chip bacterial lysis and nucleic acid amplification on the MD NAAT platform and is a step toward translating NAATs to the home. This aim describes the first use of thermally conductive tape as the sole adhesive to planarize and transfer heat from large area and small area heaters on a single printed circuit board. Moreover, it is the first demonstration of a nucleic acid amplification test that simultaneously can be manufactured with rapid prototyping techniques, reaches near-boiling lysis temperatures, and is compatible with real-time fluorescence imaging with mobile phones.

6 Two-fluorophore, real-time imaging of nucleic acid amplification tests overcomes artifacts in highly scattering porous media

"May it be a light to you in dark places, when all other lights go out."
– Lady Galadriel as she gave a phial (vial) of light to Frodo
in J. R. R. Tolkien's *The Fellowship of the Ring*, 1954

6.1 Summary

6.1.1 Abstract

Nucleic acid amplification tests (NAATs) are common in laboratory and clinical settings due to their low time to result and exquisite sensitivity and specificity. Laboratory NAATs include onboard positive controls to reduce false negatives and specialized hardware to enable real-time fluorescence detection. Recent efforts to translate NAATs to the home sacrifice one or more of the benefits of laboratory NAATs such as sensitivity (in assays lacking onboard, co-amplifying positive controls) or time to result (*e.g.* endpoint colorimetric assays). In this aim, we describe an imaging strategy for real-time NAATs that addresses these concerns by enabling mobile phones to image two colocalized fluorophores, even in the highly scattering porous media in which almost all home assays (*e.g.* pregnancy) are performed. The strategy consists of imaging fluorophore-labeled biplexed NAATs performed in glass fiber membranes with mobile phones that have multipass excitation and emission filters on the flash and camera. We showed that mobile phones with vastly different camera spectral sensitivities imaged fluorescein and Texas Red at NAAT-relevant concentrations. However, we observed a strong evaporation-induced optical artifact in heated glass fiber pads due to changes in refractive index, which we overcame by analyzing the differential fluorescence signal between the red and green color channels of phone images. We demonstrated that the differential fluorescence imaging strategy enabled low limits of detection (316 copies of methicillin-resistant *Staphylococcus aureus* DNA) in our lab's MD NAAT platform, even in biplexed isothermal strand displacement amplification reactions containing 100k copies of co-amplifying internal amplification control DNA. These results suggest that two-fluorophore mobile phone imaging may enable translating the benefits of extant laboratory-based, real-time NAATs to the point of care.

6.1.2 Academic contributions

This section will be submitted as a manuscript in a peer-reviewed journal in collaboration with current and former members of the Yager group, including Sujatha Kumar, Vidhi Singh, Louise Hansen, Caitlin Monahan, Enos Kline, Erin Heiniger, Joshua Bishop, and Barry Lutz.

6.2 Introduction

Infectious disease diagnostic tests are increasingly intended for the point of care, including clinics or even the home. Many point-of-care assays for infectious diseases leverage the format of extant home-based assays, such as those for glucose, pregnancy, or HIV. Typically, these assays are paper-based lateral flow tests due to their minimal cost and time to result, but these are inappropriate for many infectious diseases due to poor limits of detection.[4,14,21,42,111,112] Nucleic acid amplification tests

(NAATs) are a promising class of laboratory and clinical assays that have low limits of detection and times to result by imaging amplification reactions in real time, but these often require complex user steps or bulky instruments.[9,11,83,96,113,114] Recent NAATs intended for the point of care typically sacrifice time to result by performing amplification in paper or plastic substrates and monitoring endpoint absorbance by eye or mobile phones.[79,83,97,115]

Several research groups advocate imaging point-of-care assays with mobile phones due to phones' ubiquity, low cost, ease of use, and breadth of integrated hardware.[23,42,83,111,116,117] These arguments are predicated on either leveraging end users' mobile phones (*e.g.* for home use) or manufacturing low-cost, near-disposable assay readers integrating the low-cost camera and communications hardware used in mobile phones. However, most of the mobile phone-imaged assay literature demonstrates compatibility with just one camera sensor module or product line, even for assays imaged by multiple mobile phone models.[56,79,83,117,118] Indeed, many assays take advantage of a quirk of a particular phone model, such as a xenon lamp camera flash[119] or atypically long exposure time,[120] to improve assay performance. In contrast, we demonstrated recently that ratiometric imaging enables highly sensitive fluorescence measurements without optical filters on multiple mobile phone models, including phones with differing camera spectral sensitivities, by exciting long Stokes shift fluorophores with ultraviolet light-emitting diodes (LEDs).[111] However, there remains a need in the literature to image standard, short Stokes shift fluorophores with multiple mobile phone models with appropriate integrated controls.

Integrated positive controls are a necessary component of amplification-based point-of-care diagnostic tests. Such controls enhance an assay's specificity by discriminating between purported negative results and assay failure (thereby minimizing false negatives).[103,121–124] For example, real-time NAATs often include additional fluorescent probes that are detected in an orthogonal detection channel to monitor nontarget background amplification products.[106,125] In contrast, many point-of-care assays spatially separate such positive controls from the signal of interest and use the same optical detection strategy (*e.g.* visual readout with chromophore-labeled lateral flow strips)[4,17,21,79] to detect both regions of interest. However, real-time NAATs cannot always rely on spatially separated positive controls: false negatives are possible when amplification fails in the region corresponding to the signal of interest even if amplification occurs in the positive control region (*e.g.* due to heater or fluidic failure).

In this aim, we describe a hardware and signal processing innovation that image 2 colocalized fluorophores with mobile phones, which enables real-time, point-of-care NAATs. Multipass excitation and emission filters were attached to the flash and camera of multiple mobile phone models, which allowed us to image fluorophores at NAAT-relevant concentrations in optically scattering media such as paper. We observed that evaporation during amplification introduces an optical artifact that we overcame with a differential optical signal processing scheme. Finally, we applied these insights to our lab's multiplexed, disposable NAAT ("MD NAAT") platform, wherein we imaged biplexed isothermal strand displacement amplification reactions in real time (**Figure 6.1**). These results suggest a path toward translating real-time fluorescence NAATs to the home.

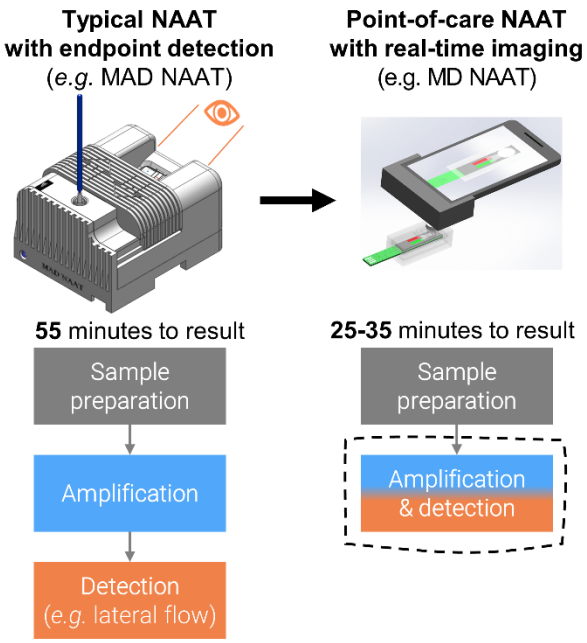

Figure 6.1: Overview of the nucleic acid amplification test (NAAT) fluorescence reader. Typical NAATs with endpoint detection (*e.g.* with lateral flow strips) require discrete sample preparation, amplification, and detection steps, which we previously implemented in the "MAD NAAT" device. This aim describes a strategy to reduce time to result by detecting amplifying nucleic acids in real time with a two-fluorophore mobile phone reader, which we validate by imaging the "MD NAAT" platform in real time.

6.3 Methods

6.3.1 Operating principle

We built a two-fluorophore mobile phone reader to image biplexed NAATs amplifying in real time. The reader detects fluorescein and Texas Red, which can both be excited with a broadband light-emitting diode (*e.g.* phone flash coupled to a multipass excitation filter) and simultaneously detected with a standard smartphone camera (with a multipass emission filter). In typical operation, the phone flash light-emitting diode (LED) emits white light, which is filtered by the excitation filter and excites fluorescein and Texas Red. The fluorescence emission then passes though the emission filter and is detected by the phone's camera (**Figure 6.2a** on page 63). Fluorescence emission from fluorescein is detected in the green color channel of phone photos, while emission from Texas Red is detected in the red color channel of phone photos due to the Bayer mosaic filter on the camera sensor. **Figure 6.3** shows the spectra of the phone LED, filters, and camera photo color channels. We also calculated the differential fluorescence signal between the red and green color channels, which we define in **Equation 6.1**:

Equation 6.1:
$$\boldsymbol{Differential\ fluorescence} = I_{\mathbf{red},\gamma\mathbf{-corrected}} - I_{green,\gamma-corrected}$$

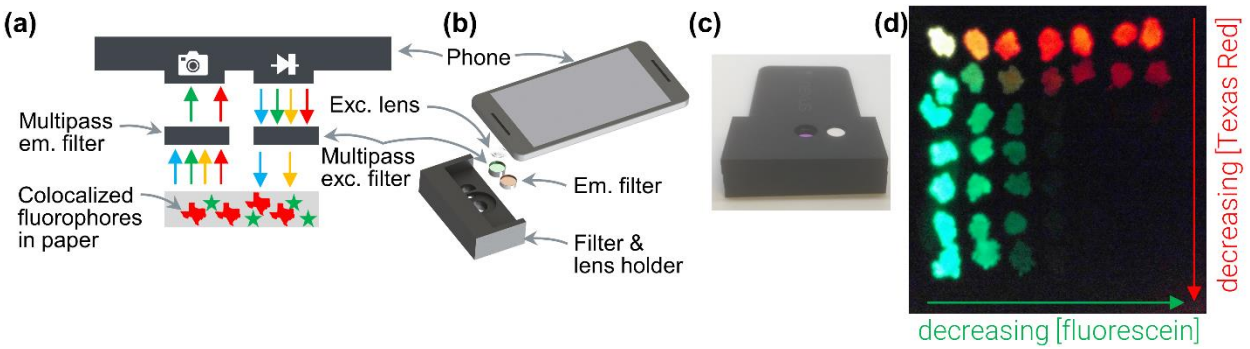

Figure 6.2: Design of a mobile phone fluorescence reader that images two colocalized fluorophores, such as in point-of-care NAATs, in real time. (**a**) A cartoon of the mobile phone fluorescence reader shows how multipass excitation (exc.) and emission (em.) filters image colocalized fluorophores simultaneously. (**b**) CAD rendering and (**c**) photo of the fluorescence reader. (**d**) Photo of 49 spots of fluorophore mixtures of Texas Red and fluorescein on glass fiber show a phone's ability to image fluorophores at NAAT-relevant concentrations over a large 5 × 5 cm field of view (2nd and 3rd row/column from left and top). Noncircular spot patterns are due to wicking in the glass fiber membrane. The photo in panel C was acquired by Vidhi Singh.

6.3.2 Design of the mobile phone fluorescence reader

Filter holders for two common mobile phones (Google Nexus 5X and LG Pixel 2) were designed by layering 1/16" (1.59 mm) and 1/8" (3.18 mm)-thick PMMA sheets (McMaster-Carr) that were laser cut (VLS 3.60, Universal Laser Systems) and chemically welded with dichloromethane. The filter holder design was engineered to minimize light leakage (including autofluorescence) with contours corresponding to the phones' profiles. Cutouts over the camera aperture and camera flash LED hold the multipass 479/585 nm excitation (Semrock FF01-479/585-12.5) and 524/628 nm emission filters (Semrock FF01-524/628-12.5) for fluorescein and Texas Red, respectively. The excitation light is partially collimated with a 12 mm-wide, 12 mm focal length plano-convex lens (Edmund Optics 45-083) placed 6 mm from the light-emitting diode. An exploded view and photo of the filter holder in **Figure 6.2**.

6.3.3 Estimating limits of detection

We estimated the limits of detection of the mobile phone fluorescence reader at conditions mimicking that of a NAAT run. We created dilution series of fluorescein (Sigma F-6377, Lot 79H0023) or Texas Red (Invitrogen T-1905, Lot 1836702) in a mock isothermal strand displacement amplification (iSDA) solutions at concentrations of 0, 100, 150, 200, 250, 300, or 400 nM. The diluent contained magnesium sulfate (3.75 mM), trehalose (270 mM), dextran (500 kDa, 4.8% w/v), and anhydrous glycerol (0.41% (v/v)) in phosphate-buffered saline (10 mM, pH=7.4). Glass fiber pads (GE Standard 17) were laser cut, placed into laser ablated PMMA cartridges, and rehydrated with 20 µL of fluorophore solution. The cartridges were mounted to the printed circuit board of our lab's MD NAAT platform with thermally-conductive tape (3M 8815) (following the procedure outlined in the previous aim and Lafleur et al.).[79] Pads were heated for about three minutes and imaged with the mobile phone reader using the Nexus 5X and Pixel 2 phones. Images were acquired with the Camera FV-5 application (ISO 1600, 0.25 sec. exposure, incandescent white balance), gamma-corrected, quantified in the red and green color channels in MATLAB R2017b, and statistically analyzed in MATLAB or Excel 365.

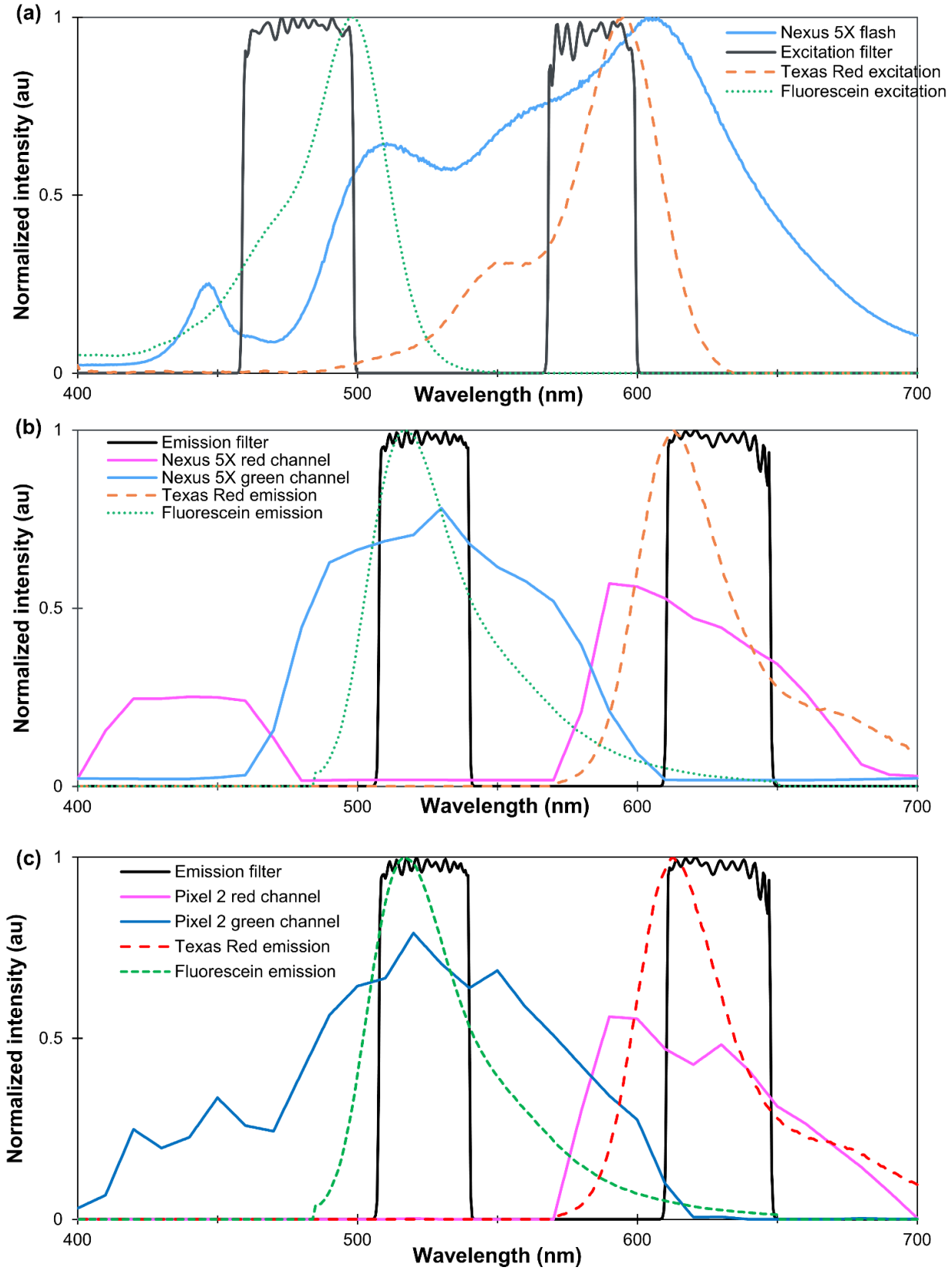
(a)
Normalized intensity (au)
1
0.5
0
400
500
600
700
Wavelength (nm)
Nexus 5X flash
Excitation filter
Texas Red excitation
Fluorescein excitation
(b)
Normalized intensity (au)
Wavelength (nm)
Emission filter
Nexus 5X red channel
Nexus 5X green channel
Texas Red emission
Fluorescein emission
(c)
Normalized intensity (au)
Wavelength (nm)
Emission filter
Pixel 2 red channel
Pixel 2 green channel
Texas Red emission
Fluorescein emission

Figure 6.3: Principle of operation of the dual fluorophore mobile phone reader. (**a**) The multi-pass excitation filter (solid black curve) transmits wavelengths of the mobile phone flash (solid blue curve) that correspond to the excitation spectra of fluorescein (dotted green curve) and Texas Red (dashed red curve). (**b, c)** The multi-pass emission filter (solid black curve) transmits wavelengths of the fluorescein (dotted green curve) and Texas Red (dashed red curve) emission that correspond to the green (solid blue curve) and red channels (solid orange curve) of photos taken by the mobile phone, respectively. Photos taken with the flash thereby image fluorescein and Texas Red. Shown are the specific flash and camera spectra of the Nexus 5X mobile phone (a, b), along with the camera spectra of the Pixel 2 mobile phone (c). Filter spectra are adapted from Semrock, and the fluorophore spectra are from ThermoFisher. Phone spectra were measured with the approach outlined in Aim 2 (section 4.3.1).

6.3.4 Characterizing evaporation artifact

Next, we characterized how evaporation in heated pads (*e.g.* during amplification) affects the fluorescence intensity observed by the mobile phone reader. Since the glass fiber pads are a highly optically scattering substrate, we first measured the refractive indices of the fibers of the glass fiber membranes to characterize the impact of light scattering on observed fluorescence intensities. We punched samples of glass fiber to 15.9 mm diameter circles, mounted them in a refractometer (Rudolph Research J157, ±0.00002 RI accuracy), and measured the refractive index at 589.3 nm and 20.0 °C. We also measured several liquid controls, including 100 μL of immersion oil of known refractive index (1.460, 1.480, and 1.500 at 589.3 nm, Cargille Series A) or 500 μL of: nuclease-free water (Ambion AM9937), *p*-xylene, and simulated NAAT master mix (water mixed with trehalose (270 mM) and 500 kDa dextran (4.8% w/v)). We also took brightfield photographs of glass fiber pads blocked with bovine serum albumin (see procedure below) that were wetted with 20 μL of water or *p*-xylene.

We then measured how observed fluorescence intensities change during a simulated NAAT run. Glass fiber pads (GE Standard 17) were blocked with bovine serum albumin (1% w/v) and Tween-20 (0.1% v/v) following Lafleur et al. and the previous aim,[79] mounted in PMMA cartridges as before, and heated for 60 minutes in the MD NAAT device. A Nexus 5X-based mobile phone fluorescence reader was mounted about 15 cm above the MD NAAT and imaged the pads about every 30 seconds with the Camera FV-5 application (ISO 3200, 0.25 sec. exposure, incandescent white balance). Images were gamma-corrected and quantified in the red and green color channels in MATLAB R2017b.

6.3.5 Applying fluorescence reader to image a NAAT in real-time

Finally, we validated the ability of the mobile phone reader to image real-time nucleic acid amplification in the MD NAAT device. We performed isothermal strand displacement amplification (iSDA) targeting the *ldh1* or *mecA* genes of *Staphylococcus aureus* and an internal amplification control (IAC). Details of procedures, primer and probe sequences, and MD NAAT fabrication and assembly parameters are found in the previous aim and Lafleur et al.[79] Briefly, glass fiber pads were laser cut; blocked as above; filled with all iSDA reagents including enzymes, primers, and probes; flash-frozen; and lyophilized. The lyophilized pads were placed in PMMA cartridges and rehydrated with samples containing genomic DNA from methicillin-resistant *S. aureus* (MRSA) strain FPR3757 (ATCC BAA-1556DQ) and/or 100k copies of IAC single-stranded DNA in nuclease-free water. Filled cartridges were sealed with PCR tape (Biorad MSB1001), adhered to the MD NAAT PCB with thermally conductive tape (3M 8815), and heated over USB power by the MD NAAT device for 45 minutes (set point 55.3 °C, K_p=65535, K_i=10).

Amplification reactions were imaged by a mobile phone (Nexus 5X or Pixel 2) equipped with multipass excitation and emission filters about every 30 seconds. We analyzed the images by masking them to the glass fiber pads, normalizing the individual color channel intensities, and gamma correcting. The differential fluorescence intensity was calculated for each pixel based on **Equation 6.1** and averaged across each glass fiber pad. Image analysis was performed in MATLAB R2019a.

6.4 Results

6.4.1 Hardware validation and limits of detection

The mobile phone reader was validated by imaging dilution series of two fluorophores with two mobile phones. First, the ability of the mobile phone reader to image a large (5×5 cm) field of view was confirmed by imaging a five-fold dilution series of Texas Red and fluorescein in phosphate-buffered saline (pH 7.4) from 20 μM to 6.4 nM (and negative controls) in all combinations of Texas Red and fluorescein that had been pipetted onto a GE Standard 17 membrane (10 μL per spot). Fluorophores were visible at levels relevant to the NAAT fluorescent probe levels (200 nM) as suggested by visible spots in the 2nd and 3rd columns and rows of **Figure 6.2d**.

Next, the phones' fluorophore limits of detection were determined at NAAT-relevant conditions (**Figure 6.4a**). Fluorophore-filled glass fiber pads that were heated in the MD NAAT with mock iSDA master mix and imaged with two phones. Both phones detected fluorescein in the green color channel and Texas Red in the red color channel (Pearson product-moment correlation coefficient: $r>0.98$, $p<0.001$, *t*-test). Texas Red detected in the red color channel showed limits of detection of 1.2 pmol (Nexus 5X) and 1.7 pmol (Pixel 2), while fluorescein detected in the green color channel had LODs of 0.64 pmol (Nexus 5X) and 3.7 pmol (Pixel 2). The observed limits of detection were lower than the nominal fluorescent probe amounts during a NAAT run (4.0 pmol). There was no significant difference in the sensitivity to Texas Red or fluorescein for both phones ($p>0.7$).

We measured crosstalk by assessing to what extent fluorescein was detected in the red color channel and Texas Red in the green color channel. There was no correlation between Texas Red concentration and fluorescence in the green color channel on both phones as indicated by the near-zero slopes and correlation coefficients in **Figure 6.4b** ($r=0.4$, $p>0.2$). However, there was a slight negative correlation between fluorescein concentration and fluorescence in the red color channel ($r=-0.8$, $p=0.01$), albeit with a small effect size (the slope in the red color channel was -⅛ the slope in the green color channel, **Figure 6.4c**).

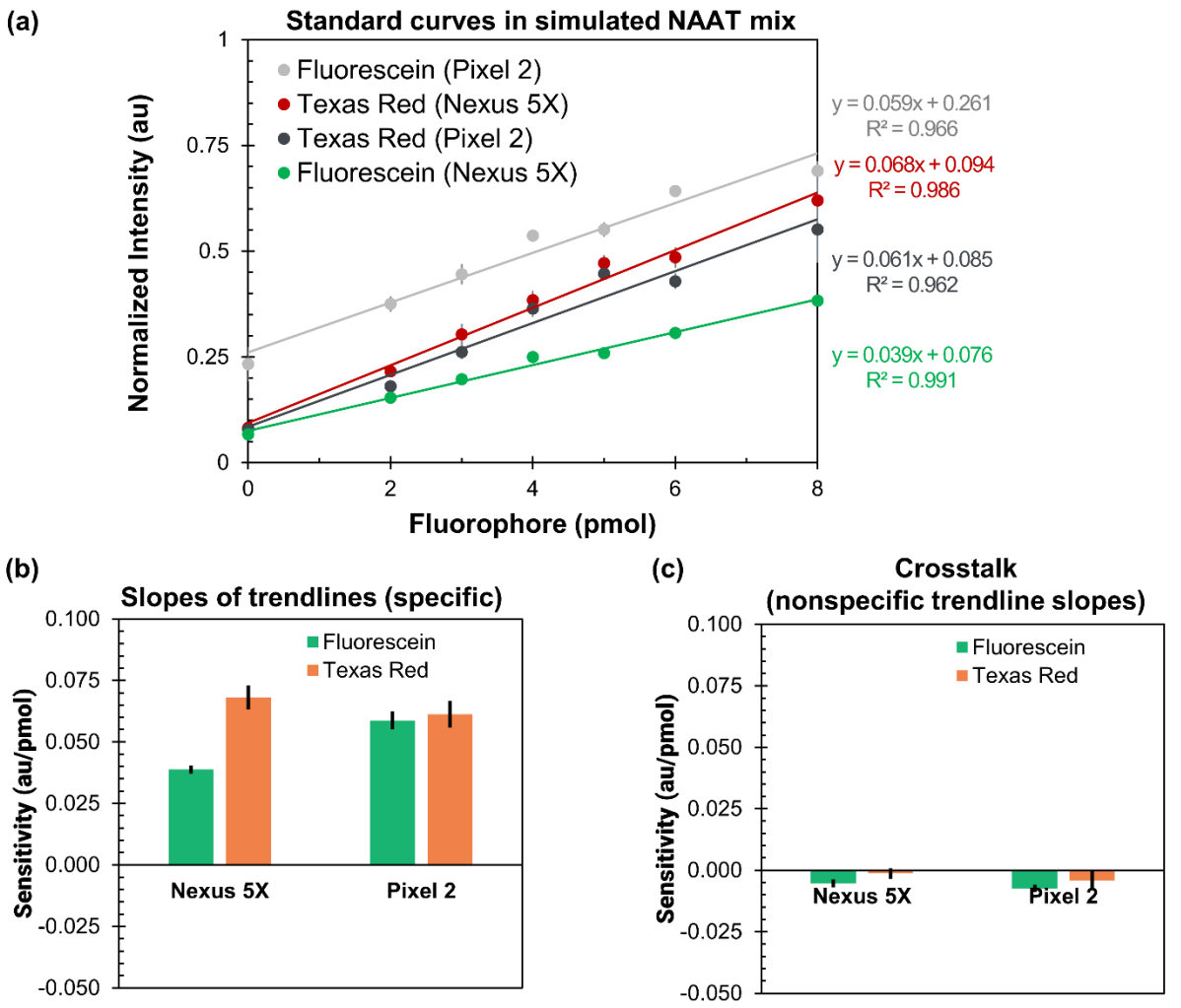

Figure 6.4: Standard curves of glass fiber pads containing fluorescein or Texas Red imaged by the mobile phone fluorescence reader. (**a**) The standard curves for both fluorophores increase linearly with concentration. (**b**) The slope of standard curves (from panel a) in the specific color channels (red channel for Texas Red and green channel for fluorescein) are substantially greater than zero. (**c**) The slopes of the trendlines from the nonspecific color channels (green for Texas Red and red for fluorescein) show near-zero slopes. Pads were saturated with mock nucleic acid amplification mixtures that mimic the pH, salt, and viscosity of iSDA and imaged at iSDA temperatures. Both phones were similarly sensitive to fluorescein and Texas Red (as indicated by the slope of the linear regression, $p>0.7$). Limits of detection for both fluorophores are lower than the nominal fluorescent probe amounts (4.0 pmol) in each iSDA reaction (Nexus 5X: 1.2 pmol (Texas Red) and 0.64 pmol (fluorescein) and Pixel 2: 1.7 pmol (Texas Red) and 3.7 pmol (fluorescein)). Points indicate mean and standard error of the mean (n=4).

6.4.2 Characterizing and overcoming evaporation artifact

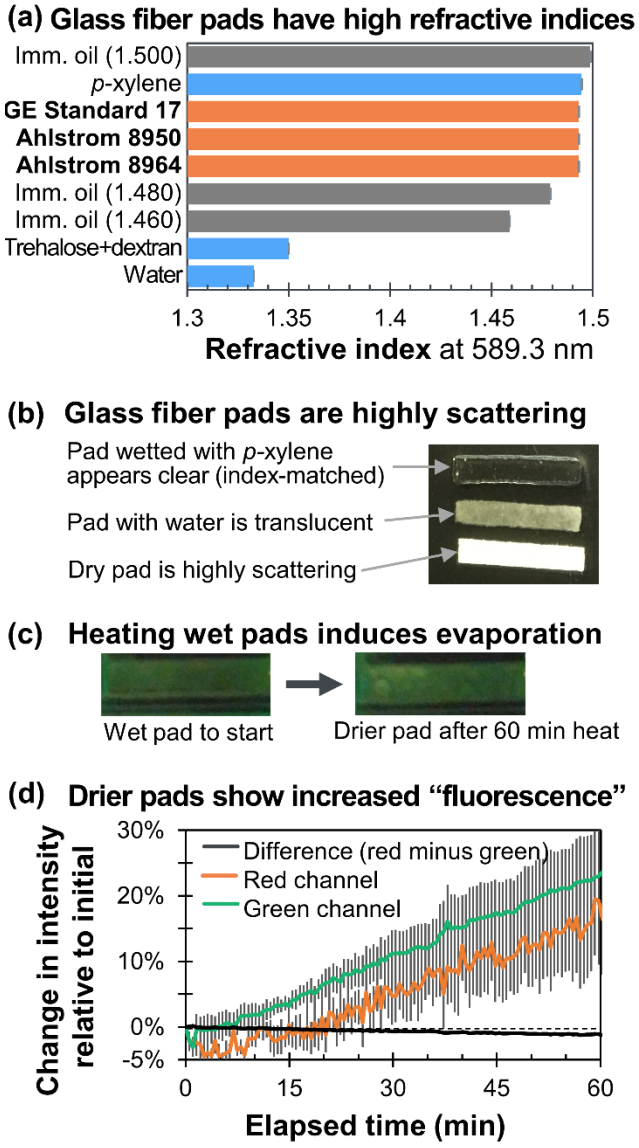

Figure 6.5: Imaging fluorophores in high surface area, optically scattering substrates such as paper requires overcoming a light scattering artifact driven by evaporation. (**a**) The measured refractive indices of the fibers of several glass fiber materials (orange bars) was about 1.4931, which was greater than that of water (1.33285) or simulated NAAT master mix (trehalose+dextran, 1.35019). The gray bars indicate reference immersion (imm.) oil controls. Bars indicate mean and error bars show 95% confidence intervals. (**b**) A glass fiber pad blocked with bovine serum albumin that was wetted with index-matching *p*-xylene appeared transparent, while a pad wetted with water was translucent and a dry pad scattered light and appeared white. (**c**) Glass fiber pads blocked with bovine serum albumin that was wetted with water showed evaporation and condensation after 60 minutes of heating when imaged with the two-fluorophore mobile phone reader. (**d**) Quantifying the heated pads' fluorescence intensity showed that the red and green color channel intensities increased inconsistently as the pads were heated, but the difference of the two color channels consistently decreased by only 1%. Lines show mean and standard error of the mean (n=4 pads).

We then characterized the effect of evaporation on imaging. First, we measured the refractive index of the glass fiber substrate which supports nucleic acid amplification. **Figure 6.5a** shows that the refractive index of GE Standard 17 was 1.49308±0.00003 (mean and 95% confidence interval) at 589.3 nm, which is similar to that of other glass fiber materials and *p*-xylene (1.49444±0.00004), but

substantially higher than the refractive index of water (1.33285±0.00000). **Figure 6.5b** shows that a BSA-blocked glass fiber pad wetted with an index-matching liquid such as *p*-xylene is nearly transparent, whereas a pad wetted with water is translucent and a dry pad appears uniformly white.

Next, we measured the fluorescence intensities of wetted glass fiber pads during a simulated NAAT. Glass fiber pads that had been filled with mock NAAT master mixes without any fluorophores were heated for one hour in the proposed device and imaged with the mobile phone reader in real time (**Figure 6.5c**, **Figure 6.5d**). The observed intensities at 45 minutes increased irreproducibly by 11±6% (mean and standard error of the mean) in the red channel and 17±5% in the green channel relative to the initial level. In contrast, the difference of the red and green color channels (based on **Equation 6.1**) decreased by 0.92±0.18% relative to the initial level, which was significantly below the threshold for positive (0.02 units, $p<0.001$ at all times, left-tailed one-sample t-test) and above the threshold for negative (-0.02 units, $p<0.01$ at times at or below 45 minutes, right-tailed one-sample t-test). In other words, the differential fluorescence signal was within the range corresponding to no amplification for amplification times up to 45 minutes.

6.4.3 Application to real-time NAATs

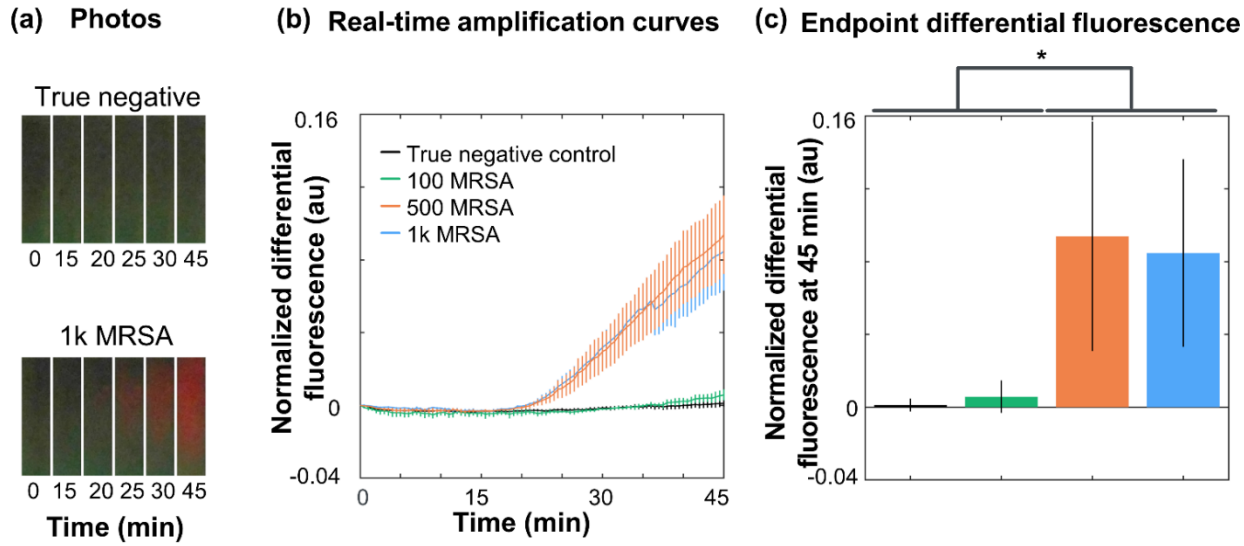

Figure 6.6: Imaging singleplexed amplification reactions in the MD NAAT in real time with the Nexus 5X phone. Glass fiber pads containing lyophilized isothermal strand displacement amplification reagents (with a red-emitting fluorescent probe for *mecA*) were rehydrated with samples containing MRSA genomic DNA or water. Pads were heated in the MD NAAT for 45 minutes and imaged about every 30 seconds with a Nexus 5X equipped with multipass excitation and emission filters for fluorescein and Texas Red. (**a**) Photos of amplifying pads show substantial red fluorescence in a MRSA-containing pad. (**b**) Real-time curves show the average differential fluorescence intensity across each pad (red color channel minus green channel) over time. The curves show rapid amplification of 500 and 1000 copies of MRSA. Lines show mean and standard error of the mean (n=3). (**c**) The endpoint differential fluorescence at 45 minutes is significantly higher in pads containing at least 500 copies of MRSA than in the negative control (* $p<0.001$, one-way ANOVA). Bars show mean and error bars show 95% confidence intervals.

Finally, we applied these insights to image isothermal strand displacement amplification (iSDA) reactions in the MD NAAT platform in real time with two phones. We ran both singleplexed and biplexed reactions targeting different genes in methicillin-resistant *S. aureus* (**Figure 6.6** and **Figure 6.7**). We prepared mixtures of MRSA genomic DNA (gDNA) and/or internal amplification control (IAC) DNA in buffer, rehydrated glass fiber pads containing lyophilized iSDA reagents, heated the

pads in the MD NAAT platform, and imaged with a phone equipped with multipass excitation and emission filters every 30 seconds. Both experiments were quantitatively analyzed by considering the normalized differential fluorescence as defined in **Equation 6.1**; Figure 4b indicates how to interpret these data.

First, we imaged (with a Nexus 5X phone) singleplexed iSDA reactions labeled with a red-emitting fluorescence probe specific to the *mecA* gene. Images of pads (**Figure 6.6a**) and real-time curves (of the differential fluorescence as defined in **Equation 6.1**, **Figure 6.6b**) during amplification consistently showed no fluorescence, while pads containing at least 500 copies of MRSA gDNA showed substantial red fluorescence from about 20 minutes onward. **Figure 6.6c** shows that the endpoint differential fluorescence for pads containing at least 500 copies of MRSA gDNA was significantly greater than the true negative control ($p<0.001$, one-way ANOVA, n=3 for positives and n=9 for true negatives).

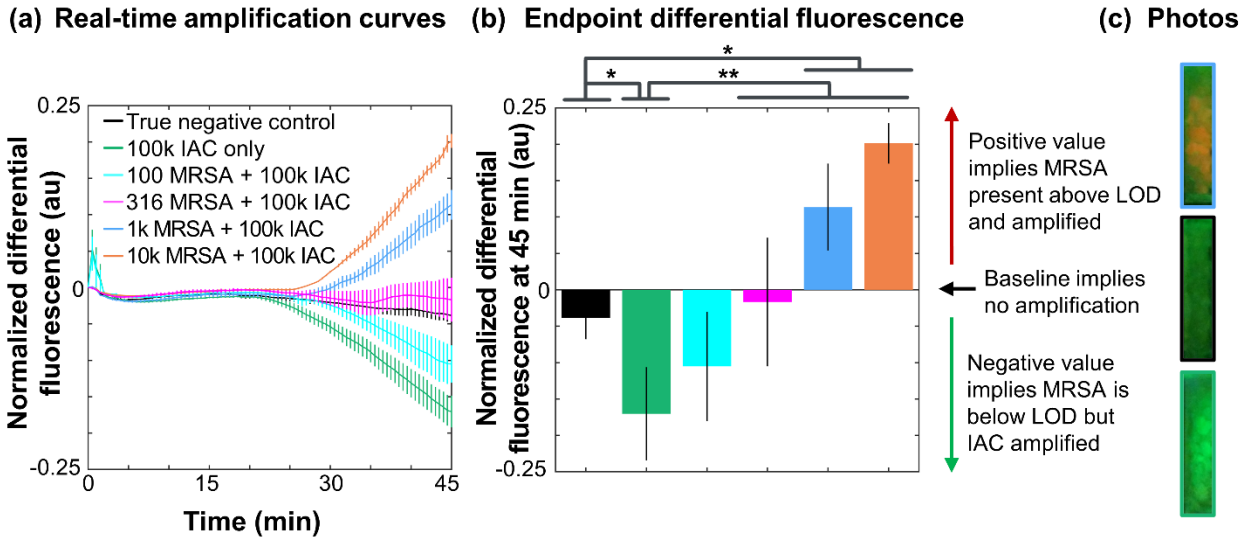

Figure 6.7: Imaging biplexed isothermal strand displacement amplification reactions performed in the MD NAAT platform with a Pixel 2 phone demonstrates the utility of the differential fluorescence imaging strategy. Glass fiber pads containing lyophilized reagents for isothermal strand displacement amplification were labeled with fluorescein (internal amplification control (IAC)) and a Texas Red (MRSA) analog. (**a**) Pads rehydrated with mixtures of MRSA genomic DNA and internal amplification control (IAC) DNA show rapid amplification with liftoff near 30 minutes. Biplexed samples containing methicillin-resistant *S. aureus* (MRSA) genomic DNA and internal amplification control (IAC) DNA show positive signals (*i.e.* more amplification in the MRSA-specific red channel than IAC-specific green channel), while samples containing only IAC show negative signals (*i.e.* more signal in the green channel than red). Truly negative samples with neither MRSA nor IAC DNA do not amplify (near-zero signals). Curves show mean and error bars show standard error of the mean (n=3). (**b**) The differential fluorescence at 45 minutes shows significant differences between the true negative control and the IAC only case (*$p<0.01$, one-way ANOVA), the true negative and samples containing at least 1k copies of MRSA (*$p<0.01$, one-way ANOVA), and the IAC only case and samples containing at least 316 copies of MRSA (**$p<0.003$, one-way ANOVA). Bars show mean and error bars show 95% confidence intervals. (**c**) Photos of pads at 45 minutes show substantial red fluorescence in pads containing 1k copies of MRSA gDNA and 100k copies of IAC DNA, while pads containing only IAC show substantial green fluorescence and pads containing neither do not fluoresce appreciably.

We then imaged (with a Pixel 2 phone) biplexed iSDA reactions labeled with a red-emitting probe specific to the *ldh1* gene and a green-emitting probe specific to the IAC amplicons. We observed that the real-time amplification curves showed liftoff times of about 30 minutes (**Figure 6.7a**). Pads

containing high levels of MRSA gDNA showed positive differential fluorescence signals, whereas pads containing only IAC or 100 copies of MRSA gDNA showed negative differential fluorescence signals. **Figure 6.7b** shows that biplexed reactions containing at least 1000 copies of MRSA gDNA showed significantly higher endpoint differential fluorescence than the true negative control ($p<0.01$, one-way ANOVA), while pads containing only IAC (*i.e.* MRSA-negative pads) showed lower endpoint differential fluorescence than either the true negative control ($p<0.01$, one-way ANOVA) or pads containing at least 316 copies of MRSA gDNA ($p<0.003$, one-way ANOVA). In other words, pads containing only IAC had lower (more negative) levels of differential fluorescence whereas pads containing high levels of MRSA had higher (more positive) differential fluorescence levels, which matched the trends in pad photos (**Figure 6.7**).

6.5 Discussion

Laboratory nucleic acid amplification tests are sensitive, specific, and rapid assays that combine exponential amplification, template-specific real-time fluorescence detection, and multiplexing (*e.g.* with onboard positive controls). For example, the GeneXpert provides results in about 66 minutes (for *S. aureus*),[114] detects up to six fluorophores, and includes onboard lysis and amplification controls. Recent attempts to translate NAATs beyond the laboratory have led to several competing platforms that only implement a subset of these features.[79,97,99] In this aim, we describe a generalizable mobile phone imaging strategy that images two colocalized fluorophores simultaneously, which enables real-time fluorescence detection in biplexed NAATs. We applied the strategy to image a point-of-care, paper-based NAAT on our lab's MD NAAT platform.

Imaging fluorophore-labeled NAATs in porous media (*e.g.* the glass fiber pads used herein) is especially challenging because the substrates introduce optical artifacts due to their heterogeneity, light scattering, and autofluorescence.[86] Beyond these drawbacks which are already documented in the literature, we also observed highly variable optical artifacts such as drift in the fluorescence intensities of heated glass fiber pads. We hypothesize that this artifact was due to evaporation and condensation of liquid on the cover as suggested by the liquid droplets in the heated pad photo in **Figure 6.5c**. Evaporation was likely exacerbated by the pads' high surface area (45 mm^2) and elevated temperature during heating (*e.g.* 50 °C for 45 minutes during iSDA). The artifact was not due to a temperature-dependent change in the fluorophore quantum yield during amplification because the artifact was observed even when fluorophores were not present (*e.g.* in **Figure 6.5c** and **Figure 6.5d**). We attribute the rise in fluorescence intensity to increased light scattering as the glass fiber pads dried, as shown in **Figure 6.5b**.

We suggest that differential fluorescence measurements are one strategy to overcome the artifacts imposed by the paper substrate's autofluorescence, light scattering, and saturation-dependent drift in fluorescence intensity. Typically, differential measurements reduce drift when noise contributors appear about equally in multiple channels, such as in radar or spectroscopy. In our case, both the red and green color channels of mobile phone photos contained artifacts introduced by evaporation and paper autofluorescence. Analyzing the difference of the red and green color channels eliminated the impact of these factors as suggested by **Figure 6.5d**. We demonstrated the usefulness of this approach on phones with completely different camera spectral sensitivities (**Figure 6.4**, **Figure 6.6**, and **Figure 6.7**), which suggests the generalizability of the proposed differential fluorescence measurement strategy.

One concern when imaging multiple fluorophores is crosstalk between ostensibly orthogonal detection channels. Although we observed minimal detection of Texas Red in the green color

channel, we observed that the red color channel fluorescence was slightly negatively correlated with fluorescein concentration. The practical consequence of this is potentially lower sensitivity toward the target labeled with Texas Red, or MRSA in our case. However, we observed exquisite sensitivity toward red fluorophore-labeled MRSA (316 copies even in biplexed reactions in which IAC was present at 100k copies (**Figure 6.7**). Further improvements to sensitivity may be possible with algorithmic improvements such as principle component analysis.

The imaging scheme described in this aim improves on alternatives described in the literature. Our group recently described a strategy to image fluorophores with multiple mobile phone models without any optical filters in paper-based immunoassays, but the particular scheme was compatible only with long Stokes shift fluorophores such as quantum dots.[111] The Krull group described a tablet-based imager that used Forster resonance energy transfer (FRET) to visualize nucleic acid hybridization in paper, but the assay was an endpoint assay that did not monitor real-time amplification. Priye et al. recently developed a multiplexed mobile-phone imager to image fluorescence NAATs in nonscattering media such as tubes. Although the imager included an onboard multipass excitation filter and LED, the system could not detect multiple fluorophores at the same time because each fluorophore required distinct emission filters, which may render the system impractical for real-time imaging in scattering media.[58,126]

To our knowledge, this aim describes the first mobile phone camera sensor-agnostic imaging strategy that visualizes, in real time, biplexed NAATs performed in highly scattering media such as paper. Differential fluorescence imaging with phones may enable translating sensitive laboratory fluorescence assays to the point of care.

6.6 Conclusions

This aim describes a mobile phone imaging strategy that simultaneously images two colocalized fluorophores. To our knowledge, this is the first solid-state mobile phone reader that images two fluorophores simultaneously. It enables highly sensitive detection of fluorophore-labeled nucleic acids even in highly scattering porous media. This work also identified heating-induced changes in membrane saturation that adversely affects fluorescence assays by introducing drift. The differential fluorescence analysis process pioneered in this aim is a substantial step to eliminate this artifact. Finally, these techniques were demonstrated with multiple phone models with different camera spectral sensitivities, which suggests that the methods developed in this aim are generalizable to other assays.

7 Near-digital amplification in paper improves sensitivity and speed in biplexed reactions

"*Veritatem dies aperit.*"

Time discloses the truth.

– Seneca, *De ira* (On Anger), *c.* 45. From: Seneca the Younger, *De ira.* p. 214-215. Loeb Classical Library, Harvard University. DOI: 10.4159/DLCL.seneca_younger-de_ira.1928

7.1 Summary

7.1.1 Abstract

The simplest point-of-care assays are usually paper and plastic devices that detect proteins or nucleic acids at low cost and minimal user steps, albeit with poor limits of detection. Digital assays improve limits of detection and analyte quantification by splitting a sample across many wells (or droplets), preventing diffusion, and performing analyte amplification and detection in multiple small wells. However, truly digital NAATs require costly consumable cartridges that are precisely manufactured, aligned, and operated to enable low detection limits. In this section, we demonstrate how to implement near-digital NAATs in low-cost porous media while approaching the low limits of detection of digital assays. The near-digital NAAT was enabled by a paper membrane containing lyophilized amplification reagents that automatically, passively meters and distributes a sample over a wide area. Performing a NAAT in the paper membrane while allowing diffusion captures many of the benefits of digital NAATs if the pad is imaged at a high spatial resolution during amplification. We show that the near-digital NAAT is compatible with a low-cost paper and plastic disposable cartridge coupled to a 2-layer rigid printed circuit board heater (the MD NAAT platform). We also demonstrate compatibility with biplexing and imaging with mobile phones with different camera sensors. Limits of detection for biplexed reactions were 316 copies of methicillin-resistant *Staphylococcus aureus* genomic DNA in 20.5 minutes of amplification time despite the presence of 10^5 copies of co-amplifying internal amplification control DNA. These results suggest that near-digital NAATs in paper improve the sensitivity and speed, even in biplexed reactions.

7.1.2 Academic contributions

This aim will be submitted to a peer-reviewed journal in collaboration with members of the Yager group, including Sujatha Kumar, Vidhi Singh, and Paul Yager.

7.2 Introduction

Nucleic acid amplification tests are part of a popular strategy to detect infectious diseases rapidly and reliably, often in integrated sample-to-result systems at the point of care.[79,97,99,115,117] Commercial NAATs intended for these point-of-care clinical settings usually enzymatically amplify pathogen-specific nucleic acids and detect amplification products with target-specific fluorescent probes.[9,11,96,106,114] These assays discriminate between the absence of target and assay failure by including onboard positive controls, often in the form of co-amplifying, heterologous internal amplification control (IAC) DNA, detected with specific probes in an orthogonal fluorescence

channel (**Figure 7.1a**).[9,11,96,114] The combination of enzymatic amplification and multichannel fluorescence detection enable low limits of detection, rapid time to result (15 minutes on the semiautomated Alere *i* platform or 60-90 minutes on the automated Cepheid GeneXpert), and high specificity.[9,11,96,114,127,128]

Recent efforts to improve NAATs include many digital amplification schemes that purport to enable accurate analyte quantification, reduce limits of detection, or lower time to result.[83,113,129–135] Typical digital NAATs use isolated nanoliter or femtoliter-scale wells or droplets to optically segment a sample into individual reaction "chambers" that contain one or zero copies of the template of interest (**Figure 7.1b**).[130,133] As amplification proceeds, each chamber provides a yes/no output as to whether template was present therein, and aggregating results from all chambers enables quantification under Poisson statistics. However, truly digital NAATs require costly, precisely manufactured cartridges[83,113,129] (for assays that amplify in wells of semi-uniform volume) or complex fluidics[133–135] (for assays based on droplets or oil/water phase separation) to prevent diffusion between neighboring amplification chambers, which is challenging to translate to the point of care.

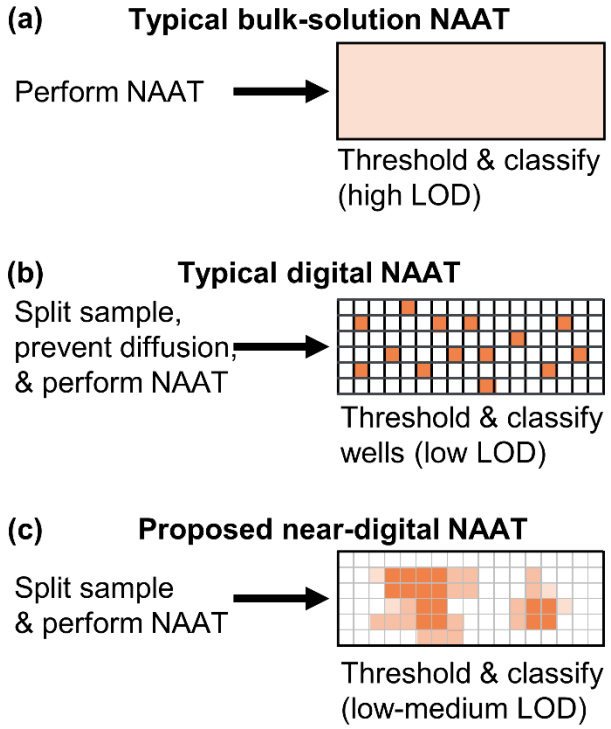

Figure 7.1: Motivation for almost-digital amplification in paper. (**a**) Typical nucleic acid amplification tests (NAATs) performed in bulk solutions have poor limits of detection (LOD) due to low spatial resolution and low initial nucleic acid concentration across the amplification zone. (**b**) Digital NAATs split the reaction mixture into multiple small wells or droplets, nominally preventing diffusion during amplification to improve limits of detection and assay time. (**c**) The near-digital NAAT initially distributes a reaction mixture across a wide area but allows diffusion during amplification, which leverages the benefits of digital NAATs without requiring complex cartridge design.

Several research groups seek to reduce the complexity of digital NAATs by simplifying the underlying assumptions and required hardware. One promising approach is to perform a digital NAAT in polydisperse droplets of varying volumes, imaging the droplets with high spatial or temporal resolution, and leveraging complex statistical corrections to compensate for the variation in

the sampled droplet volume.[134,135] Another droplet-based strategy is to simplify the optics by imaging droplets one-at-a-time in a format akin to flow cytometry.[136] Digital NAAT cartridges may also be simplified by laser cutting SlipChip-style wells in acrylic.[129] However, these approaches to date have been unsuitable to translate to the home because they require bulky/costly supporting hardware (lasers or motorized stages) or difficult to manufacture components at the nanoliter scale. In contrast, extant home assays are performed in porous media (*i.e.* paper microfluidics) that passively meter fluids at the microliter scale and require no complex hardware or user steps.[4,21]

Lateral flow immunoassays (*e.g.* pregnancy, ovulation, or HIV) are the most common paper-based assay used in the home. These assays sacrifice limits of detection for ease of use and low cost, which render them unsuitable for sensitive detection of infectious disease biomarkers.[4,21] One strategy to improve sensitivity is to perform NAATs in paper.[3,17,79,97,112] However, existing paper-based NAATs often lack co-amplifying positive controls and suffer from slow time to result (*e.g.* endpoint assays with 30-60 minutes of amplification time).[3,17,79,97,112] We propose to overcome these limitations by leveraging insights from digital NAATs and translating them into paper microfluidic assays. Specifically, we note that if the size of the area in which nucleic acid amplification occurs is large compared to the diffusivity of the amplification products, then it is not possible for amplification in one region to affect the concentration of amplification products in a distant region provided that the bulk fluid is not moving. In other words, the nucleic acid amplification reaction is confined to "virtual wells," the sizes of which increase with time (based on diffusion).

The near-digital NAAT in paper leverages wicking in porous media to automatically distribute a sample over a wide surface area pad that contains lyophilized isothermal NAAT reagents. A mobile phone images the entire pad during amplification at a high spatial resolution in real time. Individual pixels of acquired images are binned into partitions to improve signal-to-noise ratios relative to reactions performed in bulk media (**Figure 7.1c**). The usefulness of this approach was demonstrated with an isothermal NAAT for methicillin-resistant *Staphylococcus aureus* performed on the portable, USB-powered NAAT platform described in Aim 3 (Chapter 5). The near-digital NAAT described in this aim is a step toward enabling rapid detection of amplifying nucleic acids in point-of-care settings, including the home.

7.3 Methods

7.3.1 Overview of near-digital NAAT

Real-time nucleic acid amplification tests usually detect amplification products optically, often with sequence-specific fluorescent probes. For a NAAT performed in a bulk solution, all components of the reaction (*e.g.* templates; NAAT reagents such as primers, enzymes, and nucleotides; and products) are free to equilibrate throughout the reaction volume through diffusion and convection. Diffusion kinetics are governed by Fick's Second Law, shown in **Equation 7.1**:

Equation 7.1:
$$\frac{\partial C}{\partial t} = D\frac{\partial^2 C}{\partial x^2}$$

where C in the concentration, D is the diffusion coefficient, t is time, and x is distance. The diffusion coefficient is a function of several variables such as particle size (based on the Stokes-Einstein equation for spherical particles) and ionic charge (Einstein-Nernst relation), which renders it difficult to accurately predict the diffusion coefficient of all species in a NAAT reaction. Moreover, in porous media, the diffusion coefficient is further modified to compensate for

partitioning (K) and hydrodynamic drag (ω_r) as in **Equation 7.2**, where α is the hydrodynamic radius and r is the pore radius:[97,137]

Equation 7.2: $$D_m = DK\omega_r = D\left[1-\frac{\alpha}{r}\right]^2\left[1-2.1\frac{\alpha}{r}+2.09\left(\frac{\alpha}{r}\right)^3-0.95\left(\frac{\alpha}{r}\right)^5\right]$$

Equation 7.2 indicates that the diffusion coefficient of most of the components of the amplification reaction in porous media should be lower than in bulk solutions since both the partition coefficient and hydrodynamic drag terms are lower than one (because the pore radius (r) is almost always greater than the hydrodynamic radius of most species (α)).[97,137] This implies that NAATs performed in porous media should experience slower diffusion than assays performed in wells or droplets.

7.3.2 Performing the near-digital NAAT

Typical NAAT runs were performed following the procedures outlined in the previous two aims.[79,106] Briefly, glass fiber membranes (GE Standard 17) were cut, blocked, filled with all reagents (including enzymes and primers) for isothermal strand displacement amplification (iSDA), flash frozen with liquid nitrogen, lyophilized for at least two hours, and stored in heat-sealed aluminized Mylar pouches at room temperature until use.

The baseline (1×) iSDA chemistry consisted of: inorganic potassium phosphate buffer (pH 7.6, 50 mM), magnesium sulfate (3.75 mM), an equimolar mix of deoxynucleotides [dATP, dCTP, dGTP, dTTP] (0.2 mM), trehalose (0.27 M), 500 kD dextran (4.8% (w/v)), DNA primers (500 nM forward, 250 nM reverse, 50 mM of each bumper primers), target-specific fluorescent probes (minor groove binders from ELITechGroup) labeled with a Texas Red analog (AquaPhluor-593, 200 nM), internal amplification control-specific probes labeled with 6-FAM (200 nM), Bst 2.0 Warmstart DNA polymerase (New England BioLabs, 200 U/μL), Nt.BbvC1 nicking enzyme (New England BioLabs, 1.6% (v/v)), and nuclease-free water (1.23 μL).

As before, the pads were rehydrated with a 20 μL mixture of methicillin-resistant *Staphylococcus aureus* (MRSA) strain FPR3757 genomic DNA (ATCC BAA-1556DQ) and 10^5 copies of internal amplification control (IAC) single-stranded DNA (sequences in Lafleur *et al.*)[79] in nuclease-free water. The pads were placed in laser-cut polymethylmethacrylate cartridges, which was adhered to the printed circuit board of the USB-powered MD NAAT device described in Aim 3 (Chapter 5) using thermally conductive tape (3M 8815). The pads were heated to iSDA-relevant temperatures (50 °C) by the MD NAAT for 45 minutes. The mobile phone fluorescence reader (Nexus 5X or Pixel 2 equipped with multipass excitation and emission filters) detailed in Aim 4 (Chapter 6) was placed about 15 cm above the MD NAAT and imaged the pads every 30 seconds using the Camera FV-5 application.

7.3.3 Optically segmenting mobile phone images

Mobile phone images were preprocessed by gamma correcting, rotating, and cropping them to the region corresponding to each pad. Each glass fiber amplification pad corresponded to about 5×10^4 to 10^5 pixels on the phones used. The differential fluorescence intensity (difference of red and green color channels) was calculated at each pixel based on **Equation 6.1**. The pads were segmented into blocks by grouping neighboring pixels such that each pad contained 1, 4, 10, 100, 1000, 10^4, or the maximum possible number of blocks (*i.e.* the number of pixels in the region of interest). The nominal block dimensions are shown in **Table 7.1**. The average differential fluorescence intensity

was then calculated for each block, and each pad's intensity was defined as the average of the top decile of intra-block intensities (*i.e.* the average of the 10% highest blocks, which is an approach for truly digital NAATs identified by Rolando *et al.* as balancing the competing needs to maximize sensitivity and minimize false positives[132]). All analysis was performed in MATLAB R2019a.

Table 7.1: Nominal block parameters in optically segmented mobile phone images

Number of blocks	Blocks in a 3×15 mm pad	Block dimensions* (μm)	Area per block	Nominal block volume* for a 20 μL reaction
1	1×1	3000×15000	45 mm^2	20 μL
4	1×4	3000×3750	11.3 mm^2	5 μL
10	2×5	1500×3000	4.5 mm^2	2 μL
100	4×25	750×600	0.45 mm^2	200 nL
1,000	20×50	150×300	45,000 μm^2	20 nL
10,000	40×250	75×60	4,500 μm^2	2 nL
100,000	200×500	15×30	450 μm^2	200 fL

*The nominal block volumes are based on distributing a 20 μL sample volume across the number of blocks in the first column. This calculation does not make any assumptions about the thickness of the amplification zone, which is affected not only by the thickness of the porous media used, but also by the volume of the amplification reagents and surface effects (*e.g.* contact angle).

7.3.4 Validating near-digital NAAT

7.3.4.i Assess improvement of signal to noise ratios

First, we validated whether optical segmentation improved signal to noise ratios in the near-digital NAAT. Glass fiber pads containing lyophilized iSDA reagents for the MRSA *mecA* gene were rehydrated with biplexed mixtures of MRSA genomic DNA and IAC DNA, heated in the MD NAAT, and imaged with the Nexus 5X fluorescence reader. The images were analyzed as in the previous paragraph (section 7.3.3). A one-way analysis of variance (ANOVA) was used to assess whether the endpoint differential fluorescence at 45 minutes was significantly different between MRSA-positive pads containing 1000 copies of MRSA genomic DNA mixed with 10^5 copies of IAC DNA and MRSA-negative pads containing 10^5 copies of IAC DNA.

7.3.4.ii Characterize impact of diffusion

Next, we assessed the impact of diffusion in the near-digital NAAT. We rehydrated lyophilized iSDA reagents (which contained red-emitting fluorescent probes specific to the MRSA *mecA* gene) with 10^6 copies of a synthetic, single-stranded DNA (ssDNA) oligomer containing the *mecA* gene. The pads were heated in the MD NAAT (to 50 °C) and imaged with the mobile phone fluorescence reader with a Nexus 5X or Pixel 2 phone about every 30 seconds (n=4 pads total). Positive and negative controls were simultaneously heated for 45 minutes in a heat block set to 50 °C and imaged with the phone reader at the endpoint verify that contamination did not occur.

Images of the MD NAAT runs were analyzed with a computer vision algorithm that quantified propagation of the amplification front. The red channel of acquired images was binarized by thresholding, and the *regionprops()* function was used to calculate the equivalent diameter of a circle with the same area as the region above the threshold. These diameters were compared to the

expected propagation of the amplification front based on diffusion in porous media, *i.e.* the one-dimensional, semi-infinite solution to **Equation 7.1**, whereby the position of the propagation front is proportional to the square root of the modified diffusion coefficient and elapsed time.

7.3.5 Optimizing near-digital NAAT.

Next, we optimized the near-digital NAAT chemistry to maximize signal-to-noise ratios in biplexed isothermal strand displacement amplification reactions. NAAT chemistry optimization was guided by fractional factorial experiment design principles by varying the concentration of the 5 reagents that were previously implicated in affecting iSDA time to result in tube reactions. In the first experiment, 18 master mixes were prepared by varying the nicking enzyme (0.5×, 1×, 1.5×), polymerase (1×, 1.5×, 2×), and primers (1×, 1.5×) concentrations. The master mixes were lyophilized onto blocked glass fiber pads as above. A custom pad holder was engineered from 3 mm-thick clear PMMA by mimicking the shape of a standard 384-well plate and having laser-etched regions for each lyophilized pad such that each 3×15 mm pad aligned with 4 wells of a well plate. Each pad holder region was treated with dichloromethane (23 μL, corresponding to 0.5 μL/mm^2) and the bottom of the PMMA tray was covered with black LDPE secured by minimally fluorescent PDMS tape. Lyophilized pads were placed on the custom PMMA tray and were reconstituted with 1000 copies of genomic DNA purified from MRSA genomic DNA mixed with 10^5 copies of single-stranded IAC DNA in 20 μL of nuclease-free water. The tray was placed in a preheated plate reader (Molecular Devices) set to 50.5 °C, configured to read a 384-well plate, and imaged in fluorescence kinetic mode (excitation: 593 nm, emission: 650 nm, 1 s integration time, about 5 minutes to read the entire plate) over about 1 hour. In the second experiment, 18 master mixes were evaluated by testing three of the optimal master mixes identified from the first experiment at a range of concentrations of dNTPs (1×, 1.5×, 2×) and magnesium sulfate (1×, 1.5×) (procedure identical to the first experiment). Both experiments were run with triplicate pads at each condition along with a set of positive and negative controls (*i.e. sans* MRSA DNA) rehydrating the baseline (1×) master mix.

Finally, the near-digital NAAT was run at the optimized reagent concentrations identified in the previous two experiments. Lyophilized pads containing iSDA reagents were rehydrated with a dilution series of mixtures of MRSA genomic DNA and IAC ssDNA, heated in the MD NAAT for 45 minutes, and imaged with a Nexus 5X mobile phone fluorescence reader for 45 minutes (n=3). Images were analyzed with and without the near-digital optical segmenting scheme outlined previously. The time to threshold (set at 0.02 a.u. for MRSA-positive reactions and -0.02 a.u. for MRSA-negative reactions) was quantified for both the segmented and unsegmented cases. A one-sample, parametric *t*-test assessed whether there was a significant difference in the time to result.

7.4 Results

7.4.1 Validating near-digital NAAT

7.4.1.i Assess improvement of signal-to-noise ratios

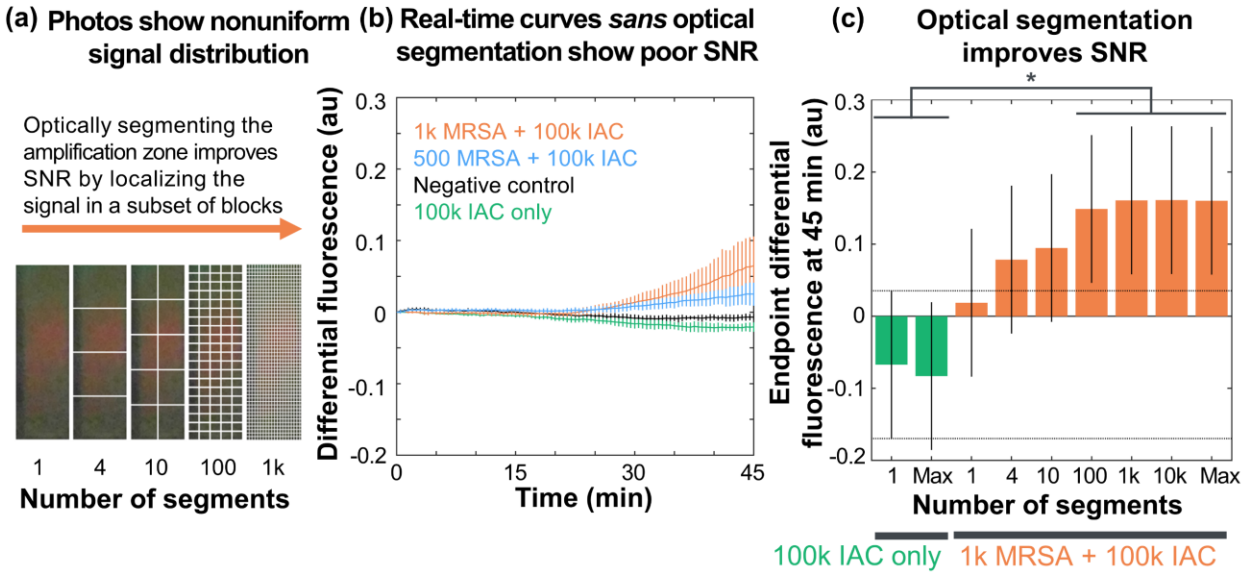

Figure 7.2: Optical segmentation improves signal-to-noise ratios of nucleic acid amplification in porous media. (**a**) A photo (with differing densities of overlaid lines) of a biplexed amplification reaction containing MRSA DNA and internal amplification control (IAC) DNA shows a highly nonuniform signal distribution after 30 minutes of amplification. Optically segmenting the pad and analyzing a subset of blocks isolates the signal of interest, improving signal-to-noise ratios. (**b**) Real-time curves for biplexed isothermal strand displacement amplification reactions imaged with a mobile phone fluorescence reader show slow liftoff times and poor signal-to-noise ratios in unsegmented pads. Curves show mean and error bars show standard error of the mean (n=5). (**c**) Plotting the endpoint signal intensities for the IAC only and MRSA-positive biplexed reactions shows a significant improvement in signal-to-noise ratios. The endpoint differential fluorescence was significantly greater in MRSA-positive pads optically segmented into at least 100 blocks than the IAC only pads ($p<0.05$, one-way ANOVA). The y-axes in both panels b and c show the differential fluorescence intensity as defined in Equation 6.1.

First, we assessed whether near-digital nucleic acid amplification in glass fiber membranes (with optical segmentation) improved signal-to-noise ratios compared to unsegmented reactions. Mixtures of MRSA genomic DNA and IAC DNA were diluted in buffer, amplified by isothermal strand displacement amplification (iSDA) in the MD NAAT device, and imaged every 30 seconds by a Nexus 5X. **Figure 7.2a** shows that images of a biplexed reaction containing 1000 copies of MRSA mixed with IAC DNA show nonuniformly distributed red, MRSA-specific fluorescence near the center of the pad after 30 minutes of amplification. The pad also showed substantial green fluorescence near the edges of the pad. Increasing the number of segments into which the image was divided isolated the red fluorescence of interest into a subset of blocks.

Next, we quantitatively analyzed the images from this experiment, but without optical segmentation. The real-time curves in **Figure 7.2b** show that data from pads as a whole (*sans* optical segmentation) have low signal-to-noise ratios, even after 45 minutes of amplification (n=5). The negative controls were indeed negative: Pads containing neither MRSA nor IAC DNA were in the range corresponding to no amplification (*i.e.* above the threshold for MRSA-negative ($p<0.01$, right-tailed

one-sample t-test) and below the threshold for MRSA-positive ($p<0.001$, left-tailed one-sample t-test)) at all times. However, without optical segmentation, pads containing only IAC DNA or both MRSA and IAC DNA did not significantly exceed the threshold for negative or positive, respectively ($p>0.05$, one-sample t-test).

Finally, the images from this experiment were analyzed with the near-digital optical segmentation scheme. **Figure 7.2c** demonstrates that increasing the number of blocks (to 100) into which each pad was optically segmented improved signal-to-noise ratios: pads containing 1k copies of MRSA (with 100k copies of IAC) significantly exceeded the threshold for positive ($p<0.05$, one-sample t-test) and were significantly greater than the IAC only group ($p<0.05$, one-way ANOVA). However, increasing the spatial resolution beyond 100 blocks (*i.e.* decreasing the block size below 750×600 μm) did not significantly improve endpoint signal-to-noise ratios. There was no significant difference in endpoint fluorescence intensities for unsegmented pads ($p>0.05$, one-way ANOVA).

7.4.1.ii Characterize impact of diffusion

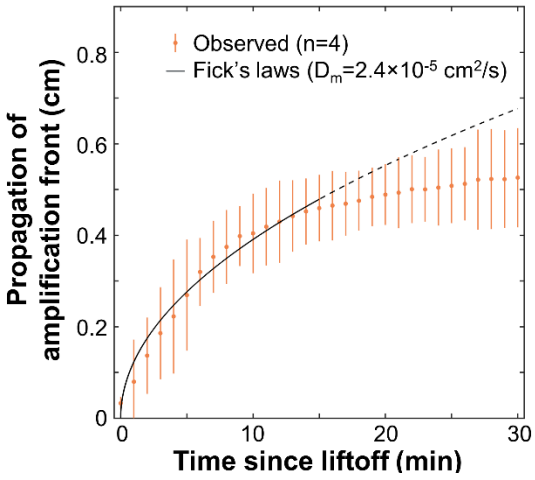

Figure 7.3: Propagation of amplification front follows Fick's laws immediately after liftoff. Glass fiber pads containing lyophilized iSDA reagents were imaged after being rehydrated with 10^6 copies of a synthetic single-stranded DNA oligomer containing the *mecA* gene of MRSA (n=4 pads, 2 each on the Nexus 5X and Pixel 2 phones). The real-time images were gamma-corrected, thresholded in the red color channel, and analyzed by a computer vison algorithm detailed in the text accompanying this figure. The y-axis shows the equivalent diameter of a circle with the same area as the pixels above the threshold, while the x-axis shows the time elapsed since amplification lifted off. The propagation of the amplification front following Fick's laws for the first 15 minutes after amplification (solid black line), with a modeled modified diffusion coefficient (D_m) of 2.4×10^{-5} cm^2/s ($p<10^{-13}$, one-sample t-test). However, propagation afterward is significantly lower than diffusion as shown by the minimal overlap between the dashed black line and error bars. Points show mean and error bars show 95% confidence intervals

We then characterized propagation of the amplification front during the near-digital NAAT since species are free to diffuse during amplification. Pads containing lyophilized iSDA chemistry were rehydrated with single-stranded DNA containing the *mecA* gene, imaged with two phones during amplification, and analyzed with a computer vision algorithm to track propagation of the amplification front (n=4 pads). **Figure 7.3** shows that the amplification front expanded following Fick's laws of diffusion during the first 15 minutes after amplification had lifted off (root mean squared error=0.03 cm). The fitted modified diffusion coefficient (D_m) was 2.4×10^{-5} cm^2/s ($p<10^{-13}$, one-sample t-test) during the first 15 minutes after liftoff. The amplification front propagated slower than diffusion after 15 minutes post-liftoff, as indicated by the minimal overlap between the dashed

black line and 95% confidence intervals in **Figure 7.3**. The positive and negative controls that were run in a heat block and imaged with a mobile phone at the endpoint indeed showed red fluorescence (indicating amplification in the positive controls) and no fluorescence (indicating no amplification in the negative controls), respectively (n=2) [photos not shown].

7.4.2 Optimizing near-digital NAAT

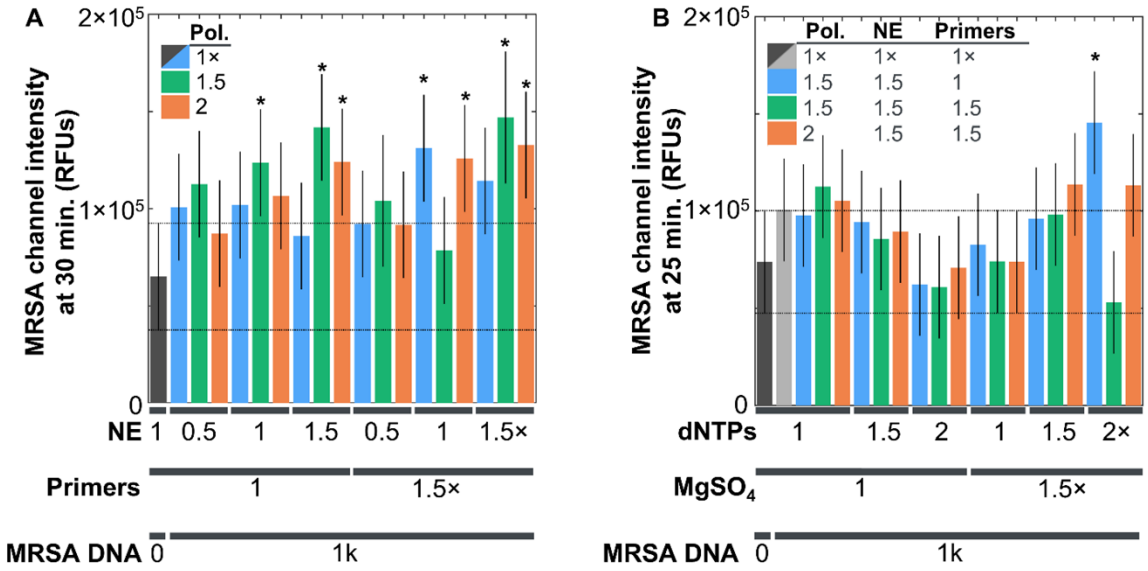

Figure 7.4: Optimizing assay time to result by varying the lyophilized master mix concentrations of polymerase (pol.), nicking enzyme (NE), primers, nucleotides (dNTPs), and magnesium sulfate ($MgSO_4$) relative to baseline (1×). All master mixes were lyophilized in glass fiber pads, rehydrated with MRSA DNA mixed with 100k copies of internal amplification control DNA, and run in a PMMA tray in a heated fluorescence plate reader. (**a**) Seven master mixes amplified by 30 minutes. (**b**) Three of the master mixes from Panel A were further tested with varying levels of nucleotides and magnesium sulfate. One master mix amplified by 25 minutes. In both panels, bars show mean and 95% confidence intervals for 3 replicates (* indicates $p<0.05$, one-way ANOVA relative to negative control).

The previous two experiments suggested that the assay had low signal to noise ratios, which we hypothesized could be improved by adjusting the assay chemistry. Therefore, we optimized the lyophilized master mix to reduce time to result (and improve signal-to-noise ratios) by performing high throughput, paper-based iSDA experiments in a plate reader. First, we optimized the concentration of polymerase, nicking enzymes, and primers by testing 18 master mixes in biplexed amplification reactions. **Figure 7.4a** shows that 7 master mixes rehydrated with MRSA-positive samples showed significantly higher MRSA-specific fluorescence at 30 minutes than the negative control ($p<0.05$, one-way ANOVA). Three of these master mixes were evaluated at a range of nucleotide and magnesium sulfate concentrations (**Figure 7.4b**). One master mix (containing 1.5× the baseline levels of polymerase, nicking enzymes, and magnesium sulfate; 2× the baseline levels of nucleotides, and 1× the baseline levels of primers) amplified by 25 minutes by having significantly higher MRSA-specific fluorescence relative to the negative control ($p<0.05$, one-way ANOVA).

7.4.3 Demonstrating shorter time to positive with optical segmentation

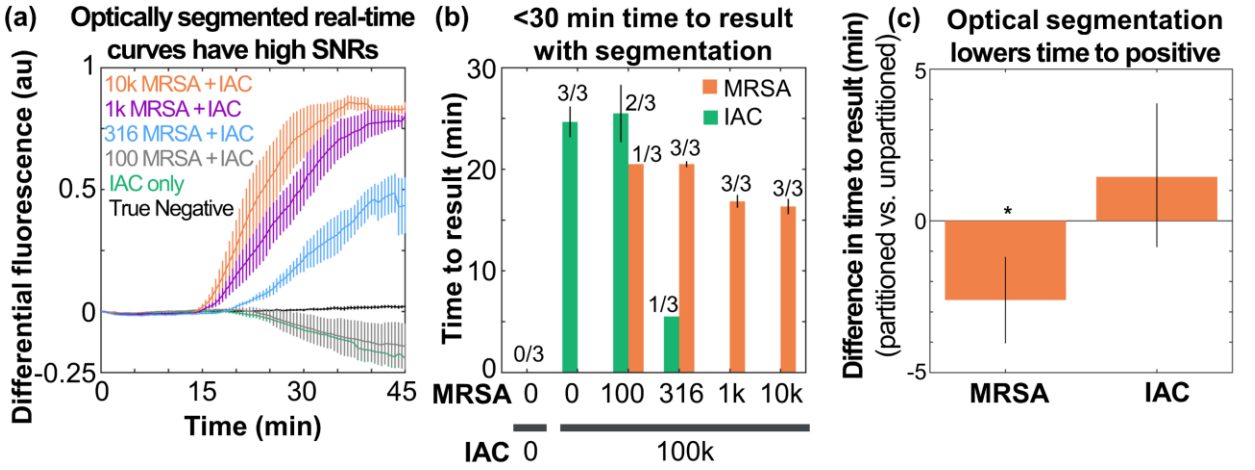

Figure 7.5: Demonstrating improved signal-to-noise ratios and time to result with near-digital NAATs. Pads containing lyophilized master mix at the optimized reagent concentrations were rehydrated with MRSA DNA biplexed with 100k copies of internal amplification control (IAC) DNA. (a) Real-time curves with optical segmentation show rapid amplification and high signal-to-background ratios for both MRSA positive and MRSA negative samples with no false positives. (b) The time to result for the MRSA channel is about 15-20 minutes in MRSA-positive samples above the limit of detection and 25 minutes for the IAC channel below the limit of detection. (c) Optical segmentation lowers the time to result in the MRSA channel by 2.6 minutes relative to unsegmented pads ($p<0.05$, one-sample t-test), but without significantly changing the time to negative ($p>0.05$, one-sample t-test). In all panels, curves and bars show mean and standard error of the mean for n=3 pads.

Finally, we evaluated the near-digital NAAT with the optimizing chemistry using biplexed samples containing MRSA genomic DNA mixed with 100k copies of IAC. Real-time curves showed rapid, reproducible amplification; MRSA-positive samples at 316 copies and above showed positive differential fluorescence signals and IAC only samples consistently had negative differential signals (**Figure 7.5a**). Times to positive were 16.3±2.3 minutes (mean ± std. dev.) at 10k copies of MRSA, 16.8±1.9 minutes at 1k copies, and 20.5±0.9 minutes at 316 copies. Times to negative were 24.7±2.6 minutes (mean ± std. dev.) for the IAC only controls (**Figure 7.5b**). One of three samples containing 100 copies of MRSA reached the threshold for positive in 20.5 minutes, whereas the other two samples reached the threshold for negative in 25.5 minutes on average (**Figure 7.5b**). Gel electrophoresis confirmed that no MRSA or IAC-specific bands appeared in the truly negative samples, but that amplification did indeed occur (**Figure 7.6**). **Figure 7.6** shows that the time to positive was 2.6 minutes lower using the near-digital optical segmentation scheme than in unsegmented pads ($p<0.05$, one-sample t-test), but the time to negative did not change significantly ($p>0.05$, one-sample t-test).

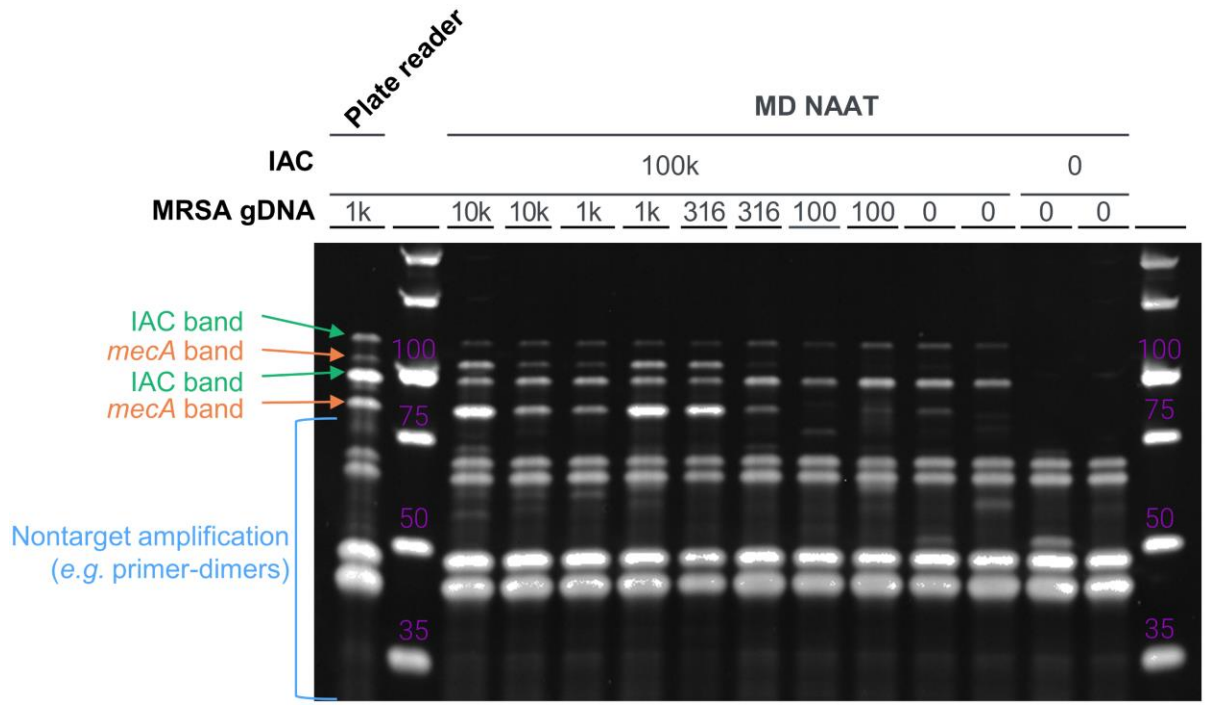

Figure 7.6: Gel electrophoresis of completed amplification reactions which were run in paper and centrifuged to isolate the liquid in the amplification pads corroborate real-time phone images. Amplification in glass fiber pads in the MD NAAT show amplification that was similar to a tube control run in a plate reader (far left). Bands corresponding to the *mecA* gene and internal amplification control (IAC) DNA were observed. The particular isothermal amplification strategy, isothermal strand displacement amplification, always shows bands from nontarget amplification (*e.g.* primer-dimers) such as those shown in the lower half of the gel. Truly negative reactions were indeed negative, all reactions containing IAC showed IAC-specific bands, and all MRSA-containing reactions showed *mecA*-specific bands at above 316 copies.

7.5 Discussion

Digital assays are a promising class of NAATs that partition an amplification reaction into multiple zones to improve time to result and limits of detection. Truly digital NAATs quantify nucleic acids based on Poisson statistics by assuming that individual wells or droplets are completely isolated. In practice, truly digital NAATs are often relegated to laboratory use due to the need for complex disposable cartridges based on traditional or droplet microfluidics. However, many digital NAATs still suffer from channeling and diffusion between neighboring amplification zones.[132] This aim describes a step toward translating digital NAATs to the point of care by implementing near-digital optical segmentation of a stationary (non-flowing) amplification reaction in a porous matrix. The strategy consists of performing a NAAT in porous media (while allowing diffusion) and imaging at high spatial resolution with a mobile phone.

The near-digital NAAT captures many of the benefits of truly digital NAATs with far simpler fluidics and assay design. Porous media automatically and passively wick fluids without pumps and enable storing lyophilized amplification reagents *in situ*.[4] Successfully implementing a near-digital assay in paper requires overcoming several constraints imposed by paper microfluidics: 1) optical artifacts caused by evaporation; 2) autofluorescence;[86] 3) low signal-to-noise ratios; and 4) limitations of low-cost hardware to uniformly heat a low thermal mass, high surface area region during

amplification. These concerns were mitigated by a combination of algorithmic, assay, and hardware optimizations as discussed in Aims 3 and 4 (chapters 6 and 7).

Real-time imaging of the near-digital NAAT was enabled by the smartphone fluorescence reader developed in Aim 4, which has high spatial (up to 80,000 pixels per pad (~560 μm^2/pixel)) and temporal resolution (every 30 seconds) over a wide field of view (up to 5×5 cm). We observed that the benefits of high spatial resolution imaging diminished when pads were optically segmented to greater than 100 blocks (750×600 μm, or 200 nL each) as shown in **Figure 7.2**. We hypothesize that this was due to diffusion of amplification products between neighboring blocks: The observed modified diffusion coefficient of 2.4×10^{-5} cm^2/s (Figure 3) implies that the amplification front would take 68 minutes (greater than the assay time) to traverse the 3 mm pad width (*e.g.* for an unsegmented pad), 2.7 minutes to travel the 600 μm block width when a pad is segmented into 100 blocks, or only 10 seconds to traverse 150 μm block width for a pad segmented into 1000 blocks.

The simplified diffusion model provides two insights toward optimizing the near-digital NAAT in the future. First, performing the near-digital NAAT in a porous membrane with a small pore radius should decrease diffusion coefficients based on **Equation 7.2**. Higher amplification speeds (*e.g.* by using a faster enzyme such as *Bst* 3.0) may also reduce the adverse impact of diffusion by generating detectable amplification products more quickly (before they diffuse away). For example, we observed that the assay chemistry optimizations shown in **Figure 7.4** reduced liftoff times by about 15 minutes and improved endpoint differential fluorescence levels by a factor of 10 (between **Figure 7.2** and **Figure 7.5**).

One important observation was that the modified diffusion coefficient of 2.4×10^{-5} cm^2/s calculated in Figure 3 is substantially greater than expected. For example, a DNA fragment of 50 bp has a nominal diffusion coefficient of 2.9×10^{-7} cm^2/s in a bulk aqueous solution.[138] This eighty-fold disparity is likely due to three main factors. First, there may have been heating-induced mass transport during amplification, driven by thermal gradients since the pads are only heated from below. Indeed, the Prandtl number for water at 50 °C is about 3.6 (and is even higher for viscous solutions (*e.g.* NAAT reagents)), which implies that advection of the amplification products and/or iSDA reagents could have skewed the calculated diffusion coefficient higher. Second, heating during amplification likely concentrated the amplification products as the aqueous solvent evaporated (as suggested by **Figure 6.5**). Third, and most importantly, the amplification front could have propagated from one block to a neighboring region not only by diffusion but also by amplification (*i.e.* biochemical reaction) in that neighboring region. In other words, rapid amplification in one region increases the concentration gradient (and diffusional flux) of the amplification products to neighboring areas, which would appear as faster-than-diffusion transport. In future work, fully accounting for all three factors in a diffusion-advection-reaction model could yield valuable insights to the true diffusion coefficient and potentially guide future optimizations of the near-digital NAAT. We did not embark on this modeling exercise in this work due to the considerable computation expense of such a model.

The near-digital assay with optically segmented mobile phone images described in this aim has several advantages over standard assays that lack segmentation. Integrating the algorithmic, assay, and hardware innovations from the last three aims increased signal-to-noise ratios by 10× (without leading to false positives or false negatives by following the principles outlined by Rolando *et al.*[132]), improved limits of detection (from above 1000 copies of MRSA genomic DNA to between 100 and 316 copies in biplexed reactions), and reduced time to result (from 45 minutes of amplification to

15-20 minutes for positive samples and 25 minutes for negative samples). These results were generalizable to multiple assays (*e.g. mecA* and *ldh1* genes for MRSA in **Figure 5.7**, **Figure 6.7**, and **Figure 7.5**), phone models with vastly different camera spectra (*e.g.* Nexus 5X and Pixel 2), and more complex samples (*e.g.* MRSA cells lysed in the proposed device or in tubes in **Figure 5.7**).

Table 7.2 shows how the near-digital NAAT compares with digital and point-of-care NAATs in the literature. The near-digital NAAT has 10-minute faster amplification times (and 25 minute faster times to result) and lower limits of detection than the biplexed colorimetric lateral flow NAAT we developed previously.[79] Limits of detection are lower than in bulk-solution assays,[97,129] but higher than truly digital (albeit singleplexed) digital assays.[83] This remarkable performance was largely enabled by the low-cost paper substrate (<$0.05) which stored lyophilized amplification reagents, passively metered and transported samples, and distributed samples over a wide area (thereby limiting the effects of diffusion). These results suggest that phone-imaged near-digital NAATs in paper are a promising step toward translating digital NAATs to the point of care.

Table 7.2: Representative digital and point-of-care NAATs

Operating principle	Readout	Consumable*	Instrument*	Point of care?	Limit of detection	Reference
Nondigital recombinase polymerase amplification in 500 nL wells	Fluorescence (singleplex)	PMMA SlipChip with laser-cut and CNC-milled features	Precision alignment tools (linear stage & micrometer drive) & reader (laser, filters, & photomultiplier tube)	No	1000 copies in buffer, 20 minutes of amplification time	129
Digital loop-mediated amplification in <10 nL wells	Colorimetric (singleplex)	Glass SlipChip fabricated with photolithography	Mobile phones with particular camera sensor	No	<40 copies in buffer, 50 minutes of amplification	83
Nondigital loop-mediated amplification in paper	Lateral flow (colorimetric, singleplex)	Paper & plastic laminate ($2.25)	Mobile phone (or eye) & custom heater ($70)	Yes	3×10^5 copies of HIV viral particles in water or whole blood, 60 minutes of amplification	97
Nondigital isothermal strand displacement amplification in paper	Lateral flow (colorimetric, biplex)	Paper & plastic with laser-cut features	Mobile phone or eye	Yes	5000 copies per device (600 copies per pad) in nasal swabs, 30 minutes of amplification + 15 minute lateral flow readout (45 min to result)	79
Near-digital isothermal strand displacement amplification in paper	Fluorescence (biplex)	Paper & plastic with laser-cut features	Any mobile phone, optical filters, & disposable heater	Yes	316 copies in buffer in biplexed reactions in 20.5 minutes of amplification	this work

*Prices, where indicated, are bill of materials costs *sans* labor

7.6 Conclusions

This aim detailed the development and application of near-digital NAATs implemented in porous media and imaged with mobile phones. It is the first demonstration of applying the principles underlying digital NAATs to porous media. The near-digital NAAT developed in this aim improved signal-to-noise ratios and lowered times to positive detection of targets, even in challenging samples containing two co-amplifying targets. A key experimental innovation that enabled this achievement was the use of a laboratory plate reader to perform high-throughput assay chemistry optimization experiments in paper with real-time fluorescence imaging. The second advance pioneered in this work is the use of high spatial and temporal resolution mobile phone imaging to improve fluorescence NAAT signal-to-noise ratios. These methods should be generalizable to any optically labeled nucleic acid amplification technique. The mobile phone-imaged, near-digital NAAT detailed in this aim is a step toward translating the benefits of truly digital NAATs to the home.

8 Conclusions

"Time is, time was, but time shall be no more."
– *A Portrait of the Artist as a Young Man* by James Joyce. 1916. p. 99, ISBN 978-1-59308-031-X.

8.1 Overall conclusions

This dissertation details the development, optimization, and validation of mobile phone-imaged fluorescence assays in highly scattering porous media. The methods described in this work are sample preparation and assay-agnostic methods that sensitively visualize fluorescence-labeled proteins and nucleic acids with smartphones. Conclusions from each specific aim of this thesis are detailed at the end of their respective chapters, but are summarized below:

1. **Develop a screening strategy to enhance the analytical performance of paper-based fluorescence assays**
   - Porous media used in paper microfluidics emit strong autofluorescence when excited at shorter wavelengths of the visible spectrum, especially ultraviolet and blue light.
   - Porous media autofluorescence lifetimes are about 5 ns for both wet and dry pads.
   - The autofluorescence spectra alone do not correlate with assay performance but require careful consideration of both the autofluorescence wavelengths and autofluorescence observed with an assay's particular imaging optics.
   - An algorithm based on the Hadamard product of autofluorescence spectra and imaging optics correlates inversely with fluorescence assay limits of detection.
   - The developed algorithm enables assay developers to quantitatively screen porous substrates used in fluorescence paper microfluidic assays, improving LODs by 50%.

2. **Mobile phone ratiometric imaging enables highly sensitive fluorescence lateral flow immunoassays without external optical filters**
   - A simple USB-powered ultraviolet LED can excite long Stokes shift fluorophores such as quantum dots without optical filters.
   - The unmodified cameras of mobile phones with different spectral sensitivities image long Stokes shift fluorophores excited by an ultraviolet LED *sans* optical filters.
   - A ratiometric algorithm quantitates quantum dots in scattering media, despite autofluorescence or variations in excitation light intensity.
   - Mobile phone ratiometric imaging of a quantum-dot labeled influenza lateral flow assay has limits of detection comparable to a laboratory fluorescence reader (2 fmol) and improved (7-12×) sensitivity compared to conventional gold nanoparticle labeling and imaging with a laboratory-grade scanner.

3. **Disposable platform for bacterial lysis and nucleic acid amplification based on a single USB-powered printed circuit board**
   - Thermally conductive tape adheres disposable NAAT cartridges to a nonplanar printed circuit board heater reproducibly and reliably (*i.e.* reproducibly between devices).
   - Heating a laser-cut NAAT cartridge only from below heats samples to near-boiling, lysing Gram-positive bacteria such as *S. aureus*.
   - Minimally fluorescent, laser cut PMMA housing adequately insulates a disposable cartridge during bacterial lysis and nucleic acid amplification.

- A single USB-powered printed circuit board platform (the MD NAAT) enables on-chip lysis and isothermal strand displacement amplification of *S. aureus* in porous media.

4. **Mobile phone imaging of colocalized fluorophores enables integrated, colocalized positive controls in point of care nucleic acid amplification assays**
   - A solid-state mobile phone fluorescence reader images colocalized fluorophores simultaneously in porous media by coupling multipass optical filters to a phone's camera and flash.
   - A differential fluorescence imaging algorithm eliminates drift and artifacts caused by evaporation and condensation in heated glass fiber pads.
   - The fluorescence reader and differential algorithm are compatible with mobile phones with different camera spectral sensitivities and visualize biplexed reactions labeled with fluorescein and a Texas Red derivative in real time.

5. **Near-digital nucleic acid amplification in porous media improves signal-to-noise ratios and time to result**
   - Optical segmentation improves signal-to-noise ratios in real-time mobile phone images of NAATs performed in porous media.
   - Optimizing the assay chemistry of a paper-based NAAT in high-throughput plate reader experiments improves signal-to-noise ratios and times to result.
   - Analyzing the top decile of pixel intensities in segmented mobile phone images does not introduce false positives but still lowers times to positive in biplexed reactions for MRSA.

8.2 Future work

The aims comprising this dissertation identified several promising avenues for future research. First, assay developers may improve signal-to-background ratios of their assays by carefully choosing fluorophores that emit at longer wavelengths, especially in the orange and red parts of the spectrum, provided that their photodetector is sufficiently sensitive at these wavelengths. Second, since the lifetime of paper autofluorescence was observed to be on the order of 5 ns, time-gated fluorescence imaging with a >400 MHz sensor may also improve signal-to-noise ratios, particularly for long-lifetime fluorophores such as quantum dots. Third, it may be possible to further lower the cost of the two-fluorophore phone reader developed in Aim 4 by eliminating the need for multipass optical filters, *e.g.* by using diffraction gratings or prisms to filter the excitation and emission light.[139,140] This consideration must balance the need to maximize fluorophore sensitivity with the practical optical engineering constraint imposed by imaging the divergent fluorescence emitted from a scattering porous substrate. Finally, the near-digital NAAT explicated in Aim 5 promises to improve signal-to-noise ratios and lower times to positive even further with additional assay and algorithmic optimizations, such as by increasing the numerical aperture or by placing a CMOS sensor directly next to the region in which the NAAT is performed. These future directions should further enhance the sensitivity and performance of fluorescence assays performed in porous media and may enable translating these assays to the home.

9 Acknowledgments

"Sed contra est quod philosophus dicit, in V Ethic., refamulari oportet ei qui gratiam fecit, et rursum ipsum incipere. Quod quidem fit dum aliquid maius retribuitur. Ergo recompensatio debet tendere ad hoc quod aliquid maius faciat."

> "On the contrary, the Philosopher [Aristotle, *Nicomachean Ethics*, v. 5] says: 'we should repay those who are gracious to us, by being gracious to them in return,' and this is done by repaying more than we have received. Therefore, gratitude should incline to do something greater."
>
> – Thomas Aquinas, *Summa Theologiæ*, Secunda Secundæ Partis, Question 106, A. 6. From *The Summa Theologiæ of Saint Thomas Aquinas*, *c.* 1265-1274, published in 1920.

I am deeply grateful for the support of everyone who offered their time and feedback to strengthen this dissertation, especially my advisor, Dr. Paul Yager, and supervisory committee members, Dr. Barry Lutz, Dr. Xiaohu Gao, and Dr. Wesley van Voorhis. I am also indebted to the extended Yager and Lutz labs for their critical feedback, research support, and invaluable brainstorming suggestions. I would like to specifically thank Peter Kauffman, Sujatha Kumar, and Steven Bennett for their feedback on electronics, assay optimization, and mechanical engineering, respectively. Special thanks are due to the undergraduates whom I have had the pleasure of mentoring and with whom I have collaborated, especially Vidhi Singh, Margarita Ankoudinova, and Charlie Glaser, among others. I would be remiss without also thanking family, friends, and especially my wife, Dr. Eleanor Shah, who have provided the support that made this thesis possible. Beyond these generalities, there were several specific contributions and funding that deserve to be specifically enumerated:

9.1 Aim 1

I am grateful for the support of Koji Abe (lateral flow assay), Sujatha Kumar (iSDA), and Dr. Liam Bradshaw (time-resolved spectroscopy). The iSDA assay used was developed by ELITechGroup. Funding was provided by the National Science Foundation (EAGER-1450187), Defense Threat Reduction Agency (HDTRA1-16-C-0029), National Science Foundation Graduate Research Fellowship (DGE-1256082), and the University of Washington College of Engineering Dean's Fellowship. Part of this work was conducted at the Molecular Analysis Facility, a National Nanotechnology Coordinated Infrastructure site at the University of Washington which is supported in part by the National Science Foundation (ECC-1542101), the University of Washington, the Molecular Engineering & Sciences Institute, the Clean Energy Institute, and the National Institutes of Health. Any opinion, findings, and conclusions or recommendations expressed in this material are of the author and do not necessarily reflect the views of the funders.

9.2 Aim 2

I would like to thank Dr. Joshua Bishop and other members of the Yager group for their support and Dr. Barry Lutz for use of lateral flow assay manufacturing (striping and guillotining) equipment. This work was funded by the National Science Foundation (EAGER-1450187 and DGE-1256082), Defense Threat Reduction Agency (HDTRA1-16-C-0029), University of Washington College of Engineering Dean's Fellowship. Any opinion, findings, and conclusions or recommendations expressed in this material are of the authors and do not necessarily reflect the views of the funders.

9.3 Aims 3 and 4

I am grateful to members of the Yager group for their insightful comments, especially Steven Bennett and Peter Kauffman. Funding was provided in part by the Bill & Melinda Gates Foundation, DARPA (DSO/BTO-HR0011-11-2-0007), the National Science Foundation via a graduate research fellowship to K.G.S. (DGE- 1762114), University of Washington College of Engineering Dean's Fellowship (to K.G.S.), and University of Washington Department of Bioengineering (to P.Y.). I would like to thank colleagues at ELITechGroup for access to the isothermal strand displacement amplification technology. Any opinion, findings, and conclusions or recommendations expressed in this material are those of the authors and do not necessarily reflect of the views of the funding sources.

9.4 Aim 5

I would like to thank Sujatha Kumar and others in the Yager group for their feedback and support with experimental design. I would like to thank colleagues at GE Global Research Laboratory, especially the research team of Dr. David R. Moore, who identified apparent supra-diffusional propagation of the amplification front in isothermal strand displacement amplification during the "MAD NAAT" project (funded by DARPA as described below). Funding was provided in part by the Bill & Melinda Gates Foundation, DARPA (DSO/BTO-HR0011-11-2-0007), the National Science Foundation via a graduate research fellowship to K.G.S. (DGE- 1762114), University of Washington College of Engineering Dean's Fellowship (to K.G.S.), and University of Washington Department of Bioengineering (to P.Y.). I would like to thank colleagues at ELITechGroup for access to the isothermal strand displacement amplification technology. Any opinion, findings, and conclusions or recommendations expressed in this material are those of the authors and do not necessarily reflect of the views of the funding sources.

10 References

"Actio gratiarum in accipiente respicit gratiam dantis"

"Thanksgiving in the recipient corresponds to the favor of the giver."
– Thomas Aquinas, *Summa Theologiæ*, Secunda Secundæ Partis, Question 106, A. 2.
From *The Summa Theologiæ of Saint Thomas Aquinas*, *c.* 1265-1274, published in 1920.

(1) Naghavi, M.; Abajobir, A. A.; Abbafati, C.; Abbas, K. M.; Abd-Allah, F.; Abera, S. F.; Aboyans, V.; Adetokunboh, O.; Ärnlöv, J.; Afshin, A.; Agrawal, A.; Zhang, X.; Zipkin, B.; Zodpey, S.; Lopez, A. D.; Murray, C. J. L. *Lancet* **2017**, *390* (10100), 1151–1210.

(2) GBD 2015 Mortality and Causes of Death Collaborators. *Lancet* **2016**, *388*, 1459–1544.

(3) Rohrman, B. A.; Leautaud, V.; Molyneux, E.; Richards-Kortum, R. R. *PLoS One* **2012**, *7* (9), e45611.

(4) Anderson, C. E.; Shah, K. G.; Yager, P. In *Methods in Enzymology*; 2017; Vol. 589, pp 383–411.

(5) Boerma, T.; Mathers, C.; AbouZahr, C.; Chattergi, S.; Hogan, D.; Stevens, G. *Health in 2015: From MDGs, Millennium Development Goals to SDGs, Sustainable Development Goals*; World Health Organization: Geneva, 2015.

(6) Dye, C. *Philos. Trans. R. Soc. B* **2014**, *369*.

(7) MacPherson, P.; Houben, R. M.; Glynn, J. R.; Corbett, E. L.; Kranzer, K. *Bull. World Health Organ.* **2014**, *92* (2), 126–138.

(8) Kettler, H.; White, K.; Hawkes, S. *Mapping the landscape of diagnostics for sexually transmitted infections*; Geneva, Switzerland, 2004.

(9) Tabrizi, S. N.; Unemo, M.; Golparian, D.; Twin, J.; Limnios, A. E.; Lahra, M.; Guy, R. *J. Clin. Microbiol.* **2013**, *51* (6), 1945–1947.

(10) Boehme, C. C.; Nabeta, P.; Hillemann, D.; Nicol, M. P.; Shenai, S.; Krapp, F.; Allen, J.; Tahirli, R.; Blakemore, R.; Rustomjee, R.; Milovic, A.; Jones, M.; O'Brien, S. M.; Persing, D. H.; Ruesch-Gerdes, S.; Gotuzzo, E.; Rodrigues, C.; Alland, D.; Perkins, M. D. *N. Engl. J. Med.* **2010**, *363* (11), 1005–1015.

(11) Nie, S.; Roth, R. B.; Stiles, J.; Mikhlina, A.; Lu, X.; Tang, Y. W.; Babady, N. E. *J. Clin. Microbiol.* **2014**, *52* (9), 3339–3344.

(12) Shah, M.; Chihota, V.; Coetzee, G.; Churchyard, G.; Dorman, S. E. *BMC Infect. Dis.* **2013**, *13* (1).

(13) Murtagh, M. M. *The Point-of-Care Diagnostic Landscape for Sexually Transmitted Infections (STIs)*; 2017.

(14) Sajid, M.; Kawde, A. N.; Daud, M. *J. Saudi Chem. Soc.* **2015**, *19* (6), 689–705.

(15) Sharp, S. E.; Ruden, L. O.; Pohl, J. C.; Hatcher, P. A.; Jayne, L. M.; Ivie, W. M. *J. Clin. Microbiol.* **2010**, *48* (6), 2082–2086.

(16) Holstein, C. A.; Griffin, M.; Hong, J.; Sampson, P. D. *Anal. Chem.* **2015**, *87* (19), 9795–9801.

(17) Rohrman, B. A.; Richards-Kortum, R. R. *Lab Chip* **2012**, *12* (17), 3082.

(18) López-Marzo, A. M.; Merkoçi, A. *Lab Chip* **2016**, *16* (17), 3150–3176.

(19) Parolo, C.; Medina-Sánchez, M.; de la Escosura-Muñiz, A.; Merkoçi, A. *Lab Chip* **2013**, *13* (3), 386–390.

(20) O'Farrell, B.; Rosen, S.; Ponti, J.; Brown, M.; Chun, P.; Mansfield, M.; Jones, K.; Tison, T.; Faulstich, K.; Gruler, Roman, Eberhard, M.; Lentzch, D.; Haberstroh, K.; Wong, R.; Tse, H. *Lateral Flow Immunoassay*; Wong, R., Tse, H., Eds.; Humana Press: Totowa, NJ, 2009.

(21) Posthuma-Trumpie, G. A.; Korf, J.; Van Amerongen, A. *Anal. Bioanal. Chem.* **2009**, *393* (2), 569–582.

(22) Martinez, A. W.; Phillips, S. T.; Whitesides, G. M.; Carrilho, E. *Anal. Chem.* **2010**, *82* (1), 3–10.

(23) Martinez, A. W.; Phillips, S. T.; Carrilho, E.; Thomas, S. W.; Sindi, H.; Whitesides, G. M. *Anal. Chem.* **2008**, *80* (10), 3699–3707.

(24) Fridley, G. E.; Le, H.; Yager, P. *Anal. Chem.* **2014**, *86* (13), 6447–6453.

(25) Lee, S.; Mehta, S.; Erickson, D. *Anal. Chem.* **2016**, acs.analchem.6b01828.

(26) Holstein, C. A. Development of a Novel Paper-Based Flu Test for Improved Diagnosis at the Point of Care, University of Washington, 2015.

(27) Yetisen, A. K.; Akram, M. S.; Lowe, C. R. *Lab Chip* **2013**, *13* (12), 2210.

(28) Sedighi, A.; Krull, U. J. *Talanta* **2018**, *186*, 568–575.

(29) Grant, B. D.; Smith, C. A.; Karvonen, K.; Richards-Kortum, R. *Analytical Chemistry*. 2016, pp 2553–2557.

(30) Fu, E.; Kauffman, P.; Lutz, B.; Yager, P. *Sensors Actuators, B Chem.* **2010**, *149* (1), 325–328.

(31) Ngom, B.; Guo, Y.; Wang, X.; Bi, D. *Analytical and Bioanalytical Chemistry*. Springer-Verlag June 27, 2010, pp 1113–1135.

(32) Paterson, A. S.; Raja, B.; Garvey, G.; Kolhatkar, A.; Hagstrom, A. E. V; Kourentzi, K.; Lee, T. R.; Willson, R. C. *Anal. Chem.* **2014**, *86* (19), 9481–9488.

(33) Zhan, L.; Guo, S. Z.; Song, F.; Gong, Y.; Xu, F.; Boulware, D. R.; McAlpine, M. C.; Chan, W. C. W.; Bischof, J. C. *Nano Lett.* **2017**, *17* (12), 7207–7212.

(34) Hammond, J. L.; Formisano, N.; Estrela, P.; Carrara, S.; Tkac, J. *Essays Biochem.* **2016**, *60* (1),

69–80.

(35) The Emerging Risk Factors Collaboration. *Lancet* **2010**, *375* (9733), 2215–2222.

(36) Zhu, X.; Shah, P.; Stoff, S.; Liu, H.; Li, C. Z. *Analyst* **2014**, *139* (11), 2850–2857.

(37) Stevens, D. Y. Development and Optical Analysis of a Microfluidic Point-of-Care Diagnostic Device, University of Washington, 2010.

(38) Rajendran, V. K.; Bakthavathsalam, P.; Jaffar Ali, B. M. *Microchim. Acta* **2014**, *181* (15–16), 1815–1821.

(39) Chen, H.; Hagström, A. E. V; Kim, J.; Garvey, G.; Paterson, A.; Ruiz-Ruiz, F.; Raja, B.; Strych, U.; Rito-Palomares, M.; Kourentzi, K.; Conrad, J. C.; Atmar, R. L.; Willson, R. C. *Sci. Rep.* **2016**, *6*, 24297.

(40) Qin, Z.; Chan, W. C. W.; Boulware, D. R.; Akkin, T.; Butler, E. K.; Bischof, J. C. *Angew. Chem. Int. Ed. Engl.* **2012**, *51* (18), 4358–4361.

(41) Hu, J.; Wang, L.; Li, F.; Han, Y. L.; Lin, M.; Lu, T. J.; Xu, F. *Lab Chip* **2013**, *13* (22), 4352–4357.

(42) Huang, S.; Abe, K.; Bennett, S.; Liang, T.; Ladd, P. D.; Yokobe, L.; Anderson, C. E.; Shah, K.; Bishop, J.; Purfield, M.; Kauffman, P. C.; Paul, S.; Welch, A. E.; Strelitz, B.; Follmer, K.; Pullar, K.; Sanchez-Erebia, L.; Gerth-Guyette, E.; Domingo, G.; Klein, E.; Englund, J. A.; Fu, E.; Yager, P. *Anal. Chem.* **2017**, *89* (11), 5776–5783.

(43) Sennepin, A. D.; Charpentier, S.; Normand, T.; Sarré, C.; Legrand, A.; Mollet, L. M. *Multiple reprobing of Western blots after inactivation of peroxidase activity by its substrate, hydrogen peroxide*; 2009; Vol. 393.

(44) Venkatraman, V.; Steckl, A. J. *Biosens. Bioelectron.* **2015**, *74*, 150–155.

(45) Lee, L. G.; Nordman, E. S.; Johnson, M. D.; Oldham, M. F. *Biosensors* **2013**, *3* (4), 360–373.

(46) Li, Z.; Wang, Y.; Wang, J.; Tang, Z.; Pounds, J. G.; Lin, Y. *Anal. Chem.* **2010**, *82* (16), 7008–7014.

(47) Wang, Q.; Nchimi Nono, K.; Syrjänpää, M.; Charbonnieère, L. J.; Hovinen, J.; Härmä, H. *Inorg. Chem.* **2013**, *52* (15), 8461–8466.

(48) Walter, J. G.; Stahl, F.; Reck, M.; Praulich, I.; Nataf, Y.; Hollas, M.; Pflanz, K.; Melzner, D.; Shoham, Y.; Scheper, T. *Eng. Life Sci.* **2010**, *10* (2), 103–108.

(49) Ge, L.; Wang, S.; Song, X.; Ge, S.; Yu, J. *Lab Chip* **2012**, *12* (17), 3150–3158.

(50) Urata, M.; Iwata, R.; Noda, K.; Murakami, Y.; Kuroda, A. *Biotechnol. Lett.* **2009**, *31* (5), 737–741.

(51) Yu, L.; Shi, Z.; Fang, C.; Zhang, Y.; Liu, Y.; Li, C. *Biosens. Bioelectron.* **2015**, *69*, 307–315.

(52) Gasperino, D. J.; Leon, D.; Lutz, B.; Cate, D. M.; Nichols, K. P.; Bell, D.; Weigl, B. H. *Anal. Chem.* **2018**, *90* (11), 6643–6650.

(53) Lathwal, S.; Sikes, H. D. *Anal. Chem.* **2016**, *88* (6), 3194–3202.

(54) Göröcs, Z.; Ozcan, A. *Lab Chip* **2014**, *14* (17), 3248–3257.

(55) Petryayeva, E.; Algar, W. R. *Anal. Bioanal. Chem.* **2016**, *408* (11), 2913–2925.

(56) Noor, M. O.; Krull, U. J. *Anal. Chem.* **2014**, *86* (20), 10331–10339.

(57) US Food and Drug Administration. *Digital health innovation action plan*; 2017.

(58) Priye, A.; Ball, C. S.; Meagher, R. J. *Anal. Chem.* **2018**, acs.analchem.8b03521.

(59) Abe, K.; Suzuki, K.; Citterio, D. *Anal. Chem.* **2008**, *80* (18), 6928–6934.

(60) Lathwal, S.; Sikes, H. D. *Lab Chip* **2016**, *16* (8), 1374–1382.

(61) Choi, D. H.; Lee, S. K.; Oh, Y. K.; Bae, B. W.; Lee, S. D.; Kim, S.; Shin, Y. B.; Kim, M. G. *Biosens. Bioelectron.* **2010**, *25* (8), 1999–2002.

(62) Janssen, K. P. F.; Knez, K.; Spasic, D.; Lammertyn, J. *Sensors (Switzerland)* **2013**, *13* (1), 1353–1384.

(63) Zhang, H.; Li, X. F.; Le, X. C. *Anal. Chem.* **2012**, *84* (2), 877–884.

(64) Lee, S.; Kim, G.; Moon, J. *Sensors (Switzerland)* **2013**, *13* (4), 5109–5116.

(65) Stevens, D. Y.; Petri, C. R.; Osborn, J. L.; Spicar-Mihalic, P.; McKenzie, K. G.; Yager, P. *Lab Chip* **2008**, *8* (12), 2038–2045.

(66) Hall, E. A. H. H.; Chen, S.; Chun, J.; Du, Y.; Zhao, Z. *Trends in Analytical Chemistry*. 2016, pp 247–256.

(67) Fridley, G. E.; Holstein, C. A.; Oza, S. B.; Yager, P. *MRS Bull.* **2013**, *38* (04), 326–330.

(68) Hollas, M.; Jallerat, E.; Pflanz, K.; Praulich, I.; Walter, J.; Stahl, F.; Scheper, T. *Desalination* **2006**, *199* (1–3), 230–231.

(69) Kopf, E.; Zharhary, D. *International Journal of Biochemistry and Cell Biology*. 2007, pp 1305–1317.

(70) Chi, J.; Gao, B.; Sun, M.; Zhang, F.; Su, E.; Liu, H.; Gu, Z. *Anal. Chem.* **2017**, *89* (14), 7727–7733.

(71) Song, X.; Knotts, M. *Anal. Chim. Acta* **2008**, *626* (2), 186–192.

(72) Linnes, J. C.; Rodriguez, N. M.; Liu, L.; Klapperich, C. M. *Biomed. Microdevices* **2016**, *18* (2), 1–12.

(73) Lee, J. Y.; Kim, Y. A.; Kim, M. Y.; Lee, Y. T.; Hammock, B. D.; Lee, H. S. *Anal. Chim. Acta* **2012**, *757*, 69–74.

(74) McKnight, D. M.; Boyer, E. W.; Westerhoff, P. K.; Doran, P. T.; Kulbe, T.; Andersen, D. T. *Limnol. Oceanogr.* **2001**, *46* (1), 38–48.

(75) Coble, P. G. *Mar. Chem.* **1996**, *51* (4), 325–346.

(76) Zepp, R. G.; Sheldon, W. M.; Moran, M. A. In *Marine Chemistry*; 2004; Vol. 89, pp 15–36.

(77) Horn, R. In *The Hadamard Product*; Johnson, C., Ed.; Proceedings of Symposia in Applied Mathematics: Providence, Rhode Island, 1990; p 88.

(78) Hawkins, K. R.; Yager, P. *Lab Chip* **2003**, *3* (4), 248–252.

(79) Lafleur, L. K.; Bishop, J. D.; Heiniger, E. K.; Gallagher, R. P.; Wheeler, M. D.; Kauffman, P. C.; Zhang, X.; Kline, E. C.; Buser, J. R.; Kumar, S.; Byrnes, S. A.; Vermeulen, N. M. J.; Scarr, N. K.; Belousov, Y.; Mahoney, W.; Toley, B. J.; Ladd, P. D.; Lutz, B. R.; Yager, P.; Ramachandran, S.; Byrnes, S. A.; Vermeulen, N. M. J.; Scarr, N. K.; Belousov, Y.; Mahoney, W.; Toley, B. J.; Ladd, P. D.; Lutz, B. R.; Yager, P. *Lab Chip* **2016**, *52* (19), 3377–3383.

(80) Tang, R.; Yang, H.; Gong, Y.; You, M.; Liu, Z.; Choi, J. R.; Wen, T.; Qu, Z.; Mei, Q.; Xu, F. *Lab Chip* **2017**, *17* (7), 1270–1279.

(81) Monahan, C. M. Fluorescence Detection of DNA Amplification in Porous Media for Point-of-Care Diagnostics, University of Washington, 2015.

(82) Gui, C.; Wang, K.; Li, C.; Dai, X.; Cui, D. *Nanoscale Res. Lett.* **2014**, *9* (1), 57.

(83) Rodriguez-Manzano, J.; Karymov, M. A.; Begolo, S.; Selck, D. A.; Zhukov, D. V.; Jue, E.; Ismagilov, R. F. *ACS Nano* **2016**, *10* (3), 3102–3113.

(84) Vashist, S. K.; Mudanyali, O.; Schneider, E. M.; Zengerle, R.; Ozcan, A. *Anal. Bioanal. Chem.* **2014**, *406* (14), 3263–3277.

(85) Matasaru, C. Mobile Phone Camera Possibilities for Spectral Imaging, University of Eastern Finland, 2014.

(86) Shah, K. G.; Yager, P. *Anal. Chem.* **2017**, *89* (22), 12023–12029.

(87) Panpradist, N.; Toley, B. J.; Zhang, X.; Byrnes, S.; Buser, J. R.; Englund, J. A.; Lutz, B. R. *PLoS One* **2014**, *9* (9), e105786.

(88) Eickhardt, S.; Kragh, K. N.; Schrøder, S.; Poulsen, S. S.; Sillesen, H.; Givskov, M.; Høiby, N.; Bjarnsholt, T.; Alhede, M. *Pathog. Dis.* **2015**, *73* (4).

(89) Hulspas, R.; O'Gorman, M. R. G.; Wood, B. L.; Gratama, J. W.; Robert Sutherland, D. *Cytometry Part B - Clinical Cytometry*. Wiley Subscription Services, Inc., A Wiley Company November 1, 2009, pp 355–364.

(90) Ren, M.; Xu, H.; Huang, X.; Kuang, M.; Xiong, Y.; Xu, H.; Xu, Y.; Chen, H.; Wang, A. *ACS Appl. Mater. Interfaces* **2014**, *6* (16), 14215–14222.

(91) Kairdolf, B. A.; Mancini, M. C.; Smith, A. M.; Nie, S. *Anal. Chem.* **2008**, *80* (8), 3029–3034.

(92) Qin, W.; Wang, K.; Xiao, K.; Hou, Y.; Lu, W.; Xu, H.; Wo, Y.; Feng, S.; Cui, D. *Biosens. Bioelectron.* **2017**, *90*, 508–515.

(93) Malashikhina, N.; Garai-Ibabe, G.; Pavlov, V. *Anal. Chem.* **2013**, *85* (14), 6866–6870.

(94) Yang, X.; Liu, L.; Hao, Q.; Zou, D.; Zhang, X.; Zhang, L.; Li, H.; Qiao, Y.; Zhao, H.; Zhou, L. *PLoS One* **2017**, *12* (2), e0171376.

(95) Petryayeva, E.; Algar, W. R. *Anal. Chem.* **2014**, *86* (6), 3195–3202.

(96) Hazelton, B.; Gray, T.; Ho, J.; Ratnamohan, V. M.; Dwyer, D. E.; Kok, J. *Influenza Other Respi. Viruses* **2015**, *9* (3), 151–154.

(97) Phillips, E. A.; Moehling, T. J.; Ejendal, K. F. K.; Hoilett, O. S.; Byers, K. M.; Basing, L. A.; Jankowski, L. A.; Bennett, J. B.; Lin, L.-K.; Stanciu, L. A.; Linnes, J. C. *Lab Chip* **2019**.

(98) Oblath, E. A.; Henley, W. H.; Alarie, J. P.; Ramsey, J. M. *Lab Chip* **2013**, *13* (7), 1325–1332.

(99) Ma, Y.-D.; Li, K.-H.; Chen, Y.-H.; Lee, Y.-M.; Chou, S.-T.; Lai, Y.-Y.; Huang, P.-C.; Ma, H.-P.; Lee, G.-B. *Lab Chip* **2019**.

(100) Shah, K. G.; Guelig, D.; Diesburg, S.; Buser, J.; Burton, R.; LaBarre, P.; Richards-Kortum, R.; Weigl, B. *PLoS One* **2015**, *10* (10), e0139449.

(101) Buser, J. R.; Zhang, X.; Byrnes, S. A.; Ladd, P. D.; Heiniger, E. K.; Wheeler, M. D.; Bishop, J. D.; Englund, J. A.; Lutz, B.; Weigl, B. H.; Yager, P. *Anal. Methods* **2016**, *8* (14), 2880–2886.

(102) Curtis, K. A.; Rudolph, D. L.; Nejad, I.; Singleton, J.; Beddoe, A.; Weigl, B.; LaBarre, P.; Owen, S. M. *PLoS One* **2012**, *7* (2), e31432.

(103) Singleton, J.; Osborn, J. L.; Lillis, L.; Hawkins, K.; Guelig, D.; Price, W.; Johns, R.; Ebels, K.; Boyle, D.; Weigl, B.; LaBarre, P. *PLoS One* **2014**, *9* (11), e113693.

(104) Heiniger, E. K.; Buser, J. R.; Mireles, L.; Zhang, X.; Ladd, P. D.; Lutz, B. R.; Yager, P. *J. Microbiol. Methods* **2016**, *128*, 80–87.

(105) Ezaki, T.; Suzuki, S. *J. Clin. Microbiol.* **1982**, *16* (5), 844–846.

(106) Toley, B. J.; Covelli, I.; Belousov, Y.; Ramachandran, S.; Kline, E.; Scarr, N.; Vermeulen, N.; Mahoney, W.; Lutz, B. R.; Yager, P. *Analyst* **2015**, *140* (22), 7540–7549.

(107) Phillips, E. A.; Shen, R.; Zhao, S.; Linnes, J. C. *Lab Chip* **2016**, *16* (21), 4230–4236.

(108) Buser, J. R.; Diesburg, S.; Singleton, J.; Guelig, D.; Bishop, J. D.; Zentner, C.; Burton, R.; LaBarre, P.; Yager, P.; Weigl, B. H. *Lab Chip* **2015**, *15* (September 2016), 4423–4432.

(109) Liu, C.; Mauk, M. G.; Hart, R.; Qiu, X.; Bau, H. H. *Lab Chip* **2011**, *11* (16), 2686–2692.

(110) Pardy, T.; Tulp, I.; Kremer, C.; Rang, T.; Stewart, R. *PLoS One* **2017**, *12* (12), e0189968.

(111) Shah, K. G.; Singh, V.; Kauffman, P. C.; Abe, K.; Yager, P. *Anal. Chem.* **2018**, *90* (11), 6967–6974.

(112) Rodriguez, N. M.; Linnes, J. C.; Fan, A.; Ellenson, C. K.; Pollock, N. R.; Klapperich, C. M. *Anal. Chem.* **2015**, *87* (15), 7872–7879.

(113) Schoepp, N. G.; Schlappi, T. S.; Curtis, M. S.; Butkovich, S. S.; Miller, S.; Humphries, R. M.; Ismagilov, R. F. *Sci. Transl. Med.* **2017**, *9* (410), eaal3693.

(114) Coppens, J.; Van Heirstraeten, L.; Ruzin, A.; Yu, L.; Timbermont, L.; Lammens, C.; Matheeussen, V.; McCarthy, M.; Jorens, P.; Ieven, M.; Kumar-Singh, S.; Goossens, H.; Malhotra-Kumar, S. *Antimicrob. Resist. Infect. Control* **2019**, *8* (1), 4.

(115) Horst, A. L.; Rosenbohm, J. M.; Kolluri, N.; Hardick, J.; Gaydos, C. A.; Cabodi, M.; Klapperich, C. M.; Linnes, J. C. *Biomed. Microdevices* **2018**, *20* (2), 35.

(116) Kong, J. E.; Wei, Q.; Tseng, D.; Zhang, J.; Pan, E.; Lewinski, M.; Garner, O. B.; Ozcan, A.; Di Carlo, D. *ACS Nano* **2017**, *11* (3), 2934–2943.

(117) Shin, D. J.; Athamanolap, P.; Chen, L.; Hardick, J.; Lewis, M.; Hsieh, Y. H.; Rothman, R. E.; Gaydos, C. A.; Wang, T. H. *Sci. Rep.* **2017**, *7* (1), 4495.

(118) Chen, W.; Yu, H.; Sun, F.; Ornob, A.; Brisbin, R.; Ganguli, A.; Vemuri, V.; Strzebonski, P.; Cui, G.; Allen, K. J.; Desai, S. A.; Lin, W.; Nash, D. M.; Hirschberg, D. L.; Brooks, I.; Bashir, R.; Cunningham, B. T. *Anal. Chem.* **2017**, *89* (21), 11219–11226.

(119) Selck, D. A.; Karymov, M. A.; Sun, B.; Ismagilov, R. F. *Anal. Chem* **2013**, *85*, 54.

(120) Kim, H.; Jung, Y.; Doh, I. J.; Lozano-Mahecha, R. A.; Applegate, B.; Bae, E. *Sci. Rep.* **2017**, *7*.

(121) Apfalter, P.; Reischl, U.; Hammerschlag, M. R. *Journal of Clinical Microbiology*. December 2005, pp 5835–5841.

(122) Hoorfar, J.; Cook, N.; Malorny, B.; Wagner, M.; De Medici, D.; Abdulmawjood, A.; Fach, P. *J. Clin. Microbiol.* **2003**, *41* (12), 5835–5835.

(123) Whiley, D. M.; Lambert, S. B.; Bialasiewicz, S.; Goire, N.; Nissen, M. D.; Sloots, T. P. *Crit. Rev. Microbiol.* **2008**, *34* (2), 71–76.

(124) Espy, M. J.; Uhl, J. R.; Sloan, L. M.; Buckwalter, S. P.; Jones, M. F.; Vetter, E. A.; Yao, J. D. C.; Wengenack, N. L.; Rosenblatt, J. E.; Cockerill, F. R.; Smith, T. F. *Clinical Microbiology Reviews*. January 2006, pp 165–256.

(125) Whiley, D. M.; Tapsall, J. W.; Sloots, T. P. *Journal of Molecular Diagnostics*. Association of Molecular Pathology 2006, pp 3–15.

(126) Priye, A.; Bird, S. W.; Light, Y. K.; Ball, C. S.; Negrete, O. A.; Meagher, R. J. *Sci. Rep.* **2017**, *7*, 44778.

(127) Chapin, K. C.; Flores-Cortez, E. J. *J. Clin. Microbiol.* **2015**, *53* (2), 706–709.

(128) Novak-Weekley, S.; Marlowe, E. M.; Poulter, M.; Dwyer, D.; Speers, D.; Rawlinson, W.; Baleriola, C.; Robinson, C. C. *J. Clin. Microbiol.* **2012**, *50* (5), 1704–1710.

(129) Tsaloglou, M. N.; Watson, R. J.; Rushworth, C. M.; Zhao, Y.; Niu, X.; Sutton, J. M.; Morgan, H. *Analyst* **2014**, *140* (1), 258–264.

(130) Shen, F.; Du, W.; Kreutz, J. E.; Fok, A.; Ismagilov, R. F. *Lab Chip* **2010**, *10* (20), 2666–2672.

(131) Xia, Y.; Liu, Z.; Yan, S.; Yin, F.; Feng, X.; Liu, B. F. *Sensors Actuators, B Chem.* **2016**, *228*, 491–499.

(132) Rolando, J. C.; Jue, E.; Schoepp, N. G.; Ismagilov, R. F. *Anal. Chem.* **2019**, *91* (1), 1034–1042.

(133) Hindson, B. J.; Ness, K. D.; Masquelier, D. A.; Belgrader, P.; Heredia, N. J.; Makarewicz, A. J.; Bright, I. J.; Lucero, M. Y.; Hiddessen, A. L.; Legler, T. C.; Kitano, T. K.; Hodel, M. R.; Petersen, J. F.; Wyatt, P. W.; Steenblock, E. R.; Shah, P. H.; Bousse, L. J.; Troup, C. B.; Mellen, J. C.; Wittmann, D. K.; Erndt, N. G.; Cauley, T. H.; Koehler, R. T.; So, A. P.; Dube, S.; Rose, K. A.; Montesclaros, L.; Wang, S.; Stumbo, D. P.; Hodges, S. P.; Romine, S.; Milanovich, F. P.; White, H. E.; Regan, J. F.; Karlin-Neumann, G. A.; Hindson, C. M.; Saxonov, S.; Colston, B. W. *Anal. Chem.* **2011**, *83* (22), 8604–8610.

(134) Byrnes, S. A.; Chang, T. C.; Huynh, T.; Astashkina, A.; Weigl, B. H.; Nichols, K. P. *Anal. Chem.* **2018**, *90* (15), 9374–9380.

(135) Yen, G. S.; Fujimoto, B. S.; Schneider, T.; Kreutz, J. E.; Chiu, D. T. *J. Am. Chem. Soc.* **2019**, *141* (4), 1515–1525.

(136) Quan, P. L.; Sauzade, M.; Brouzes, E. *Sensors (Switzerland)*. MDPI AG April 20, 2018.

(137) Renkin, E. M. *J. Gen. Physiol.* **1954**, *38* (2), 225–243.

(138) Lukacs, G. L.; Haggie, P.; Seksek, O.; Lechardeur, D.; Freedman, N.; Verkman, A. S. *J. Biol. Chem.* **2000**, *275* (3), 1625–1629.

(139) Zhang, C.; Cheng, G.; Edwards, P.; Zhou, M. Da; Zheng, S.; Liu, Z. *Lab Chip* **2016**, *16* (2), 246–250.

(140) Wang, L.-J.; Naudé, N.; Chang, Y.-C.; Crivaro, A.; Kamoun, M.; Wang, P.; Li, L. .

11 Appendix

Table 11.1: List of abbreviations

Abbreviation	Extended
2DPN	Two-dimensional paper network
µPAD	Microfluidic paper-based analytical device
ACP	Achromopeptidase
ANOVA	Analysis of variance
CCD	Charge-coupled device
CMOS	Complementary metal-oxide-semiconductor
DAB	3,3'-Diaminobenzidene
DNA	Deoxyribonucleic acid
DNG	Digital negative
EEM	Excitation-emission matrix
ELISA	Enzyme-linked immunosorbent assay
FRET	Forster resonance energy transfer
gDNA	Genomic deoxyribonucleic acid
HRP	Horseradish peroxidase
IAC	Internal amplification control
iSDA	Isothermal strand displacement amplification
JPEG	Joint Photographic Experts Group
LAMP	Loop-mediated amplification
LED	Light-emitting diode
LOD	Limit of detection
MAD NAAT	Multiplexed, autonomous, and disposable nucleic acid amplification test
MD NAAT	Multiplexed, disposable nucleic acid amplification test
MRSA	Methicillin-resistant *Staphylococcus aureus*
NAAT	Nucleic acid amplification test
NP	Nucleoprotein
PCB	Printed circuit board
PDMS	Polydimethylsiloxane
PMMA	Polymethylmethacrylate
PVDF	Polyvinylidene difluoride
RGB	Red, green, and blue
SDA	Strand displacement amplification
sRGB	Standard red, green, and blue
ssDNA	Single-stranded DNA
TIFF	Tagged image file format
TMB	3,3'-5-5'-tetramethylbenzidene
US	United States
USB	Universal serial bus
USD	United States dollar
UV	Ultraviolet
wrt	With respect to